

Epileptic Neural Dynamics: Insights from a Computational Model of a CA3 Hippocampal Network

by

Marc Julius Posthuma

Radboud University, in affiliation with Synaptica B.V.



Synaptica

Readers:

1st: Prof. Dr. P.H.E. Tiesinga

2nd: Prof. Dr. R.J.A. van
Wezel

Supervised by:

Dr. Marijn Martens (CEO)

Sean Gies, MSc

Thesis submitted in partial fulfillment of the requirements for the degree of Master of Science in
Medical Biology (Specialization: Neurobiology)

April 26th, 2024

Copyright Notice

Contents of this thesis, including data and software, were produced and/or utilized under a signed agreement with Synaptica B.V., and are considered proprietary.

Data and Code Availability

The datasets and computer code utilized in the simulations and subsequent analyses within this thesis are proprietary assets owned by Synaptica B.V. Software includes the “Neuromics” and “Network_Sims” packages developed by Synaptica B.V. These materials are not available to the public, and all rights to their use are exclusively reserved by Synaptica B.V. Inquiries regarding access to the data and code for replicating experiments or for further analysis of the results should be directed to Synaptica B.V., attention Marijn Martens.

Requests can be sent via email to info@synaptica.nl.



Declaration of Originality

I hereby declare that this thesis, titled “*Epileptic Neural Dynamics: Insights from a Computational Model of a CA3 Hippocampal Network*”, is my own original work and has been written by me. All sources and materials used have been properly acknowledged and referenced. This thesis has been prepared in accordance with the rules and regulations set by the exam committee of the FNWI, Radboud University, regarding plagiarism. I affirm that this work has not been submitted for any other academic degree or professional qualification.

Marc Julius Posthuma
26th of April, 2024



Abstract

Temporal lobe epilepsy (TLE) is a frequently occurring form of epilepsy, commonly associated with the hippocampus, particularly its CA3 subfield, which is noted for its hyperexcitability and crucial role in seizure generation. This study employs a computational model of the CA3 subfield, developed within the NEURON simulation environment, comprising 800 pyramidal cells, 200 basket cells, and 200 oriens-lacunosum moleculare (OLM) interneurons. To simulate genetic profiles characteristic of epilepsy, network alterations were introduced to sodium and potassium conductances across all cell types. The study examines the impact of these alterations on neural oscillations within the theta-gamma frequency range and their power. Additionally, it investigates the network's susceptibility to depolarization blocks in basket cell populations resulting from increased external noise. An in-depth exploration of population burst dynamics was also conducted. Furthermore, the effects of strengthened recurrent connections in the basket cell population were examined to assess the potential for rescuing the network from an ictal state back to homeostatic baseline activity. The findings suggest that the CA3 network is indeed hyperexcitable, with imbalances in sodium and potassium channels that mirror genetic predispositions for epilepsy, leading to increased firing rates and heightened susceptibility to epileptiform activity. Moreover, the network demonstrated increased resilience to depolarization blocks through enhanced soma-inhibition by recurrently connected basket cells, showing effects akin to those of contemporary anti-epileptic drugs (AEDs) and other therapeutic interventions.

Keywords: Temporal lobe epilepsy; CA3; hippocampus; computational neuroscience; NEURON; depolarization block; ictal state; oscillations

Acknowledgements

I am immensely grateful to Marijn Martens and Sean Gies for their guidance and mentorship during my six-month internship at Synaptica B.V. Their expertise was crucial in both practical and theoretical aspects of my work as a Master's student.

Marijn Martens provided invaluable insights that enhanced my analytical thinking and problem-solving skills, vital for completing this thesis. The opportunity to work at Synaptica B.V., with access to excellent computational resources and travel support, greatly contributed to my experience.

Observing the company's growth and the scale of projects managed by Sean, Arthogrul, and their teams was particularly inspiring. It was motivating to see the progress made over my tenure, adding a valuable perspective to my career path.

Special thanks to Sean Gies for his thorough and patient explanations of complex technical processes, which deepened my understanding of programming significantly. Both Marijn and Sean were always approachable, providing feedback and fostering a collaborative environment that supported my development as a researcher.

I am also thankful to the entire team and fellow students at Synaptica B.V. for their support and encouragement throughout my internship. Their feedback and suggestions played a significant role in shaping my research direction.

This thesis has undoubtedly benefited from their profound professional guidance, and for that, I am truly thankful.

“Every man can, if he so desires, become the sculptor of his own brain” — **Santiago Ramón y Cajal**

Contents

Copyright Statement	1
Abstract	2
Acknowledgements	3
1 Introduction	9
1.1 Background	9
1.2 Aim of the research	13
1.3 Research question	14
2 Methods	15
2.1 Computational model	15
2.2 Model implementation: cell parameters	17
2.3 Model implementation: synaptic connections	18
2.4 Model implementation: stimulation and noise	20
2.5 Simulations	20
2.5.1 Baseline activity	20
2.5.2 Model validation	21
2.5.3 Sodium and potassium variants	21
2.5.4 External noise variants	24
2.5.5 External noise: Burst analysis	27
2.5.6 Recurrent connection strength variants	29
3 Results	31
3.1 Results of the Baseline activity	31
3.2 Results of the Model validation	33
3.3 Results of the Sodium-Potassium variants	39
3.3.1 Firing rates: Pyramidal cells	39
3.3.2 Firing rates: Basket cells	40
3.3.3 Firing rates: O-LM cells	40
3.3.4 Dominant frequencies	41
3.3.5 Theta-gamma power	42
3.4 Results of the External Noise variants	44
3.4.1 Occurrence of depolarization block events across noise conditions	44
3.4.2 Average delay of depolarization block events across noise conditions	46
3.5 Results of the External Noise: Burst analysis	48
3.5.1 Inter-ictal state	48

3.5.2	Pre-ictal state	48
3.5.3	Ictal state	48
3.6	Results of the Recurrent Connections variants	51
4	Discussion	53
4.1	Model assumptions and Observations	54
4.1.1	Sodium and Potassium variants	54
4.1.2	External noise variants	56
4.1.3	Recurrent connection strength variants	58
4.2	Implications of the findings	58
4.3	Limitations of the research	59
4.4	Suggestions for future research	60
	Bibliography	61
A	Appendix	66
A.1	Cellular dynamics: equations and parameters	66
B	Appendix	70
B.1	Additional tables	70
B.1.1	Sodium-Potassium variants numerical results.	70
B.1.2	Compartment dependent parameters	72
B.1.3	Connections	73
B.1.4	NetStim parameters	75
C	Appendix	77
C.1	Additional data	77
C.2	Additional figures	77
C.2.1	External Noise variants: DPB percentage matrices	78
C.2.2	External Noise variants: DPB delay matrices	81
C.2.3	Recurrent connection matrices	84
	About Synaptica B.V.	86

List of Figures

2.1	Schematic of the CA3 network model	16
2.2	Sanjay et al. (2015) article results	22
2.3	Depolarization block in basket cells	25
2.4	Burst detection example	28
3.1	Baseline activity of the CA3 network	32
3.2	20 % OLM-Pyr connection scatter plot	33
3.3	0 % OLM-Pyr connection scatter plot	34
3.4	Validation: Firing rates per population	36
3.5	Validation: Dominant frequencies	37
3.6	Validation: Theta-Gamma power	38
3.7	Sodium-Potassium variants: Firing rates per population	39
3.8	Sodium-Potassium variants: Dominant frequencies	41
3.9	Sodium-Potassium variants: Theta-Gamma power	42
3.10	Comparative FFT of LFP: O-LM variants	44
3.11	10 % O-LM-Pyr connection with increased external noise scatter plot	45
3.12	DPB percentage matrices	46
3.13	DPB delay matrices	47
3.14	Burst detection near the onset of a depolarization block	50
3.15	RC DPB percentage matrices (all)	52
C.1	DPB percentage matrices (all)	78
C.2	DPB delay matrices (all)	81
C.3	RC DPB percentage matrices (all)	84

List of Tables

2.1	Compartment dependent parameters	18
2.2	Synaptic Parameters for the Connectivity Between Neurons in the Model	19
2.3	Summary of Original Network Simulation Parameters and Results . .	21
3.1	Summary of Model validation: Network simulation Parameters and Results	35
B.1	Sodium variant: Pyramidal cell	70
B.2	Sodium variant: Basket cell	70
B.3	Sodium variant: OLM cell	71
B.4	Potassium variant: Pyramidal cell	71
B.5	Potassium variant: Basket cell	71
B.6	Potassium variant: OLM cell	72
B.7	Compartment dependent parameters	72
B.8	Synaptic Parameters for the Connectivity Between Neurons in the Model	73
B.9	Pyr to Other Cells NMDA Connections Summary	73
B.10	Pyr to Other Cells AMPA Connections Summary	74
B.11	Bwb to Other Cells GABA Connections Summary	74
B.12	OLM to Pyr GABA Connections Summary	74
B.13	NetStim Parameters Pyramidal cells	75
B.14	Noise to OLM Parameters	75
B.15	Noise to BWB Parameters	75
B.16	Noise from MS to BWB & OLM Parameters	76

1 Introduction

1.1 Background

Epilepsy is a neurological disorder characterized recurrent seizures. Seizures have to be two or more unprovoked and more than 24 hours apart, a single unprovoked seizure with a high recurrence risk (>60 % over the next 10 years); or the patient needs to have been previously diagnosed with an epilepsy syndrome. Patients with epilepsy usually also suffer cognitive challenges, language difficulties, and an increased risk of mental health issues, such as anxiety and depression (Fisher et al., 2014).

At its core, epilepsy involves an imbalance between excitatory and inhibitory processes within the brain. This imbalance can originate in specific brain regions and spread, affecting various interconnected areas outside of the epileptogenic zone (Lüders et al., 2006). The minimum amount of brain tissue of an associated region that initiates a seizure is therefore not fixed and is the reason epilepsy is often thought of as a network disorder.

Temporal Lobe Epilepsy (TLE), the most prevalent form of focal epilepsy in adults (60% of cases), impacts over 30 million people globally by estimation of the World Health Organization. TLE's epileptic events often begin in brain regions like the hippocampus and entorhinal cortex, known for their capacity to independently produce epileptiform activities (Lytton et al., 2005). Despite improvements over the years, not all TLE patients respond to medication, are subject to drug-resistance (25–30%) or suffer intolerable adverse effects (30–40%, Hakami (2021)). Thus, research into TLE's underlying mechanisms is vital for developing effective new treatments.

The hippocampus, located in the temporal lobe, is crucial for memory formation and retrieval, emotion regulation, and spatial navigation. In TLE, it often serves as the seizure's focal point, especially its CA3 subfield. The CA3 region, with its dense connections and low epilepsy activation threshold, is particularly susceptible to hyper-excitability (Witter, 2007). In TLE, seizures can be triggered by excessive input from higher cortical regions, such as the visual or auditory cortex that project to the hippocampus via the entorhinal cortex.

How excessive input is handled however, is dependent on the network's intrinsic properties and its functional connectivity. The CA3 subfield of the hippocampus plays a pivotal role in facilitating higher cognitive functions such as memory encoding and retrieval, spatial navigation, and pattern completion and separation. The region exhibits robust capacity for synaptic plasticity via long-term potentiation (LTP) and depression (LTD), mechanisms that underlie learning and memory and are modulated by the level of neural activity (Stokes et al., 2015).

Perturbations in the connectivity of the CA3 region are common in TLE and directly impacts the working memory (WM) of the network (Arski et al., 2021). However, the exact mechanisms by which these perturbations lead to epileptiform activity are not well understood. The hippocampus is particularly susceptible to connectivity variability which can be transiently induced by epileptic discharge. This is likely due to the high processing demands for WM (Aldenkamp & Arends, 2004).

The neural assemblies that constitute the circuits in the CA3 region are highly regulated and the transfer of information propagates through specific oscillatory patterns. Characteristic neural oscillations in the hippocampus, such as theta (3–12 Hz) and gamma (30–80 Hz) rhythms, play significant roles in forming episodic memory and cognition (Nyhus & Curran, 2010).

Epilepsy is associated with alterations in Cross-Frequency Coupling (CFC), where the phase of slower waves modulates the amplitude of faster waves, reflecting disrupted network functionality. Abnormalities in Theta-Gamma Phase-Amplitude Coupling (PAC) correlate with cognitive impairments in epilepsy. Therefore, tracking changes in these neural oscillations can provide insights into the disease's progression.

Detecting the state of the brain is crucial for predicting and managing seizures, as patients of epilepsy only experience the effects of their disease during seizures. The gold standard of brain activity detection utilizes the electroencephalogram (EEG), which can adequately measure electrical fluctuations in the range of theta-gamma oscillations.

The associated brain region of an epilepsy patient when investigated can be in one of three states that have been generally defined using various epilepsy detection algorithms:

- **Inter-ictal State**

- *Definition:* The period between seizures, with no active seizure activity.
- *Characterization:* Characterized by inter-ictal spikes or sharp waves in EEG. These spikes indicate abnormal electrical discharges that are not actual seizures.

- **Pre-ictal State**

- *Definition:* The period immediately before the onset of a seizure.
- *Characterization:* Marked by subtle and variable changes in EEG and other physiological signals that precede seizures, crucial for seizure prediction efforts.

- **Ictal State**

- *Definition:* The period during which a seizure occurs.
- *Characterization:* EEG shows sustained, rhythmic electrical activity distinct from normal or inter-ictal activity, with corresponding behavioral symptoms based on seizure type.

Classification methods can extract the aforementioned epileptic features from the EEG based on comparison of different kernels (Linear, Sigmoid, Grid, etc). The classification accuracy of these methods vary but are fairly high (>98.9 %) for methods such as Support Vector Machine (SVM) or Wavelet Neural Network (WNN) classification (Yayik et al., 2015). These methods demonstrate significant potential in enhancing the accuracy of epilepsy state detection, offering promising avenues for more effective monitoring and intervention strategies in epilepsy management.

Identification of the epileptic states provides a benchmark for potential epileptiform activity in a (simulated) network. Epilepsy as a whole could be viewed particular brain functioning state, manifested in a multi-state network of coupled oscillatory systems. Therefore, tracking observable phenomena in the CA3 region of the hippocampus, such as bursting or oscillatory coupling could provide insights into the network's susceptibility to ictal transitions (Kalitzin et al., 2019).

In the past 20 years, research has shown that at least half of all epilepsy cases have a genetic basis. Rapid discovery of disease-causing genes have identified genes encoding for ion channel proteins. Remarkably, a quarter of all cases involving monogenic variants are related to ion channels (Oyrer et al., 2018; Striano & Minassian, 2020).

Sodium and potassium channels in particular, are essential for maintaining the resting membrane potential and action potential generation in neurons. Dysfunctional variants of sodium or potassium channels can lead to hyperexcitability in neurons, depending on whether the relevant mutation causes loss or gain of function. This in turn can have destabilizing effects on neural circuits in regions such as the CA3 subfield of the hippocampus in TLE.

A lot of epileptic mutations have been found in *voltage-gated* type ion channel genes. For example, for sodium these are most often related to the brain-expressed SCN family (*SCN1A*, *SCN2A*, *SCN3A* and *SCN1B*, Brunklaus and Lal (2020)). Highly conserved across species, these genes encode for the pore-forming alpha subunits of the sodium channel and are responsible for the fast depolarizing current in neurons. Previous research has shown that mutations in these genes have become increasingly frequent in Mendelian epilepsy syndromes in recent years (Brunklaus & Lal, 2020).

These SCN genes are involved in generalized epilepsy with febrile seizures plus (GEFS+) syndrome, with some novel mutations in genes such as *SCN1B* being correlated directly with TLE phenotypes in oocytes (Scheffer et al., 2006). These kinds of mutations are often associated with a loss of function, leading to a decrease in sodium current and a subsequent increase in the threshold for action potential generation (Wallace et al., 1998). However, the same mutation in mammalian cells exhibited reduced degradation during periods of high-frequency channel activity. This indicates an improved ability of the channel to reset itself between activation events, potentially causing increased excitability (Meadows et al., 2002).

SCN1A in particular encodes predominantly in inhibitory GABAergic neurons, usually enriched in axonal segments and facilitates initiation of action potentials (Yu et al., 2006). *SCN1A* is also associated with Dravet syndrome, a severe form of (loss-of-function) epilepsy that is often drug-resistant and a candidate of familial mesial temporal lobe epilepsy (Hwang & Hirose, 2012).

Classically, these voltage-gated channels only allow for passage of ions transiently, and are closed at rest. However, a fraction of sodium ions passes through constantly

(1%-2%). So while these channels form the foundation for excitable cell function, a small fraction of channels shows persistent current, I_{NaP} . This current is normally contributes to proper physiological function of neurons, but can become pathogenic when dysregulated. In recent years I_{NaP} has been identified as an important factor in sodium channelopathies, which could provide targets for novel anti-seizure medication strategies (Wengert & Patel, 2021).

Similarly, there are also common mutations in potassium channels that are associated with epilepsy. The KCN family contains genes that encode the respective sub-units in potassium channels in TLE: *KCNA1*, *KCNA2*, *KCNJ11* and *KCNS1* (Gao et al., 2022; Zhang et al., 2023). The dysfunction of these channels can lead to hyperexcitability in neurons, where modified dynamics of voltage gated channels lead to changes in the action potential's shape and duration. *KCNA1* targeted deletions result in TLE-symptoms rodent models of epilepsy due to impaired repolarization of excitatory neurons (Eunson et al., 2000). Moreover, *KCNA2* mutations can increase seizure susceptibility by decrease of the AP threshold (Liu et al., 2020). In healthy neurons regulation of current happens via inwardly rectifying potassium channels that maintain the resting membrane potential (Isomoto et al., 1997). In channelopathies regarding voltage-gated potassium channels, altered potassium gradients or accelerated hyperpolarization might occur which can no longer be compensated for by the rectifying potassium channels (Nikitin & Vinogradova, 2021). This showcases the fact that both sodium and potassium channels are heavily involved in the pathophysiology of epilepsy.

A lot of genetic variety exists for both of these major channels and can both lead to a destabilized hyperexcitable network, hallmark of epileptic activity. However, it remains difficult to quantitatively translate the genetic profile to network dynamics. This is where computational models can provide a valuable tool to investigate the impact of genetic variations on network behavior.

The NEURON simulator is a powerful tool for modeling the intricate dynamics of neurons and their networks. It supports detailed simulations of membrane dynamics, synaptic interactions, and the Hodgkin-Huxley model for action potentials. The Hodgkin-Huxley model, a cornerstone of computational neuroscience, describes the ionic currents underlying action potentials in neurons based on non-linear differential equations (Hodgkin et al., 1952). This simulation framework allows for quite realistic representation of life-like neurons based on experimentally-defined cellular characteristics. Many of which are freely available on ModelDB, but vary in terms of complexity such as morphology, synapses or 3D-micro-environment.

NEURON's Python interface facilitates scripting and integration with other Python-based tools, enhancing its utility in neuroscience research. This simulator is crucial for studying neural phenomena, the effects of anti-epileptic drugs, and diseases caused by dysfunctional ion channels for sodium and potassium, providing invaluable insights into the functioning of the nervous system and the development of therapeutic strategies (Migliore et al., 2006).

1.2 Aim of the research

This study aims to further investigate the role of the CA3 region of the hippocampus in epilepsy, by adapting the computational model of the CA3 region of the hippocampus by Neymotin et al. (2011) in the NEURON simulator. The model consists of 800 pyramidal, 200 O-LM interneurons and 200 basket cells. The baseline model contains enough biophysical detail to replicate homeostatic neural activity, consisting of theta-modulated gamma oscillations observable in the local field potential. In the model the inhibitory interactions between pyramidal cells and basket cells (soma-inhibiting) are crucial for the generation of gamma oscillations. Consequently, the O-LM interneurons are responsible for the generation of theta oscillations (dendritic inhibition).

This research builds upon experiments by Sanjay et al. (2015), which focussed on reducing dendritic inhibition, increasing external stimulation and modifying synaptic connectivity as potential causes for TLE.

This study focusses on the role of sodium and potassium channels via ion-conductance modifications throughout the network, the sensitivity for external noise in such conditions and the effects increasing recurrent connectivity of inhibitory basket cells.

1.3 Research question

This research is focused on the following research question:

Main Research Question

- What is the impact of different genetic profiles on epileptic activity in simulated hippocampal brain circuits?

Main Hypothesis

- It is hypothesized that by emulating specific genetic profiles within simulated CA3 hippocampal neural networks, we can replicate their impact on the networks' behavior. Furthermore, it is expected that inducing cellular dynamics that reduce seizure-like (ictal) activity will rescue normal network function.

Investigative Sub-Questions

1. What specific variables such as firing rate, bursting behavior (peak size and timing) characterize (inter)-ictal activity in different neural cell types within temporal lobe epilepsy (TLE) networks?
2. How do these variables vary across different neural networks, and how can they be reliably measured and quantified in a NEURON model?
3. How can genetic variations, such as single nucleotide polymorphisms (SNPs) or known epilepsy-inducing mutations, be successfully integrated into hippocampal neural network models to simulate the impact on ictal activity?
4. What alterations in network dynamics and connectivity patterns are observed when introducing epilepsy-associated genetic variations into neural cell types?
5. Can the effects of specific genetic variants be correlated with the severity and frequency of seizures in the modeled networks?
6. Can we identify specific targets for intervention that can restore normal network dynamics in the presence of epilepsy-associated genetic variations?
7. Are we able to reliable predict the effect of a specific drug on the network dynamics and emulate them in the model?

2 Methods

2.1 Computational model

The network model that was used in this research is a custom implementation made by Sanjay et al. (2015). This model is based on the CA3 subfield region of the hippocampus, originally designed by Neymotin et al. (2011). The model is implemented in the NEURON simulation environment using python version 3.9.16 as an interface (<https://www.neuron.yale.edu>). The model consists of 1000 neurons, which are divided into populations containing three cell-types: 800 5-compartment pyramidal cells (three apical dendrites, one basal dendrite, and soma), 200 1-compartment soma-inhibiting basket cells and 200 1-compartment Oriens-Lacunosum Moleculare (O-LM) interneurons. The original source code of the model is available on ModelDB at the following link: <http://senselab.med.yale.edu/modeldb>ShowModel.asp?model=139421>.

The implementation used in this research made in cooperation with Sean Gies is part of the *Neuromics* software package by Synaptica B.V. The implementation has been modified to allow for more ease of use and to allow for the implementation of cellular modifications and network manipulations. Descriptions of the cell-types and their classes, network design, synaptic connections and stimulation parameters can be found in appendix A.

The experimental source code for this research project can be found on request on GitHub at the following link: https://github.com/SynapticaNL/Marc_network_sims.

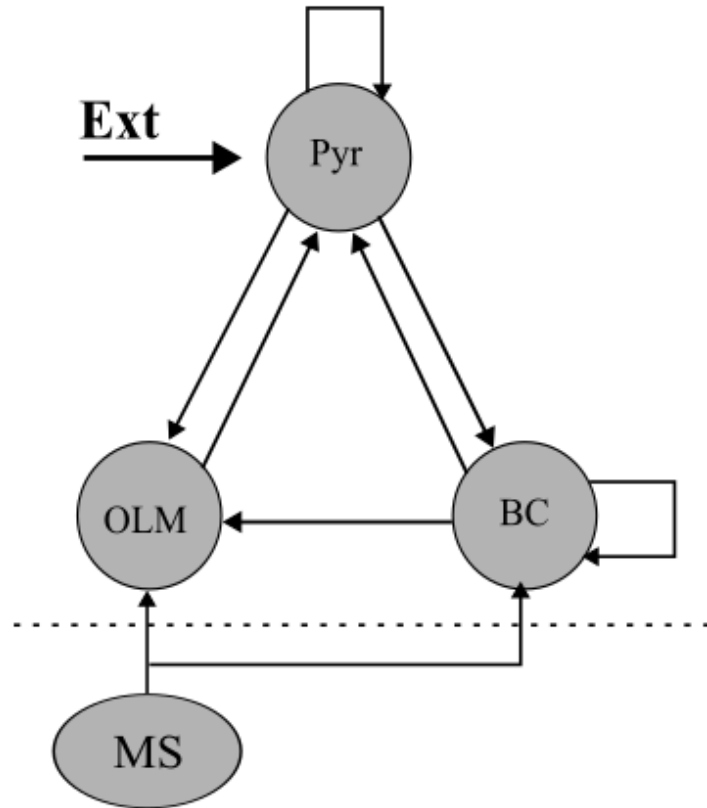


Figure 2.1: Schematic of the CA3 network model. The network comprises of many microcircuits with the connectivity as shown in the above figure. Pyr cells (pyramidal), BC cells (basket cells that inhibit soma), O-LM cells (oriens-lacunosum moleculare interneurons that inhibit dendrites), external inputs (mainly from the entorhinal cortex) to Pyr cells, and MS (medial septum). BC and O-LM cells are stimulated by Pyr cells, while Pyr cells are inhibited by BC and O-LM cells. Recurrent connections among Pyr cells are excitatory, whereas those among BC cells are inhibitory. O-LM cells are inhibited by BC cells. The medial septum (MS) delivers inhibitory inputs every 150 ms to BC and O-LM cells.

2.2 Model implementation: cell parameters

The model consists of three types of neurons, each with its own set of parameters and defined cell classes. The parameters for each cell type are based on the following references:

1. **Basket Cells:** Modeled after Wang and Buzsáki (1996), featuring standard dynamics for Na and K currents, along with synaptic and leak currents. Each cell is modeled as a single compartment and obeys the following current balance equation:

$$C_I \frac{dV_I}{dt} = I_{\text{app},I} - I_{\text{Na},I} - I_{\text{K},I} - I_{\text{L},I} - I_{\text{syn},I} \quad (2.1)$$

where V_I is the membrane potential (mV), $C_I = 1 \mu\text{F}/\text{cm}^2$ is the membrane capacitance, $I_{\text{app},I}$ is the applied current, and $I_{\text{syn},I}$ is the total synaptic current. The leak current $I_{\text{L},I} = g_{\text{L},I}(V_I - E_{\text{L},I})$ has a conductance $g_{\text{L},I} = 0.1 \text{ mS}/\text{cm}^2$ and reversal potential $E_{\text{L},I} = -65 \text{ mV}$. All currents are in units of $\mu\text{A}/\text{cm}^2$. The sodium $I_{\text{Na},I}$ and potassium $I_{\text{K},I}$ currents are voltage-dependent spiking currents of the Hodgkin-Huxley type.

2. **O-LM Cells:** Adapted from Saraga et al. (2003), including additional currents like hyperpolarization-activated (h) and A-type currents. Each cell is modeled as a single compartment and obeys the following current balance equation:

$$C_O \frac{dV_O}{dt} = I_{\text{app},O} - I_{\text{Na},O} - I_{\text{K},O} - I_{\text{L},O} - I_{\text{h},O} - I_{\text{A},O} - I_{\text{syn},O} \quad (2.2)$$

where V_O is the membrane potential, $C_O = 1.3 \mu\text{F}/\text{cm}^2$ is the membrane capacitance, $I_{\text{app},O}$ is the applied current, and $I_{\text{syn},O}$ is the total synaptic current. The leak current $I_{\text{L},O} = g_{\text{L},O}(V_O - E_{\text{L},O})$ with conductance $g_{\text{L},O} = 0.05 \text{ mS}/\text{cm}^2$ and reversal potential $E_{\text{L},O} = -70 \text{ mV}$. $I_{\text{Na},O}$, $I_{\text{K},O}$, $I_{\text{h},O}$, and $I_{\text{A},O}$ represent the transient sodium, delayed rectifier potassium, hyperpolarization-activated (or h) mixed-cation, and A-type potassium currents, respectively, all in units of $\mu\text{A}/\text{cm}^2$.

3. **Pyramidal Cells:** Based on Migliore et al. (2004), incorporating compartmentalized dynamics for the complex morphology of pyramidal neurons. Each cell is modeled as a multi-compartmental neuron with 5 compartments: 1 for basal dendrites (Bdend), 1 for soma, and 3 for apical dendrites (Adend1, 2 and 3). Each compartment obeys the following current balance equation:

$$C_{E_k} \frac{dV_{E_k}}{dt} = I_{\text{app},E_k} - I_{\text{Na},E_k} - I_{\text{K},E_k} - I_{\text{L},E_k} - I_{\text{h},E_k} - I_{\text{A},E_k} - I_{\text{syn},E_k} + I_{\text{conn},E_k} \quad (2.3)$$

where V_{E_k} is the membrane potential of compartment k , C_{E_k} is the membrane capacitance, I_{app,E_k} is the applied current, I_{syn,E_k} is the total synaptic current, and I_{conn,E_k} represents the current due to electrical coupling between compartments. I_{L,E_k} , I_{Na,E_k} , I_{K,E_k} , I_{h,E_k} , and I_{A,E_k} denote the leak, transient sodium, delayed rectifier potassium, hyperpolarization-activated mixed-cation, and A-type potassium currents for compartment k , respectively.

For further elaboration of the mathematical formulation of each cell type, see appendix A. For the full overview of cell and compartment parameters, see appendix B.

2.3 Model implementation: synaptic connections

The model contained three types of synaptic connections: excitatory, inhibitory based on AMPA, NMDA and GABA-A receptors. Synapses were modeled by standard NEURON double-exponential mechanism. This approach entailed the assignment of specific rise τ_1 and decay τ_2 time constants, which correspond to the temporal profiles of conductance increase and subsequent decline, respectively, following a synaptic event. The conductance values, indicative of synaptic efficacy, were varied according to the type of presynaptic and postsynaptic neuron pairing, as well as the subtype of receptor involved (AMPA, NMDA, or GABA-A). These parameters informed the simulation of synaptic inputs, which govern the depolarization and hyperpolarization events in the postsynaptic neuron membrane, thereby influencing the temporal patterns of neuronal firing and network activity. These parameters adhere to the following formula:

$$g(t) = \frac{g_{\max}}{\tau_2 - \tau_1} \left(e^{-\frac{t}{\tau_2}} - e^{-\frac{t}{\tau_1}} \right) \quad (2.4)$$

The synaptic conductance at a given time t after a presynaptic spike is represented by $g(t)$, where g_{\max} indicates the peak conductance measured in NanoSiemens (nS). The rise and decay of the synaptic conductance are characterized by the time constants τ_1 and τ_2 , respectively, both of which are measured in milliseconds (ms). Here, t stands for the time elapsed following the arrival of the presynaptic spike. This model effectively describes the dynamic behavior of synaptic conductance, which initially rises during the onset phase and subsequently undergoes a more prolonged decrease, a pattern common to both excitatory and inhibitory postsynaptic potentials (EPSPs and IPSPs). The variation in the time constants τ_1 and τ_2 facilitates the adjustment of the synaptic response's time profile, with τ_1 influencing the speed of onset and τ_2 affecting the length of the conductance alteration. For the parameters used, see Table 2.1 and 2.2.

Table 2.1: Compartment dependent parameters used in the formulations of the three neuronal cell types according to equation 2.4. See appendix A for the full equations. The ionic conductances are in mS/cm².

	g_h	g_A	g_{Na}	g_K	V_{50}	b	c	d	e	f
Bdend	0.1	48	32	10	-82	1	4	1.5	11	0.825
Soma	0.1	48	32	10	-82	0.8	4	1.5	11	0.825
Adend1	0.2	72	32	10	-82	0.5	4	1.5	11	0.825
Adend2	0.4	120	32	10	-90	0.5	2	1.8	-1	0.7
Adend3	0.7	200	32	10	-90	0.5	2	1.8	-1	0.7

The synaptic connections between neurons were implemented as follows:

Table 2.2: Synaptic Parameters for the Connectivity Between Neurons in the Model: Pre- and postsynaptic receptor types are given for each cell type. The time constants τ_1 and τ_2 are in milliseconds. τ_1 is the rise time constant, the time it takes for synaptic conductance to increase from baseline to peak. τ_2 is the decay time constant, the time it takes for the conductance to decrease from peak to baseline. The conductance indicates the strength of the synaptic connection and its ability to conduct ionic current across the postsynaptic membrane. This influences the extent to which the synaptic input can depolarize the postsynaptic neuron and is in nanoSiemens (nS).

Presynaptic	Postsynaptic	Receptor	τ_1 (ms)	τ_2 (ms)	Conductance (nS)
Pyramidal	Pyramidal	AMPA	0.05	5.3	0.02
Pyramidal	Pyramidal	NMDA	15	150	0.004
Pyramidal	Basket	AMPA	0.05	5.3	0.36
Pyramidal	Basket	NMDA	15	150	1.38
Pyramidal	OLM	AMPA	0.05	5.3	0.36
Pyramidal	OLM	NMDA	15	150	0.72
Basket	Pyramidal	GABA-A	0.07	9.1	0.72
Basket	Basket	GABA-A	0.07	9.1	4.5
Basket	OLM	GABA-A	0.07	9.1	0.0288
OLM	Pyramidal	GABA-A	0.2	20	72
MS	Basket	GABA-A	20	40	1.6
MS	OLM	GABA-A	20	40	1.6

For the full overview of synaptic parameters, see appendix B.

2.4 Model implementation: stimulation and noise

The model was activated by external inputs originating from the entorhinal cortex, which were then transmitted to the pyramidal cells. Background random excitatory and inhibitory inputs were received by the O-LM, basket cells, and the soma of the pyramidal cells via their AMPA, NMDA, and GABA-A receptors as shown in Table 2.2. The mechanism by which noise was applied to the model was defined via NEURON simulator's *NetStim* object. This object type generated spike train according to a set of parameters such as stimulus interval, noise variability (Poisson-like), weight, target, start and delay times. These parameters can be viewed in Appendix A.

Similarly, the distal dendritic compartments of the pyramidal cells also received comparable inputs through the same types of receptors. Connections such as O-LM to pyramidal cell, basket to pyramidal cell, basket-basket recurrent connections, and medial septum to O-LM and basket cell connections were mediated through GABA-A receptors. Additionally, the medial septum provided inhibitory inputs to the basket and O-LM cells at intervals of 150 ms.

2.5 Simulations

For the simulations, the model was implemented in NEURON version 7.6.3. The simulations were run on a Linux GNOME (v22.04) desktop computer with 2 Xeon CPU E5-2699 v3 CPUs with 32 physical cores @ 2.3GHz for multi-threading, a Nvidia GTX 4060 graphics card, and 256 GB of RAM. Trials were run for 5000 ms with a time integration step of 0.1 ms resulting in 50.000 simulation steps per trial dataset. Random seeds were used to generate the external noise, connections and cells for each trial and remained constant between trials and between experiments. The number of trials varies between experiments and are specified in their respective sub-sections that follow. In the network, the individual cells were assigned a global identifier (GID) to which all the data was associated in the same ascending order for each trial. The first 800 cells were always pyramidal cells, the next 200 were basket cells and the last 200 were O-LM cells. For each trial, the individual cell spike times were saved for the entire duration of the simulation. Pyramidal cell membrane soma voltage data was saved per cell in order to calculate the LFP signal (necessary for theta-gamma calculations). In all simulations the LFP is calculated by taking the sum of the differences in membrane potential of the distal apical and basal dendritic compartments of all cells in the pyramidal population.

2.5.1 Baseline activity

In order to obtain baseline activity in the network as shown in Figure 2.1, current injections were added (**Pyramidal cells:** 50 pA; **O-LM cells:** -25 pA). At Baseline, the network generates theta-modulated gamma oscillations activity. This activity was measured from the Local Field potential (LFP) in the network. The LFP was simulated by a sum difference between membrane potential of the distal apical and basal dendritic compartment over all pyramidal cells. As discussed in the cell parameters section, all cells contained leak current, transient sodium current I_{Na} ,

and delayed rectifier current $I_{K,\text{dr}}$ to allow for action potential generation. On average, the firing rates were 2.36 ± 0.024 Hz for pyramidal cells, 16.05 ± 0.15 Hz for basket cells and 0.96 ± 0.027 Hz for O-LM interneurons at baseline in the original (Sanjay et al., 2015). However, it should be noted that our custom implementation of the same model had a slightly lowered baseline (see the results section). The reason for this discrepancy is unknown and is a potential source of error in the results. 50 trials total were done for the baseline activity and averaged.

2.5.2 Model validation

In order to test the implementation of the model, results from the article were replicated, namely Figures 6A, B and C from Sanjay et al. (2015). In this replicated experiment the O-LM to pyramidal cells connection weight was reduced in decrements of 0.1x times the baseline from 1.0 to 0.0. In addition to reduced connection strength, the external noise fed into the pyramidal cells was increased in increments of 0.1X times the baseline from 1.0 to 2.0. By reducing the connectivity from O-LM to pyramidal cells, dendritic inhibition was impaired and potential epileptiform activity was induced.

The original results on which the validation experiment focussed on, were the following three aspects: changes in firing rates per population, the changes in dominant theta and gamma frequencies, and finally the changes in the power of the theta and gamma oscillations (see Figure: 2.2). The numerical results from are in the following table:

Table 2.3: Overview of Original Network Simulation Settings and Outcomes. This table contains all the original results of Figure 6 from the Sanjay et al. (2015) article. Variations in the firing rates of single cells, alongside theta and gamma oscillations within the local field potential, as well as the alterations in their intensity upon the decrease of dendritic inhibition and the concurrent enhancement of external stimuli to the pyramidal neurons.

OLM-Pyr Wt	External Wt	Pyr (Hz) + Std	BWB (Hz) + Std	OLM (Hz) + Std	Theta Freq (Hz)	Theta power (mV ² Hz ⁻¹)	Gamma Freq (Hz)	Gamma power (mV ² Hz ⁻¹)
1x	1x	2.36 ± 0.024	16.05 ± 0.15	0.96 ± 0.027	6.7	5.35	33.2	2.55
0.8x	1.2x	2.66 ± 0.029	19.88 ± 0.11	1.11 ± 0.03	6.7	5.4	32.5	2.4
0.6x	1.4x	2.9 ± 0.03	21.04 ± 0.15	1.42 ± 0.03	6.7	4.1	32.4	5.3
0.4x	1.6x	3.19 ± 0.033	22.15 ± 0.15	1.93 ± 0.03	6.7	2.2	31.7	3.6
0.2x	1.8x	3.67 ± 0.036	23.97 ± 0.15	2.64 ± 0.036	6.7	2	32.7	6.5
0.1x	1.9x	4.24 ± 0.038	26.98 ± 0.15	3.35 ± 0.034	6.7	1.16	33.9	11.4
0.05x	1.95x	4.5 ± 0.04	21.68 ± 0.25	3.69 ± 0.033	6.7	0.65	37.8	1.55
0x	2x	6.14 ± 0.054	24.26 ± 0.44	4.98 ± 0.035	0	0	38.8	1.32

2.5.3 Sodium and potassium variants

In this experiment, the sodium and potassium conductances of the all cell types cells were changed from 0.5x to 1.5x times the baseline in increments of 0.1. The changes were induced in separate experiments for each of the three cell types, so 6 experiments in total were conducted: 3 for sodium and 3 for potassium. These induced changes were done in order to investigate the effect of the conductances on the network activity and the influence of individual cell types on the same metrics as in the model validation experiment. 20 trials each were done per condition (6 total conditions) and the results were averaged.

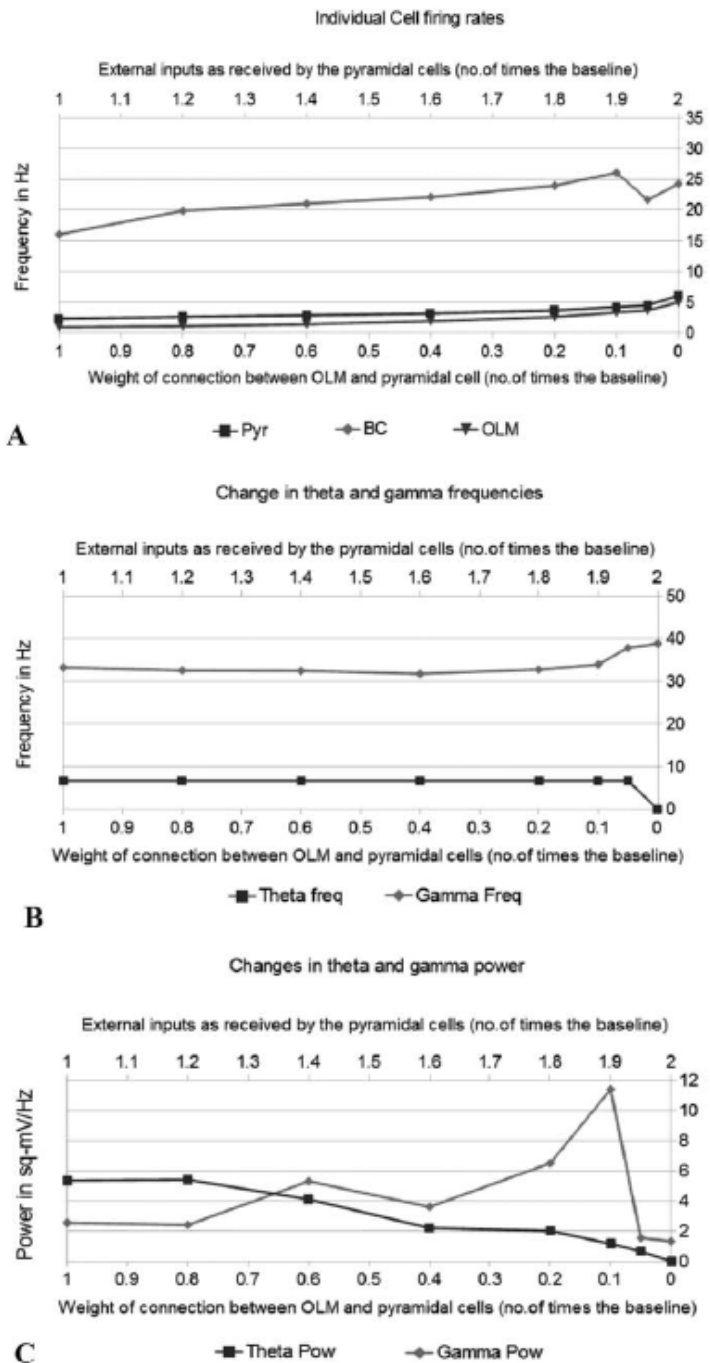


Figure 2.2: Sanjay et al. (2015) article results: Figure 6. A validation experiment was conducted to replicate the results of scenario 2 from the original article. This was done in order to verify the implementation of the model. The experiment involved reducing the connection strength from O-LM to pyramidal cells and increasing the external noise fed into the pyramidal cells. The firing rates per population (A), dominant frequencies in the theta-gamma bands (B) and their respective average power (C) was investigated. The results were compared to the original article to verify the implementation of the model (see Results section).

Visualization of Neuronal Activity Variants

This section outlines the analytical approach adopted for visualizing the neuronal activity within our network model under different experimental conditions. Specifically, we focused on plotting the firing rates, theta-gamma frequencies, and theta-gamma power across all neuronal populations (pyramidal, basket, and O-LM cells) for variants induced by alterations in sodium and potassium conductance levels.

Firing Rate Analysis

We initiated our analysis by examining the firing rates across different cell populations. A comparative visualization was generated to juxtapose the mean firing rates under sodium and potassium variant conditions, utilizing a grid layout for a side-by-side comparison. Each plot incorporated error bars to represent the standard error of the mean (SEM), thereby conveying the variability inherent in our simulation trials. Cell populations were differentiated by distinct markers and colors to facilitate clear distinction between pyramidal, basket, and O-LM cells across varying conditions.

Theta-Gamma Frequency Analysis

Subsequent to firing rate analysis, we delved into the investigation of theta and gamma frequency bands. For each variant type (sodium and potassium), theta and gamma frequencies were plotted on a 2×2 grid, delineating the mean frequency values extracted from the simulation data. This approach allowed for an intuitive understanding of the oscillatory dynamics prevalent in the network under different ionic conductance conditions, highlighting potential shifts in theta-gamma coupling associated with epileptiform activities.

Theta-Gamma Power Analysis

In addition to the frequency analysis, the power of theta and gamma oscillations were quantified. This step aimed to investigate the intensity of oscillatory activity within these critical frequency bands. Similar to our frequency analysis, a 2×2 grid layout facilitated the comparison of theta and gamma power across sodium and potassium variants. This visual representation served to elucidate variations in oscillatory power, potentially correlating with changes in network excitability and synchronization under altered ionic conditions.

Power Spectral Density (PSD) Calculation

The aforementioned theta-gamma analyses used the `calc_psd` function to compute the power spectral density (PSD) of an LFP signal, focusing on theta (3–12 Hz) and gamma (30–80 Hz) frequencies. Initial signal processing includes discarding the first millisecond to avoid transient effects and down-sampling according to a predefined maximum frequency (f_{max}). The PSD calculation uses a Fast Fourier Transform (FFT) approach, adjusting for the signal mean. For both theta and gamma ranges, the function identifies relevant frequencies, calculates mean power by averaging power values within these ranges, and identifies the dominant frequency by locating the frequency with the maximum power value. This analysis facilitated

the quantification of signal power and rhythmic activity within specific frequency bands, essential for understanding neural dynamics in these ranges.

2.5.4 External noise variants

In this experiment, the external noise fed into the distal dendrites of pyramidal cells was set a new baseline for the 1.0x condition, which was 20 times that of the original Sanjay et al. (2015) model. Excitatory inputs were fed through AMPA and NMDA receptors. Reduced O-LM to pyr connections were kept at 10% of the original baseline. This was done because in the original article, epileptic activity was induced by feeding in 20 times more external noise at reduced dendritic inhibition.

This condition was tested as a special condition in Figure 7 of the article, and was expanded upon because of the occurrence of a depolarization block in the basket cell spike activity. This depolarization block occurrence was assumed to be the epileptic state in which the network is found at such conditions. This new baseline was changed times a range of pyramidal noise factors of the following values: 0.65, 0.70, 0.75, 0.80, 0.85, 0.90, 0.95, 1.00, 1.10, 1.20, and 1.30. In addition to the range of noise factors, pyramidal conductances g_{Na} and g_K were modified over a range of 0.5x to 1.5x times the baseline in increments of 0.1. 15 trials were done per noise condition and the results were averaged.

Detection of epileptiform activity (Experiments: External Noise and Recurrent Connection strength variants)

The detection of epileptic activity depends on the spiking activity of the basket cells, which according to results of Figure 7 from the Sanjay et al. (2015) article occurs in the presence of great external drive from the pyramidal cells of at least 20 times the baseline and with reduced dendritic inhibition by the O-LM cells. Detection of a depolarization block in the basket cells was done by calculating the convoluted fire rates of the basket cell population.

The systematic approach to analyzing basket cell firing rates through convolution with a Gaussian window was as follows:

- **Extracting Spike Times:** The `get_spike_times_for_basket_cells` function is used for iterating over a range of GIDs. This process collects spike times from all basket cells and concatenates them, constructing a continuous signal of neural activity.
- **Creating Time Series:** Spike times are converted into a binary series using `create_time_series`. Each neural firing event is denoted by a '1' in a zero-initialized array at the corresponding time index.
- **Applying Gaussian Convolution:** The `apply_gaussian_convolution` function smooths the time series. It convolves the series with a Gaussian window, normalized to sum to one, yielding a signal that mirrors the firing rates over time.
- **Summing Convolved Signals:** Collective firing behavior is analyzed by `get_convolved_signal_per_neuron`. It applies Gaussian convolution to individual neuron time series and sums them, forming an aggregated firing rate signal.

- **Detecting Depolarization Blocks:** The `detect_depolarization_blocks` function identifies reduced activity periods by analyzing the convolved signal for intervals that remain below a set threshold for a specified minimum duration.

This method for detecting depolarization blocks in the basket cell population and convolution of spike activities was also used for the recurrent connection strength variants experiment below. See the example in Figure 2.3.

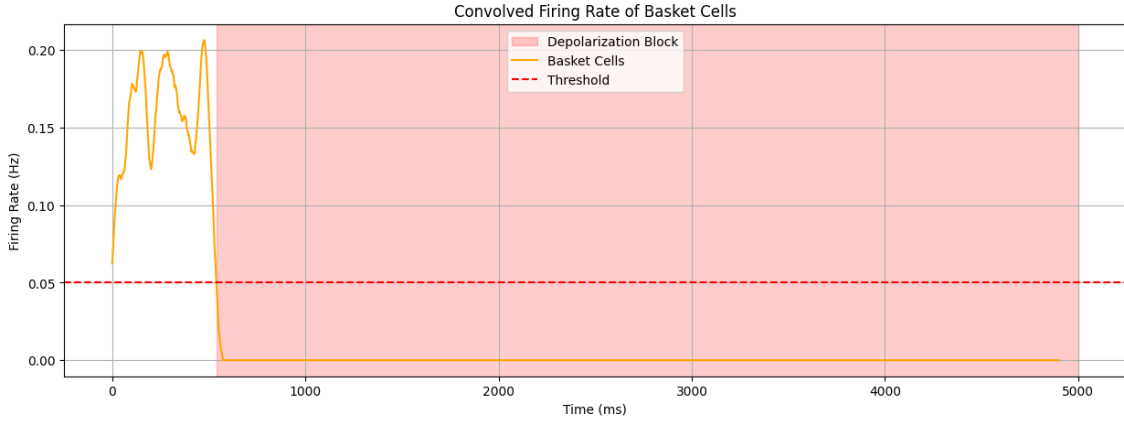


Figure 2.3: Depolarization block in basket cells. Example of a single trial where a depolarization block is found in the convoluted spike activity signal as a flat-line at 0 Hz. The firing rate is in Hz (y-axis) and the signal is calculated over the entire duration of the trial (5000 ms). Note that the signal has to pass the threshold for an extended period of 100 ms to be considered a DPB. In addition, the first 50 ms are excluded from detection to avoid false positives. This detection method was done for each individual trial.

Analysis of External Noise Variants

This section elaborates on the methodological approach undertaken to assess the impact of varying levels of external noise on pyramidal cells, with the aim of understanding its influence on depolarization block occurrences within the network. The experiment's premise was based on the hypothesis that adjusting the external noise could modulate the epileptic state, characterized by depolarization blocks, within the neural network.

The analysis was structured as follows:

1. **Event Detection and Quantification:** For each variant of external noise levels, depolarization events were systematically identified. These results were quantified per trial. This process involved the enumeration of depolarization events, accumulation of their start and end times, and the computation of the overall duration of these events within each trial.
2. **Statistical Analysis:** Subsequent to the detection of depolarization events, the analysis proceeded with the calculation of average event duration and the computation of the percentage of trials exhibiting depolarization blocks. Furthermore, the mean delay and standard deviation for the onset of depolarization events were determined to gauge the temporal dynamics of the network's response to varying noise levels.
3. **Data Visualization:** To concisely present the findings, the analysis results were visualized through matrix plots. These plots delineated the relationship between pyramidal conductances (g_{Na} and g_K) and the observed network behavior under different external noise conditions. The visualizations highlighted the proportion of trials with depolarization blocks and detailed the temporal onset characteristics of these events, facilitating an intuitive understanding of the network's epileptic susceptibility.

The investigative focus on external noise variants sought to delineate the conditions under which the network transitions into an epileptic state, as indicated by the presence of depolarization blocks and the average delay in the onset of a DPB (including STD).

2.5.5 External noise: Burst analysis

Further analysis was conducted to investigate the burst dynamics of pyramidal and basket cell activity based on the observations done in the initial increased noise experiment. This experiment involved looking at the temporal shift in detected bursts surrounding the onset of a depolarization block event in the basket cell population.

Detection of Epileptiform Activity and Burst Analysis

This experiment employed leveraging convolved spike activities and burst detection within neural populations to detect epileptiform activity. The approach was predicated on analyzing the temporal dynamics of neuronal firing rates, specifically focusing on the basket and pyramidal cell populations. A critical aspect of this analysis was the identification and analysis of bursts in relation to the onset of depolarization blocks (DPBs), including the possible variance in burst intensity.

The unified methodology proceeded as follows:

- **Identification of Depolarization Block Onset:** A custom python function `find_depolarization_block` was employed to scan the simulation data for periods devoid of spiking activity within a specified window across basket cell populations. This step was crucial in pinpointing the initial point of a depolarization block, thus serving as a reference for the subsequent analysis.
- **Preparation and Convolution of Spike Activities:** Spike times were aggregated and subjected to a Gaussian filter, smoothing the data to represent neural firing rates over time effectively. This step facilitated the identification of significant patterns in relation to the DPB onset.
- **Burst Detection and Temporal Analysis:** The convolved spike activities were analyzed using a burst detection algorithm, identifying significant increases in activity as bursts. These were classified based on their occurrence relative to the DPB onset—focusing on the last burst before, the second-last burst before, and the first burst after the onset. This classification shed light on the changes in neural dynamics preceding and following a depolarization block.
- **Analytical Assessment and Summarization of Findings:** Start and end times were determined for detected bursts, as well as peak activity levels. This comprehensive analysis of convolved spike activities and burst dynamics provided a detailed view of the neural mechanisms during critical phases of epileptiform activity.

The experiment utilized a 100 ms window and a 0.1 ms time step throughout the 5000 ms simulation duration, resulting in 50,000 indices for spike detection. The absence of basket cell firing within this window indicated a DPB, which was critical for burst detection. This methodology offered a nuanced understanding of epileptiform dynamics, highlighting the transitions of neural populations into and out of depolarization blocks which are indicative of epileptic activity in the network. Note that in the burst analysis the 1D-Gaussian convolution was performed on a histogram of the spike times of cells. Whereas in the previous convolution for the matrices, the convolutions were performed using a binary time series of the spike times.

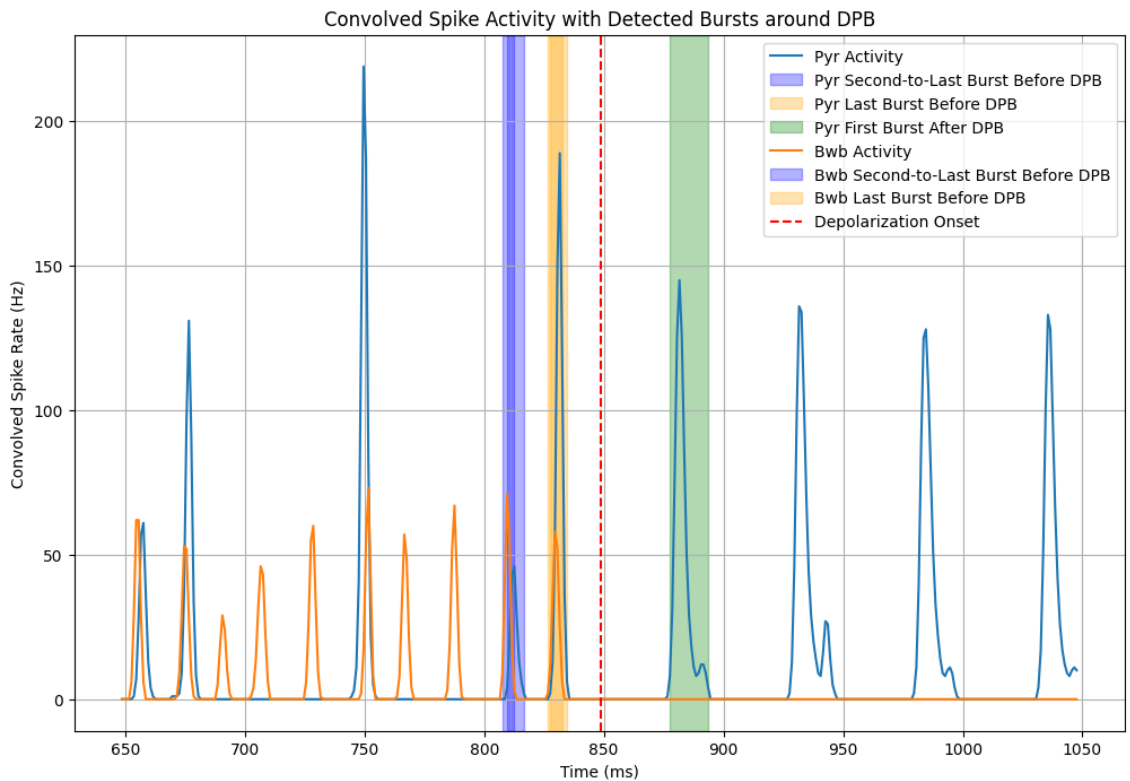


Figure 2.4: Burst detection example. Example of a single trial where bursts in the neural populations are detected near the onset of a DPB using convoluted spike activity signals. The firing rate is in Hz (y-axis) and the signal is calculated over the entire duration of the trial (5000 ms). The onset of a depolarization block in basket cells is indicated by a red dashed vertical line. The last and second to last bursts before, and the first burst after the DPB were detected and used for analysis. Note that the signal has to pass the threshold for an extended period of 100 ms to be considered a DPB. In addition, the first 50 ms are excluded from detection to avoid false positives. This detection method was done for each individual trial.

2.5.6 Recurrent connection strength variants

This section describes the methodology employed to analyze the effects of varying recurrent connection strengths between basket cells on the incidence and characteristics of depolarization blocks within the network. This analysis aimed to explore the potential of modulating soma inhibition strength to mitigate epileptic activity and restore baseline network dynamics.

The experiment adjusted the recurrent connection strength across a range of multipliers (1.00, 1.05, 1.10, 1.15, and 1.20 times the baseline), concurrently with modifications to g_{Na} and g_{K} within a plus or minus 25% range of the baseline. The connection weight from O-LM cells to pyramidal cells was fixed at 10%, facilitating the induction of depolarization blocks under a 20x external noise condition on pyramidal cells. A total of 15 trials were conducted for each condition, and the results were averaged for analysis.

Analysis of Recurrent Connection Strength Variants

The analysis procedure was as follows:

1. **Event Detection and Aggregation:** The analysis began by identifying depolarization events across trials for each variant of the recurrent connection strength. This involved counting the number of depolarization events, their start and end times, and the total duration of depolarization within each trial. Trials devoid of depolarization events were separately tallied.
2. **Statistical Computation:** For trials exhibiting depolarization events, the average duration of these events was calculated. Additionally, the percentage of trials manifesting depolarization events and the statistical measures (mean and standard deviation) concerning the onset times of these events were determined.
3. **Matrix Visualization:** The analyzed data were visualized using matrix plots to illustrate the relationship between the recurrent connection strength variants and the properties of depolarization events under different g_{Na} and g_{K} conditions. These plots highlighted the percentage of trials with depolarization blocks and the count of depolarization events, offering insights into the efficacy of soma inhibition strength adjustments in modulating epileptic activity.

This analytical approach facilitated a comprehensive examination of the impact of modifying recurrent connection strengths among basket cells on the network's susceptibility to epileptic disruptions. Through statistical and visual analyses, the dynamics governing epileptiform activity and the potential for intervention was investigated through targeted manipulation of inhibition mechanisms within the neural circuitry.

For detecting depolarization blocks in the basket cell population, the methodology was as follows:

- Establishing a signal threshold indicating a depolarization block.
- Excluding initial transient analysis to prevent false positives.
- Identifying threshold crossings that mark the start and end of depolarization blocks.
- Applying a minimum duration filter to these blocks.
- Summarizing and reporting the total duration of all valid depolarization blocks in the trial.

A check was performed if the convoluted signal remained beneath a fixed threshold of 0.001 for at least 100 ms. This threshold was defined non-zero, yet tiny as in the depolarization block there are no firing neurons in the basket population. The first 50 ms of the signal were excluded to avoid false positives. If the signal remained beneath the threshold for at least 100 ms, the condition was considered to be in a depolarization block state. This was done for each trial individually. An example of this can be seen in Figure 2.3.

3 Results

3.1 Results of the Baseline activity

In the initial experiment, the baseline activity of the CA3 network was observed from the *original model* by Sanjay et al. (2015). The network was simulated for 5000 ms and showed synchronous activity throughout all three populations (pyr, BC and OLM). Basket cells showed a higher firing rate compared to the pyramidal cells and O-LM cells. The basket cells also swapped between states of synchrony and asynchrony which was not observed in the other two populations. The O-LM cells showed the lowest firing rate compared to the pyramidal cells and basket cells. The baseline activity of the CA3 network is shown in Figure 3.1.

The average firing rates of the populations were 2.36 ± 0.024 Hz for pyramidal cells, 16.05 ± 0.15 Hz for basket cells, and 0.96 ± 0.027 Hz for O-LM interneurons, similar to observed results from Neymotin et al. (2011) which used the same model on which the Sanjay model is based upon.

Just as reported in the original article, the network produces theta-modulated gamma oscillations within the local field potential (LFP). These oscillations were influenced by signals from the Medial Septum (MS). The gamma oscillations emerged from the inhibitory connections between basket cells that inhibit somas of pyramidal and O-LM cells, as well as interactions among basket cells themselves. Conversely, theta oscillations were the result of interactions between pyramidal cells and O-LM cells that inhibit dendrites. The network achieved a consistent theta frequency of 6.7 Hz due to periodic inputs from the MS to both O-LM and basket cells every 150 ms. The frequency of the gamma component within the LFP was approximately 33 Hz. Despite receiving similar MS inputs as O-LM cells, the impact on basket cells was significantly reduced because of their mutual interactions and the enhanced influence from pyramidal cells.

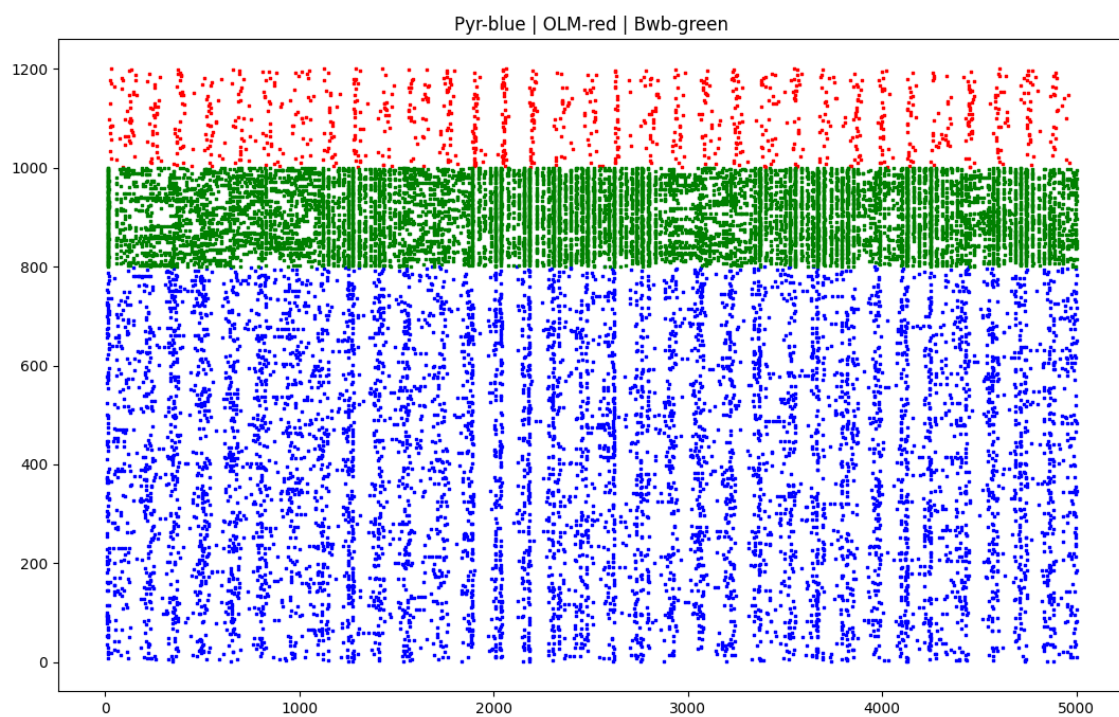


Figure 3.1: Baseline activity of the CA3 network. The above figure shows the baseline activity of the CA3 network. The network was simulated for 5000 ms. The spike activity in time of the Pyr cells, BC cells, and OLM cells are shown based on the Neuron ID. ID 0–799 = Pyramidal (blue), 800–999 = BC (green), 1000–1200 = OLM (red). The x-axis represents the time in ms and the y-axis represents the neuron ID.

3.2 Results of the Model validation

To test whether our implementation of the CA3 network was able to replicate more elaborate results, results from Figure 6 of the original Sanjay et al. (2015) article were replicated in Figure 3.4, 3.5 and 3.6.

Like in the original experiment, O-LM-pyramidal connectivity was decreased in decrements of 0.1 and reduced dendritic inhibition. Simultaneously, external noise fed to pyramidal cells via AMPA and NMDA at the synaptic level was increased in increments of 0.1. When O-LM-pyramidal connectivity was decreased to a range of 20–10 %, desynchronization was observed among basket cells (Figure 3.2). Complete desynchronization was observed when the O-LM-pyramidal connectivity was reduced to 0 % (Figure 3.3). Pyramidal to O-LM connectivity was unchanged, thus these cells showed sustained synchronous activity.

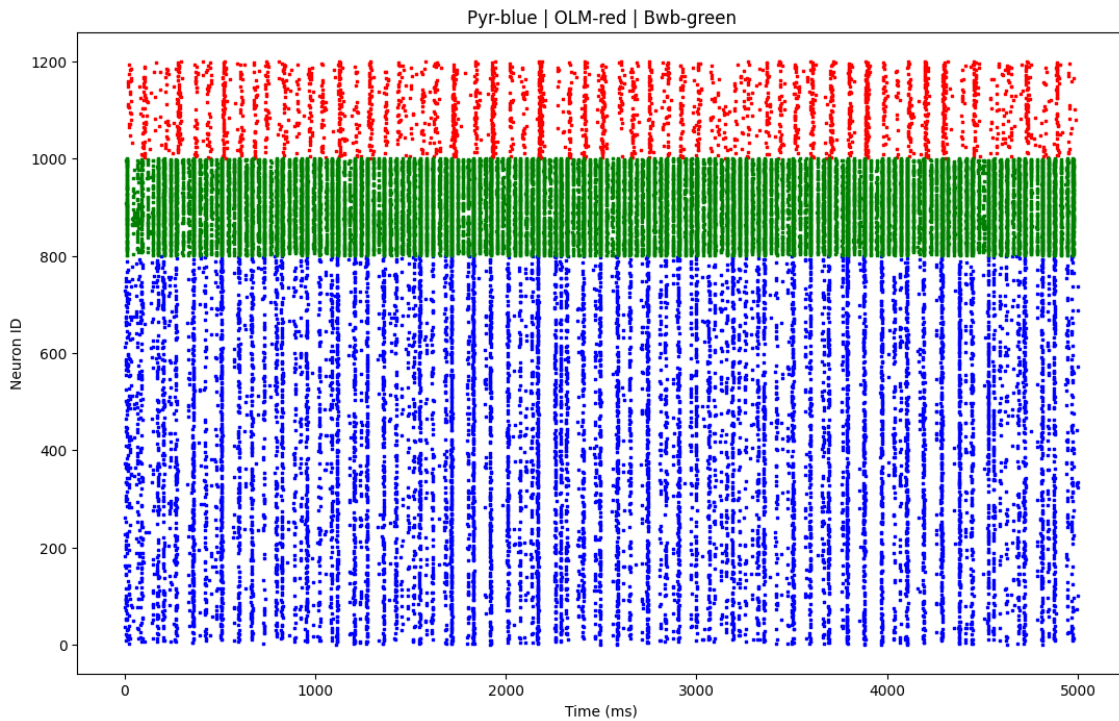


Figure 3.2: Scatter plot of the network activity at 20 % OLM-Pyr connection
The above figure shows the network activity at 20 % OLM-Pyr connection with significant asynchrony amongst the basket cells. The network was simulated for 5000 ms. The scatter plot shows the spike activity of the Pyr cells (blue), BC cells (green), and OLM cells (red). The x-axis represents the time in ms and the y-axis represents the neuron ID.

The results show that the model was able to replicate the results of the original article with slightly lower firing rates, theta-gamma frequencies and power, which can be seen in table 3.1. The original article results are visible in the methods section in table 2.3 for comparison.

For the firing rates in Figure 3.4, there was a notable increase in the firing rates of all neuron types as dendritic inhibition was decreased while external noise was simultaneously increased. The individual cell firing frequencies showed a near linear increase throughout in both pyramidal and O-LM cells, being most pronounced

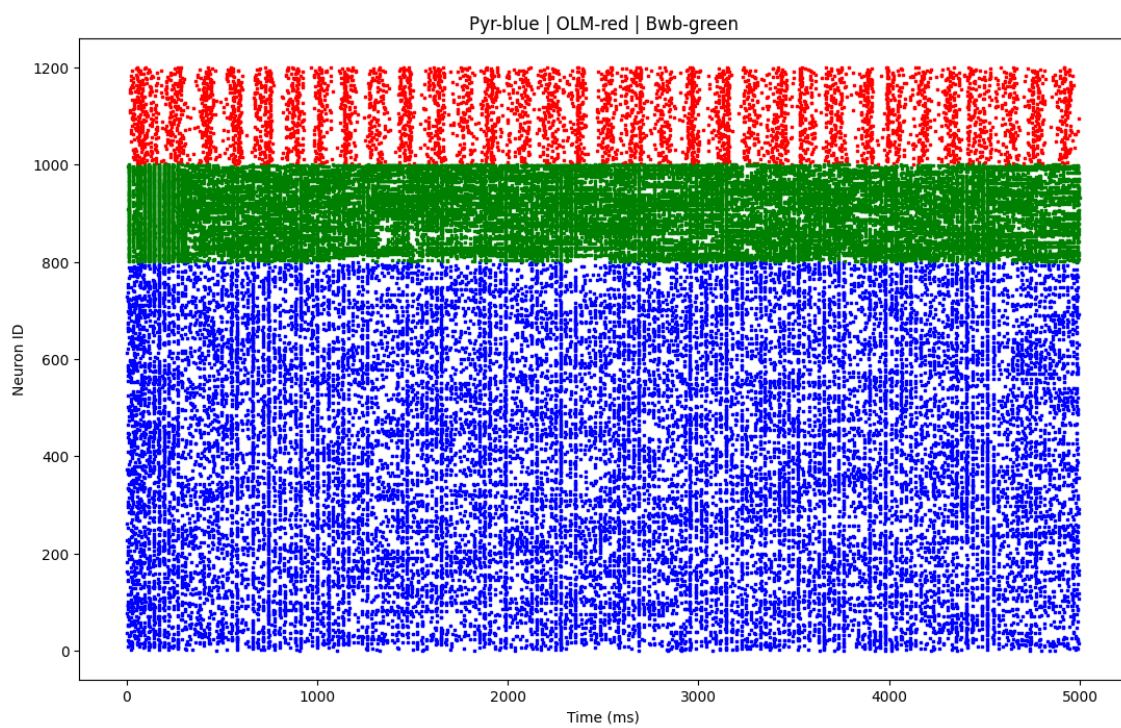


Figure 3.3: Scatter plot of the network activity at 0 % OLM-Pyr connection. The above figure shows the network activity at 0 % OLM-Pyr connection with complete asynchrony amongst the basket cells. The network was simulated for 5000 ms. The scatter plot shows the spike activity of the Pyr cells (blue), BC cells (green), and OLM cells (red). The x-axis represents the time in ms and the y-axis represents the neuron ID.

in the basket cell population. The basket cell population also showed the most variance in the standard deviation at the most extreme condition from the baseline (0.0x OLM-Pyr weight and 2.0x external weight).

The dominant frequencies in the network activity, as shown in Figure 3.5, showed that the theta frequency remained constant, while the gamma frequency only increased as dendritic inhibition was severely decreased and external noise increased. The theta frequency remained constant at 6.2 Hz, slightly lower than the original model's 6.7 Hz, due to the strong pacing from the MS at this frequency.

The power of the theta and gamma oscillations in the network, as shown in Figure 3.6, showed that the power of theta oscillations decreased, while the gamma power increased as dendritic inhibition was reduced. This shift in power distribution reflects changes in the balance of network excitability and inhibition, potentially leading to epileptic activity. The theta power reduced to $5.35 \text{ mV}^2 \text{ Hz}^{-1}$ to $0 \text{ mV}^2 \text{ Hz}^{-1}$. The gamma power increased significantly from at 20 to 10 % O-LM-pyramidal connection. The gamma power increased from $0.93 \text{ mV}^2 \text{ Hz}^{-1}$ at baseline to $5.82 \text{ mV}^2 \text{ Hz}^{-1}$ before dropping down to $1.87 \text{ mV}^2 \text{ Hz}^{-1}$ in the last condition. The gamma power was mostly due to basket cell activity, which were much more tightly synchronized than the other cell types.

The trends in the original figures were similar in Figure 2.2 to the ones of this section. Therefore, it was assumed that the model was correctly implemented and the results were valid.

Table 3.1: Overview of Model Validation Network Simulation Settings and Outcomes. Variations in the firing rates of cell populations, alongside theta and gamma oscillations within the local field potential, as well as the alterations in their intensity upon the decrease of dendritic inhibition and the concurrent enhancement of external stimuli to the pyramidal neurons.

OLM-Pyr Wt	External Wt	Pyr (Hz) + Std	BWB (Hz) + Std	OLM (Hz) + Std	Theta Freq (Hz)	Theta power (mV ² Hz ⁻¹)	Gamma Freq (Hz)	Gamma power (mV ² Hz ⁻¹)
1.0X	1.0X	1.83 ± 0.58	9.21 ± 2.20	1.08 ± 0.38	6.2	1.67	32.8	0.93
0.9X	1.1X	2.00 ± 0.64	10.67 ± 2.31	1.15 ± 0.36	6.2	2.08	34.4	1.36
0.8X	1.2X	2.00 ± 0.71	11.54 ± 2.72	1.22 ± 0.39	6.2	1.67	34.4	1.74
0.7X	1.3X	2.14 ± 0.74	13.24 ± 2.36	1.29 ± 0.42	6.2	2.06	32.8	2.37
0.6X	1.4X	2.33 ± 0.79	15.04 ± 2.35	1.44 ± 0.45	6.2	2.13	32.8	2.76
0.5X	1.5X	2.41 ± 0.80	16.44 ± 2.31	1.53 ± 0.45	6.2	2.02	32.8	3.68
0.4X	1.6X	2.57 ± 0.79	17.88 ± 2.12	1.76 ± 0.45	6.2	2.03	31.2	4.44
0.3X	1.7X	2.74 ± 0.86	19.04 ± 2.38	2.10 ± 0.49	6.2	1.55	31.2	4.68
0.2X	1.8X	2.97 ± 0.88	20.61 ± 2.14	2.44 ± 0.48	6.2	0.92	31.2	4.87
0.1X	1.9X	3.59 ± 0.99	20.98 ± 2.62	3.31 ± 0.50	6.2	0.78	32.8	5.82
0.0X	2.0X	5.50 ± 1.52	21.46 ± 7.93	4.90 ± 0.52	4.7	0.04	39.1	1.87

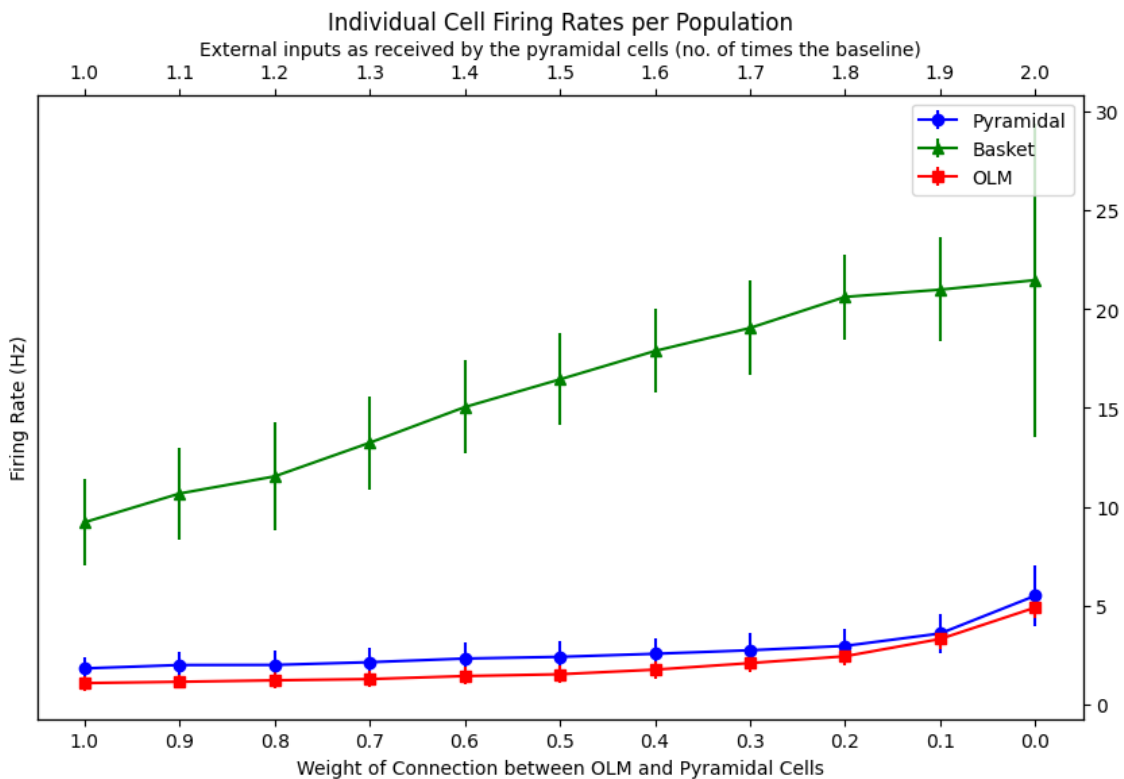


Figure 3.4: Validation of the firing rates. The above figure shows the firing rates of the Pyr cells, BC cells, and O-LM cells when dendritic inhibition is decreased and external noise is increased. The firing rates were calculated from the spike activity of the cells in each population for the duration of the simulation (5000 ms). The double x-axis represents both decrement in the weight of dendritic inhibition on pyramidal cells by OLM interneurons, while simultaneously increasing external noise stimulation to pyramidal cells. External noise levels rise and inhibition decreases by increments of 0.1, each representing a 10% change relative to the baseline. The y-axis represents the firing rate in Hz. The firing rates are per cell type: Pyr (blue), Basket (green) and OLM (red). The error bars represent the standard deviation of the firing rates.

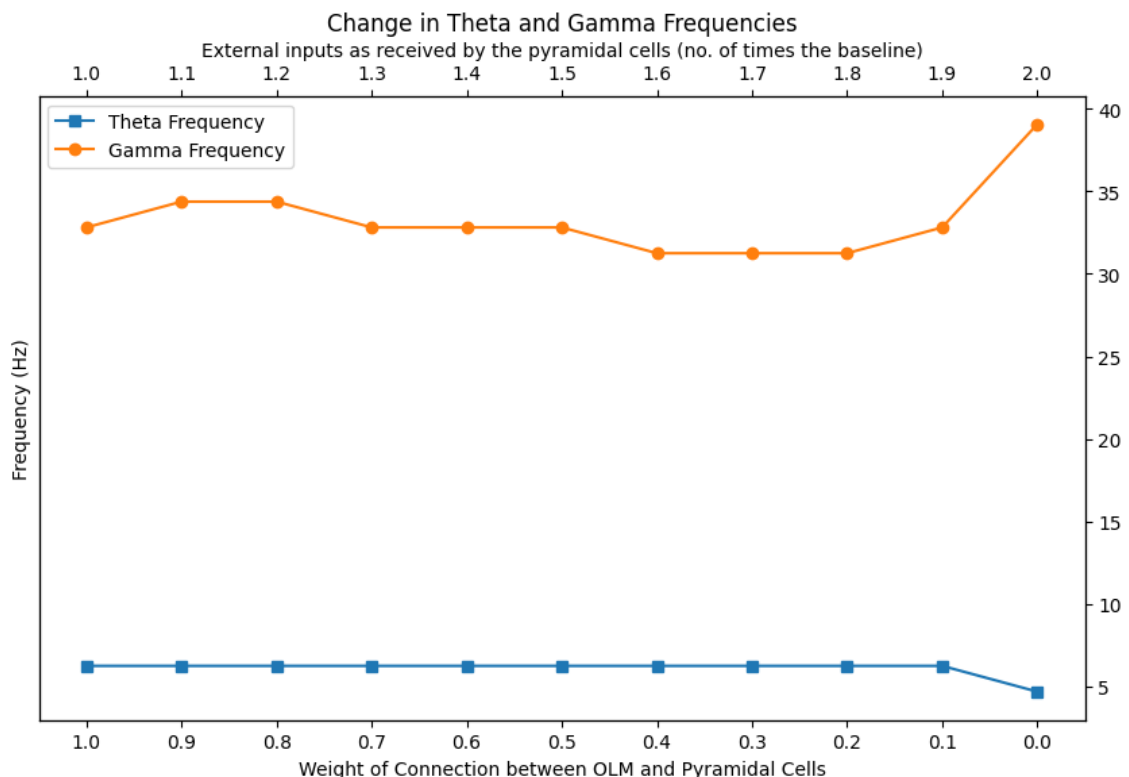


Figure 3.5: Validation of dominant frequencies. The above figure shows the dominant theta-gamma frequencies in the network activity when dendritic inhibition is decreased and external noise is increased. The double x-axis represents both decrement in the weight of dendritic inhibition on pyramidal cells by O-LM interneurons, while simultaneously increasing external noise stimulation to pyramidal cells. External noise levels rise and inhibition decreases by increments of 0.1, each representing a 10% change relative to the baseline. The y-axis represents the dominant frequency in Hz for both theta (3–12 Hz, blue) and gamma (30–80 Hz, orange) oscillatory bands.

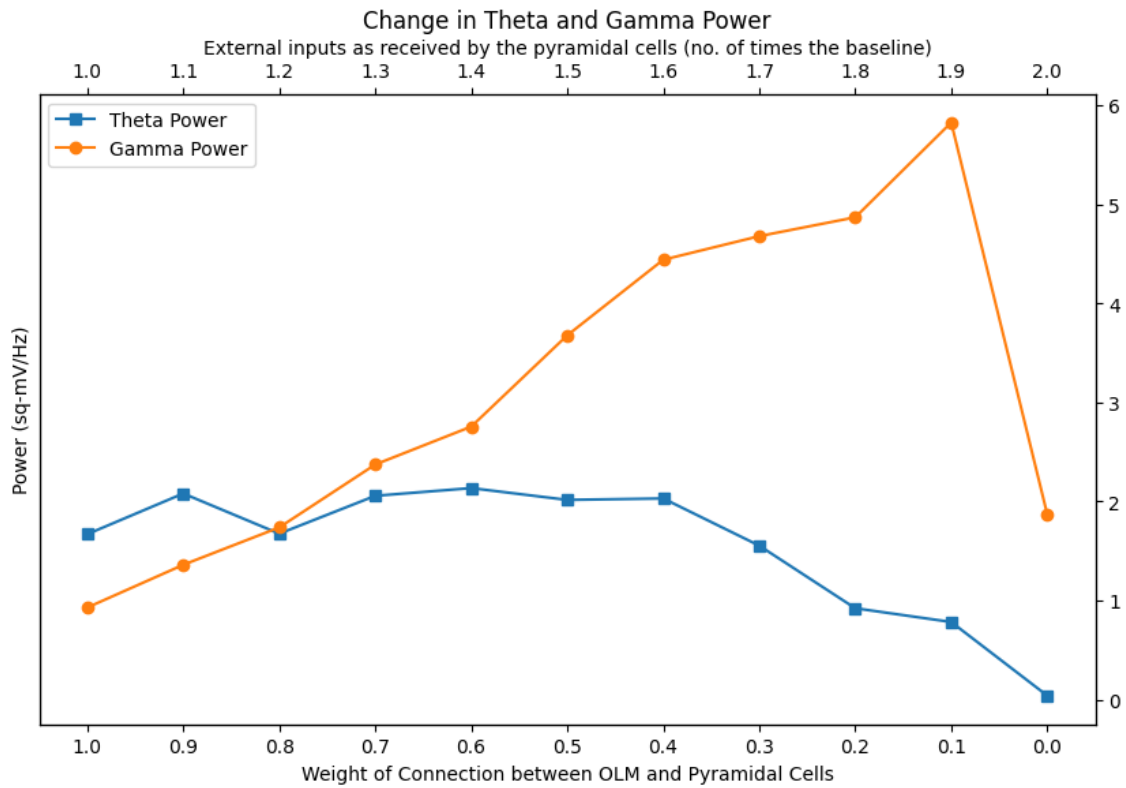


Figure 3.6: Validation of Theta-Gamma power. The above figure shows the power of the theta and gamma oscillations in the network when dendritic inhibition is decreased and external noise is increased. The double x-axis represents both decrement in the weight of dendritic inhibition on pyramidal cells by O-LM interneurons, while simultaneously increasing external noise stimulation to pyramidal cells. External noise levels rise and inhibition decreases by increments of 0.1, each representing a 10% change relative to the baseline. The y-axis represents the theta and gamma power (blue and orange, respectively).

3.3 Results of the Sodium-Potassium variants

In this experiment, the sodium and potassium conductance of the pyramidal, basket, and O-LM cells were modified in increments of 0.1. This was done in a range of 0.5 to 1.5 times the baseline conductance. Similarly to the previous experiment, the network was simulated for 5000 ms and the firing rates, dominant frequencies, and power of the theta and gamma oscillations were calculated in Figures 3.7, 3.8 and 3.9, respectively. Baseline firing rates for all cells in both conditions were 1.87 ± 0.60 Hz for pyramidal cells, 9.13 ± 2.26 Hz for basket cells and 1.06 ± 0.36 Hz for O-LM cells (see Tables B.1-B.6 in appendix B).

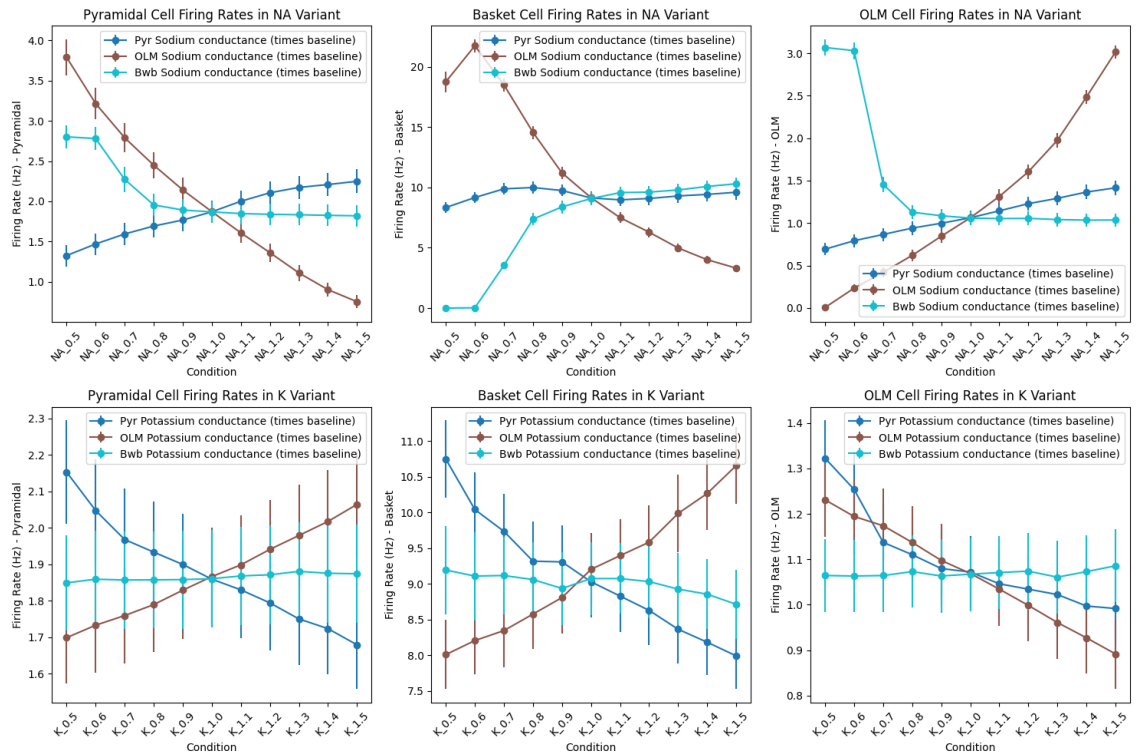


Figure 3.7: Sodium-Potassium variants: Firing rates per population. The above figure shows the firing rates of the Pyr cells, BC cells, and O-LM cells for each modified cell type. Each of the three cell types either had modified sodium or potassium conductance. The firing rates were calculated from the spike activity of the cells in each population for the duration of the simulation (5000 ms). The x-axis represents the percentage amount of changed sodium or potassium conductance, times the baseline. The y-axis represents the firing rate in Hz. The firing rates are per cell type: Pyr (blue), Basket (cyan) and OLM (red). The error bars represent the standard error of the mean (SEM) of the firing rates per population.

3.3.1 Firing rates: Pyramidal cells

In Figure 3.7, the firing rates of pyramidal cells showed the largest change when the sodium conductance (g_{Na}) of O-LM cells was modified. When the sodium conductance of O-LM cells (dendrite-inhibiting) was decreased, the firing rate of pyramidal cells increased, and vice versa. Sodium conductance of basket cells (soma-inhibiting)

was also modified. Interestingly, the firing rate of pyramidal cells was unaffected when g_{Na} was increased. However, when g_{Na} was decreased by more than 30 % the firing rate of pyramidal cells increased sharply. Lastly, increasing the g_{Na} in the pyramidal cells themselves led only to a marginal in- and decrease in firing rates.

Changing the potassium conductance (g_K) had more profound effects on pyramidal firing rates. When the potassium conductance of O-LM cells was increased, the firing rate of pyramidal cells decreased, and vice versa. Changing g_K of basket cells had almost no effect on the firing rate of pyramidal cells. However, when the potassium conductance of pyramidal cells was modified, the effect of potassium on the pyramidal firing rates were almost the exact opposite of modified the O-LM cells.

3.3.2 Firing rates: Basket cells

Compared to pyramidal cell firing rates, the basket cell population has some significantly different trends in firing rates. When the g_{Na} of O-LM cells was modified, the firing rate of basket cells decreased, and vice versa. Interestingly, at -40 % g_{Na} of O-LM the firing rate peaks and then decreases sharply, instead of a linear decrease. Changing the g_{Na} of pyramidal cells had barely any effect on the firing rate of basket cells. Whereas changing the g_{Na} of basket cells themselves, led to a sharp decrease in firing rate at -30 % g_{Na} and a complete loss of firing at a -40 % g_{Na} . Generally, the firing rates were much higher and the effects on the firing rates were more pronounced compared to the pyramidal cells and O-LM cells (with the largest SEM).

Changing the g_K of basket cells had a similar effect to that of pyramidal population, albeit with larger in- and decreases in Hz. Just like the pyramidal firing rates, the basket firing rate increases when O-LM g_K is increased and vice versa. The firing rate of basket cells was unaffected when the g_K of basket cells was modified. Whereas increasing the g_K of pyramidal cells led to a decrease of basket cell firing rate and vice versa.

3.3.3 Firing rates: O-LM cells

The O-LM population showed the most unique variations in firing rates. When the g_{Na} of O-LM cells was modified, the firing rate of O-LM cells increased, and vice versa. However, when the g_{Na} of basket cells was decreased below -30 %, the firing rate of O-LM cells increased sharply to more than double the Hz. Pyramidal g_{Na} had a weak and linear effect on the O-LM firing rates, where increased g_{Na} led to increased firing rates and decreased g_{Na} led to decreased firing rates.

Changing the g_K of O-LM cells had an inverted effect on firing rates compared to g_{Na} . Modifications to basket cell g_K , again, had little to no effect on the firing rate of O-LM cells. However, when the g_K of pyramidal cells was modified, the effect on the O-LM firing rates was almost the same as the O-LM g_K modifications.

3.3.4 Dominant frequencies

In this experiment the dominant theta and gamma frequencies were identified from the local field potential (LFP) for the duration of the simulation (5000 ms) by performing a power spectrum density analysis. The dominant frequencies were calculated for each modified cell type and are shown in Figure 3.8. The figure is split in both sodium and potassium conductance modifications for each cell type (pyramidal = blue, OLM = red, basket = cyan).

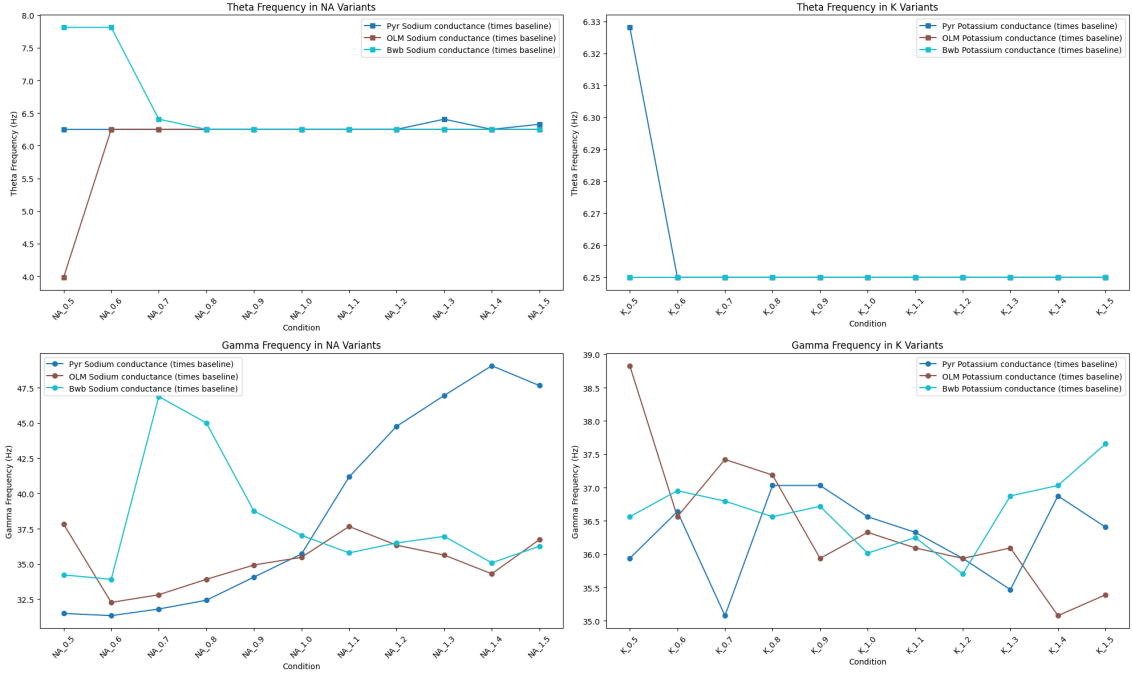


Figure 3.8: Sodium-Potassium variants: Dominant frequencies. The above figure shows the dominant theta-gamma frequencies in the network activity for each modified cell type. Each of the three cell types either had modified sodium or potassium conductance (pyr = blue, OLM = red, basket = cyan). The dominant frequencies were calculated from the local field potential (LFP) for the duration of the simulation (5000 ms). The x-axis represents the percentage amount of changed sodium or potassium conductance, times the baseline. The y-axis represents the dominant frequency in Hz for both theta (3–12 Hz) and gamma (30–80 Hz) oscillatory bands.

Theta frequency

For both sodium and potassium conductance modifications, the theta frequency was largely unaffected as it is generated by the strong pacemaker influence of the medial septum at the 6.2 Hz frequency. There were a couple of outliers in both conditions, in the -50 % conditions of O-LM and basket g_{Na} , is decreased and increased respectively (3.8, top left = sodium theta, right = potassium theta).

Gamma frequency

Conversely, the gamma frequency was more affected by the sodium and potassium conductance modifications. In the modified pyramidal condition the gamma frequency increased sharply from -50 % to 50 % g_{Na} from 30.4 hz to 48.8 Hz. O-LM

modifications in comparison, had a less significant effect on the gamma frequency, with a slight increase from the baseline at 10 % increased g_{Na} . Basket cell modifications had the most significant effect on the gamma frequency, with a sharp increase of more than 10 Hz from -40 % g_{Na} to -30%. It sharply decreases nearing baseline, at which increased g_{Na} of basket cells had very little effect on the gamma frequency (3.8, bottom left).

The effects of potassium on gamma frequency seems to more random without a clear trend in in- or decrease of conductance for all cell types. Each increment of 0.1 appeared to have a different effect on the gamma frequency, with some conditions showing a sharp increase or decrease in Hz. The power of the gamma frequency stayed mostly within the 35.5 to 37.5 Hz range (3.8, bottom right).

3.3.5 Theta-gamma power

Another aspect of the sodium-potassium experiment was a power analysis of the theta and gamma oscillations in the network based on the power spectrum density. The power of the theta and gamma oscillations were calculated from the local field potential (LFP) for the duration of the simulation (5000 ms) and are shown in Figure 3.9. The figure is again split in both sodium and potassium conductance modifications for each cell type (pyramidal = blue, OLM = red, basket = cyan).

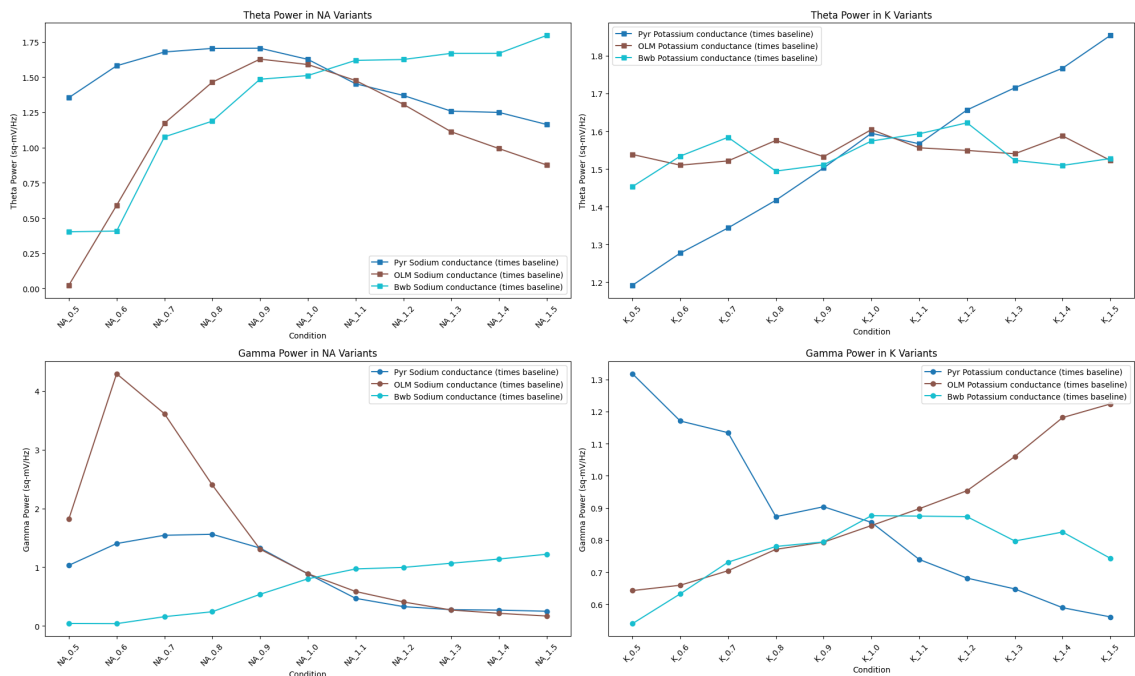


Figure 3.9: Sodium-Potassium variants: Theta-Gamma power. The above figure shows the power of the theta and gamma oscillations in the network for each modified cell type. Each of the three cell types either had modified sodium or potassium conductance (pyr = blue, OLM = red, basket = cyan). The power of the theta and gamma oscillations were calculated from the local field potential (LFP) for the duration of the simulation (5000 ms). The x-axis represents the percentage amount of changed sodium or potassium conductance, times the baseline. The y-axis represents the theta and gamma power (in $\text{mV}^2 \text{ Hz}^{-1}$).

Theta power

Theta power showed an rising trend in all three cell types where O-LM and basket cells had the most significant increase in power in below-baseline conditions. This change in power occurred predominantly in the -50 % to -30 % g_{Na} range. After which, O-LM falls off together with the modified pyramidal condition and decreases slightly. The basket cell condition shows the relative highest theta power above baseline conditions and remained slightly above baseline (3.9, top left).

In the modified potassium conductance conditions only the pyramidal modifications had an almost linear increase in theta power from -50 % to +50 % g_K . Modifications in the other cell types remained fairly constant in theta power (3.9, top right).

Gamma power

Unlike the frequency, the power of the gamma oscillations showed a large spike in power when the O-LM cells were modified from -50 % to -40 % g_{Na} of almost double the power. The effect of which in the LFP power spectrum is visualized using a fast-Fourier transformation in Figure 3.10. From this figure, it is clear that some conditions cause significant shifts in gamma power at specific frequencies (30–40 Hz and 60–70 Hz). The gamma power sharply drops back to a more constant level from baseline onwards. The other cell types show a shift from 1 and 0 Hz to 0 and 1 Hz for Pyramidal and Basket cell modified conditions respectively (3.9, bottom left).

Increased g_K of O-LM cells from -50 % onwards resulted in a constant rise in gamma power in the network, whereas modifications in pyramidal populations resulted in a steady decrease in gamma power. Basket cell modifications had a more random effect on gamma power, with some more extreme conditions reduced gamma power compared to baseline (3.9, bottom right). The gamma power was mostly due to basket cell activity, as the gamma nears 0 $mV^2 \text{ Hz}^{-1}$ as their firing rate nears 0 Hz.

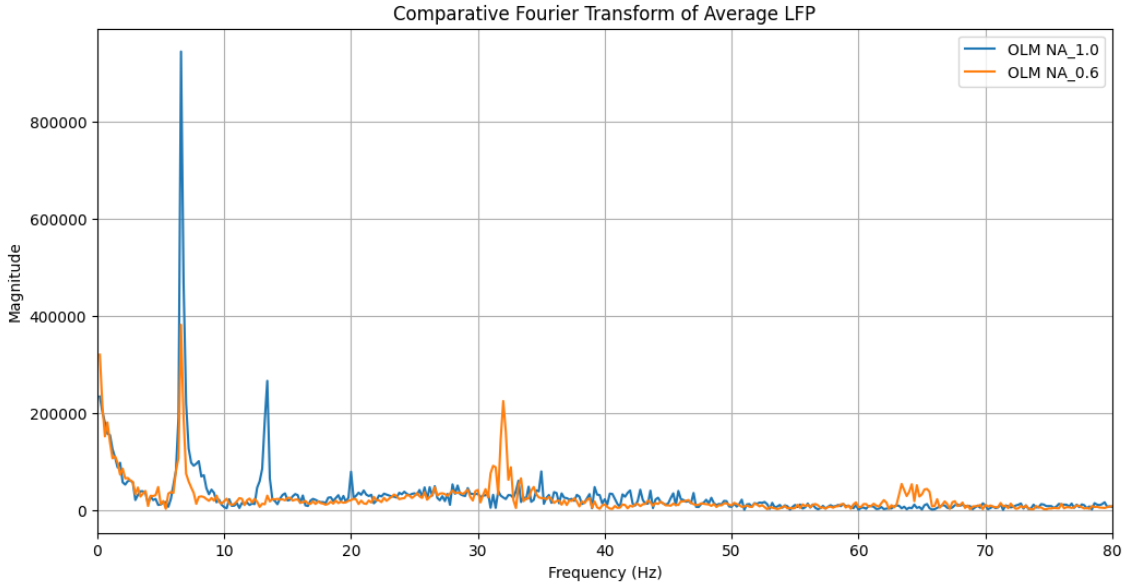


Figure 3.10: Comparative FFT of the LFP for OLM variants. The magnitude of the LFP is in arbitrary units. The signal is plotted for the frequency range that includes both theta and gamma in a range of 0 to 80 Hz. Blue is the baseline LFP, whereas orange represents a -40 % sodium conductance variant of O-LM cells.

3.4 Results of the External Noise variants

As a follow-up to the sodium-potassium experiment, the network's sensitivity to a range of external noise conditions was tested for different combinations of modified pyramidal sodium/potassium conductance. The occurrence of depolarization block events in basket cells were quantified, including the average delay of these events in trials where they occurred. The external noise fed to the pyramidal cells was modified in increments of 0.05, ranging from 0.65 to 0.95 times the baseline noise level.

More noise conditions are available for review in appendix C.

3.4.1 Occurrence of depolarization block events across noise conditions

To test the susceptibility of the network to depolarization block (DPB) events, the percentage of trials where DPB events occurred was calculated in Figure 3.12. The color intensity of the matrices indicate how often the network entered an epileptic state per noise condition for different combinations of pyramidal cell modifications of sodium and potassium. At baseline sodium-potassium conductance and 20 times noise the network response is visible with a clear depolarization block in basket cells in Figure 3.11.

In matrix a in Figure 3.12, there were barely any DPB events in the 15 trials per condition. Most of the DPB events occurred near baseline g_{Na} and g_K conditions and with elevated g_K only.

In matrix b, the number of DPB events increased significantly, with the most

events occurring at elevated pyramidal sodium conductance conditions.

Matrix c showed a similar trend to matrix b, with more DPB events occurring also at more severely elevated pyramidal potassium conductance conditions.

Matrix d showed the most DPB events, with the most events occurring at elevated pyramidal sodium conductance conditions with the exception of severely reduced sodium and potassium conductance combinations (bottom left). The selected noise levels are a percentage of the fixed 20x times baseline external noise level (0.65, 0.75, 0.85, 0.95).

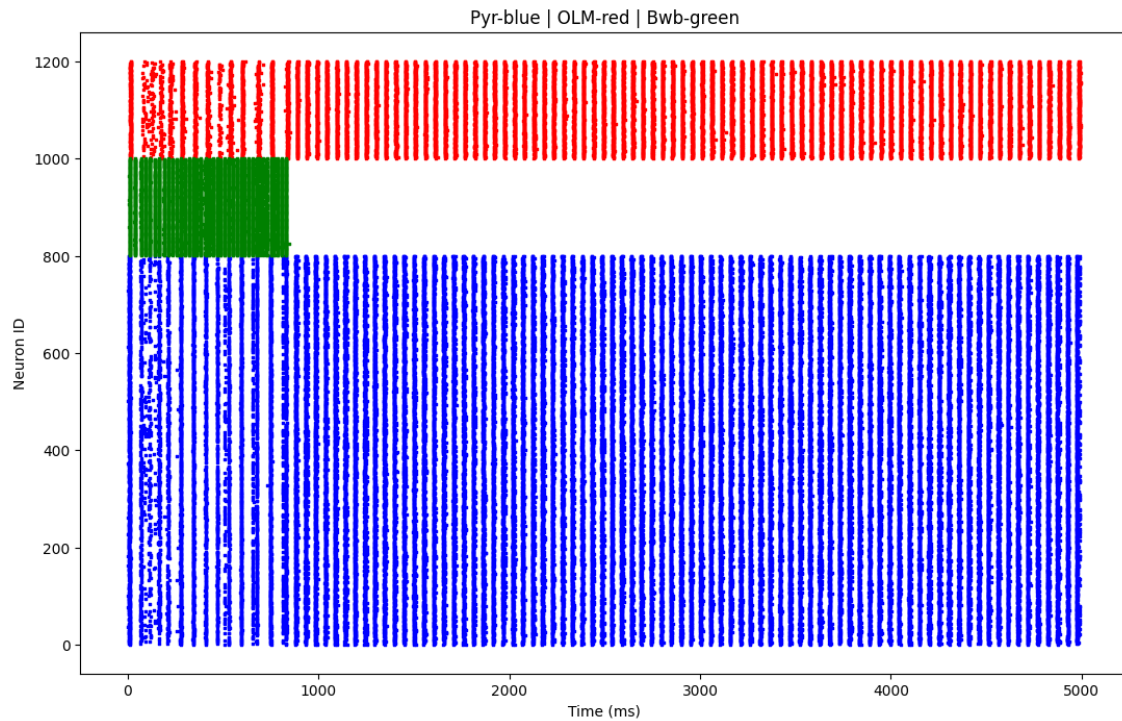


Figure 3.11: Scatter plot of the network activity at 10 % O-LM-Pyr connection with increased external noise (20x times baseline). The above figure shows the network activity at 10 % O-LM-Pyr connection with a depolarization block in the basket cell population. There is a clear ictal-tonic pattern in the population activity, along with very high synchronous spiking between O-LM and Pyr cells. The network was simulated for 5000 ms. The scatter plot shows the spike activity of the Pyr cells (blue), BC cells (green), and O-LM cells (red). The x-axis represents the time in ms and the y-axis represents the neuron ID.

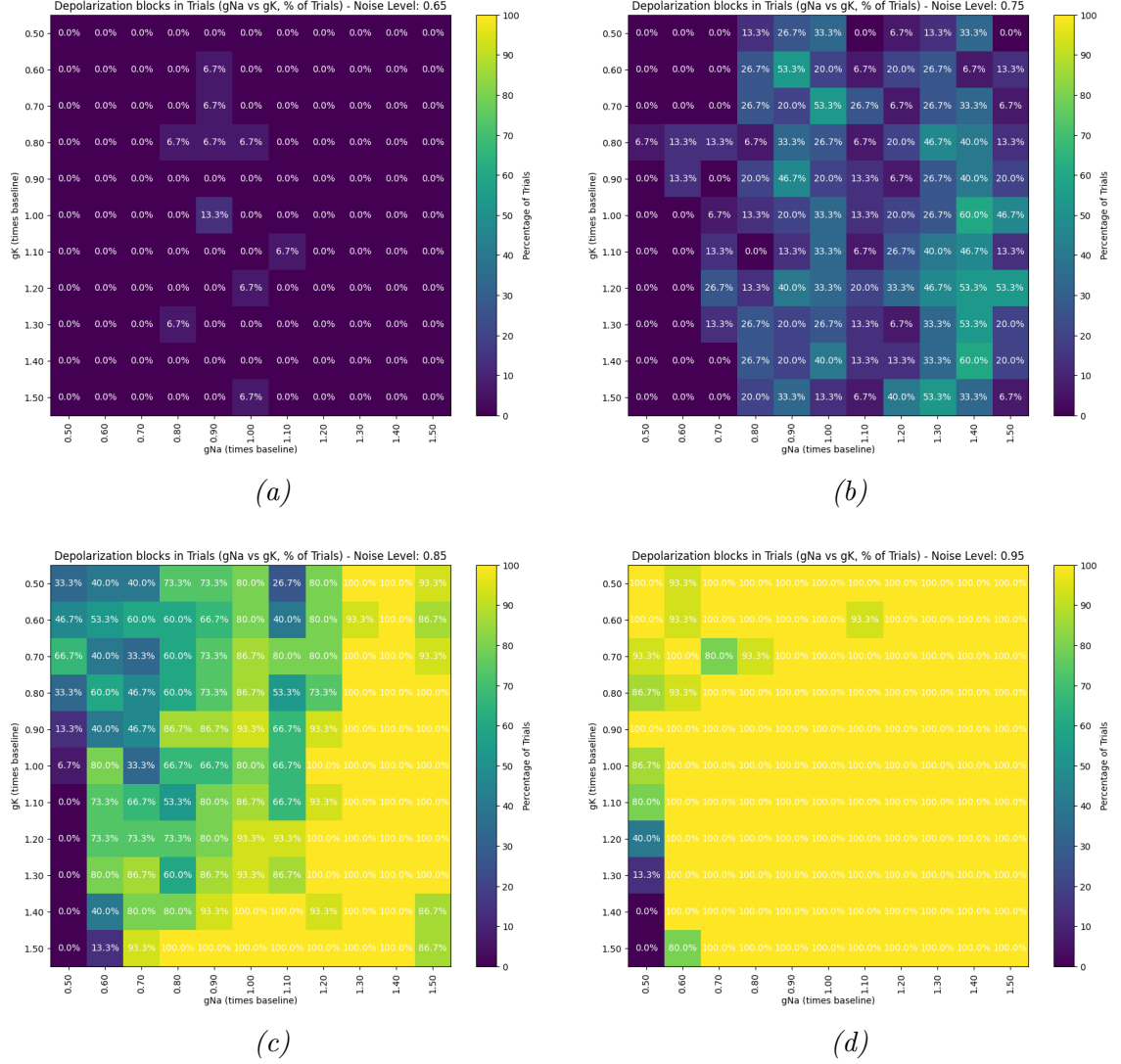


Figure 3.12: Percentage of trials where depolarization block events occurred for all tested noise conditions. The x-axis shows all the sodium conductance changes in pyramidal cells, whereas the y-axis shows the potassium conductance changes in pyramidal cells. Modifications to pyramidal cells were applied to all compartments. The color intensity scales from 0 to 100 %, where high-intensity yellow equals a higher amount of DPB events in a condition. The images are labeled from low noise to higher noise (a through d), respectively.

3.4.2 Average delay of depolarization block events across noise conditions

The average delay (+ standard deviation) of depolarization block (DPB) events was calculated in trials where these events occurred in Figure 3.13. These matrices showed similar trends to the DPB percentage matrices, with the average delay of DPB events being the shortest in the conditions where the most DPB events occurred. These same conditions are associated with the shortest average delay of DPB events and least standard deviation (3.13, c and d). The selected noise ranges are the same as in the percentage matrices, a percentage of the fixed 20x times

baseline external noise level (0.65, 0.75, 0.85, 0.95).

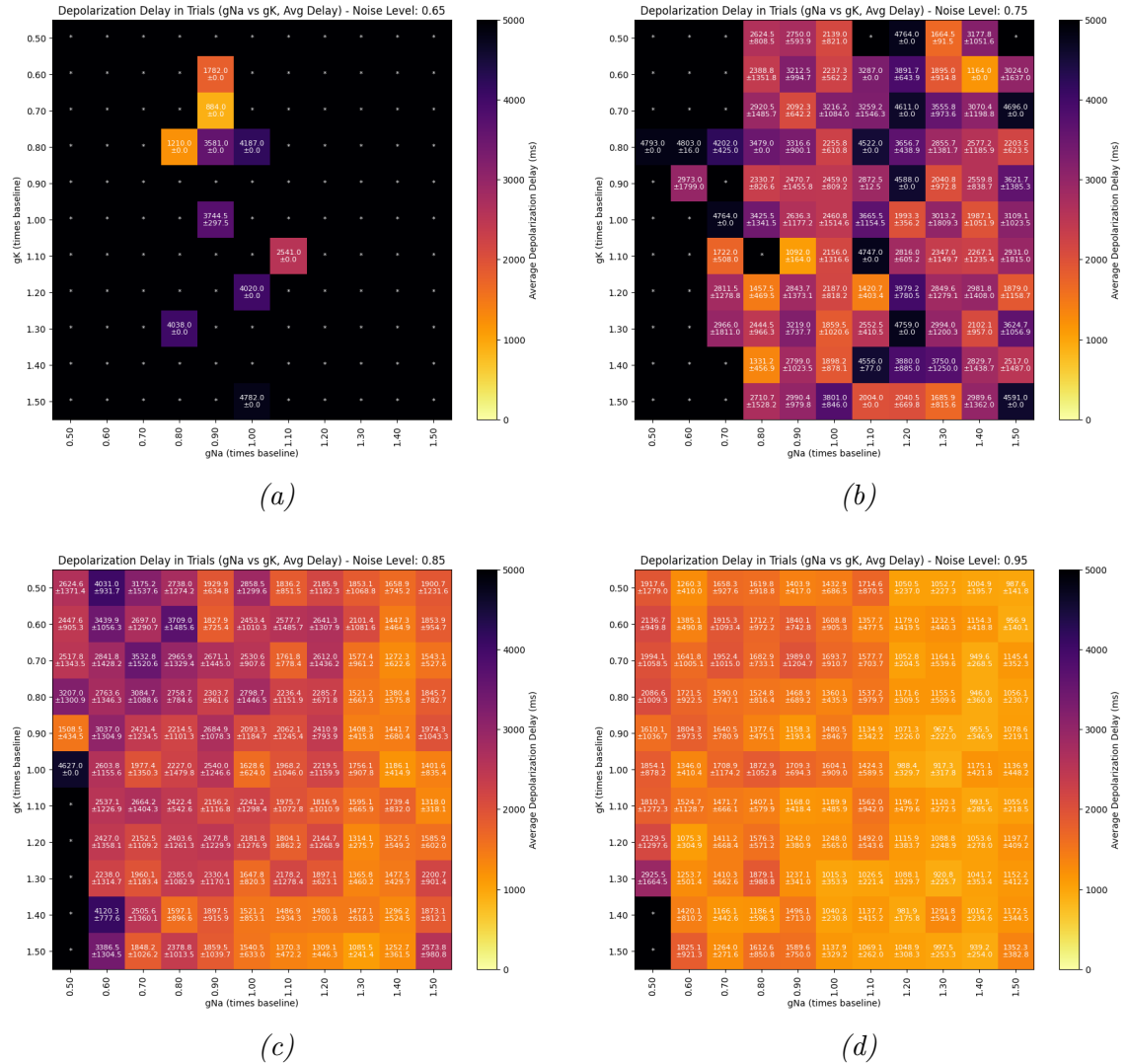


Figure 3.13: Average delay + Standard deviation of DPB in trials where depolarization block events occurred for all tested noise conditions. The x-axis shows all the sodium conductance changes in pyramidal cells, whereas the y-axis shows the potassium conductance changes in pyramidal cells. Modifications to pyramidal cells were applied to all compartments. The color intensity shows the average delay, where high-intensity red equals a shorter delay in DPB events in a condition. An asterisk (*) is an indication that no DPB events occurred in the condition and is colorless. The images are labeled from low noise (a through d), respectively.

3.5 Results of the External Noise: Burst analysis

In addition to the depolarization block (DPB) analysis, the population bursts of pyramidal and basket neurons were analyzed near the onset of a DPB event. Both peak height and general shape of the bursts were visualized in Figure 3.14. The 2nd to last before, last burst before and 1st burst after the DPB event were detected and analyzed. A range of sodium:potassium conductance changes in pyramidal cells were tested, namely: 1.00–1.00, 0.80–1.20, 1.20–0.80, and 1.20–1.20. The external noise was fixed at 20x times the baseline of the original model. Each burst has been aligned relative to the onset of the burst of the pyramidal population in the network (ms). The bursts were averaged over 15 trials, and the standard deviation of the spike activity was visualized as a filled gradient surrounding the curve.

3.5.1 Inter-ictal state

For the baseline condition, in the inter-ictal state the 2nd to last burst before the depolarization block was detected. The basket cell population burst occurred slightly before the pyramidal population burst with fairly low variance (3.14, a). In all other conditions the basket cell burst occurred at least 50 ms after the pyramidal population burst. The size of the basket cell burst only showed more variance in the 0.80–0.80 sodium:potassium condition (3.14, d), where the pyramidal burst also showed the most size variance.

3.5.2 Pre-ictal state

The pre-ictal network state shows the last burst before the depolarization block. From the Sanjay et al. (2015) article, large external drive from the pyramidal population blocks basket cell firing. Thus, the shift in basket cell burst timing is expected to be ahead of the pyramidal burst compared in the pre-ictal state. In the baseline condition the pyramidal burst peaks right after the basket cell burst (3.14, a). However, in all other conditions the basket cell burst shifts to further after the pyramidal burst, with the largest shift in the 1.20–1.20 sodium:potassium condition (3.14, e). Again, the variance if the basket cell burst was very small compared to the pyramidal population (which is also four times larger than the basket cell population)

3.5.3 Ictal state

The ictal network state shows the first burst after the depolarization block, which only contained pyramidal activity in all conditions. The shape of the pyramidal burst was fairly consistent across all conditions, in the 1.20–0.80 sodium:potassium condition the burst variance was slightly larger (3.14, c). In addition this particular pyramidal burst lost its secondary peak, which was present in all other conditions. All other conditions showed a secondary peak in the pyramidal burst, as the population spike activity became more desynchronized due to lack of somatic inhibition by the flat-lined basket cell activity (example of such population activity is visible in Figure 2.4). The variance in the burst intensity was most pronounced in the inter-ictal state, where the shape of the burst was least consistent. The height of

the pyramidal burst peak showed the most variance in the pre-ictal state with the highest variance in the 1.20–0.80 condition (3.14, C).

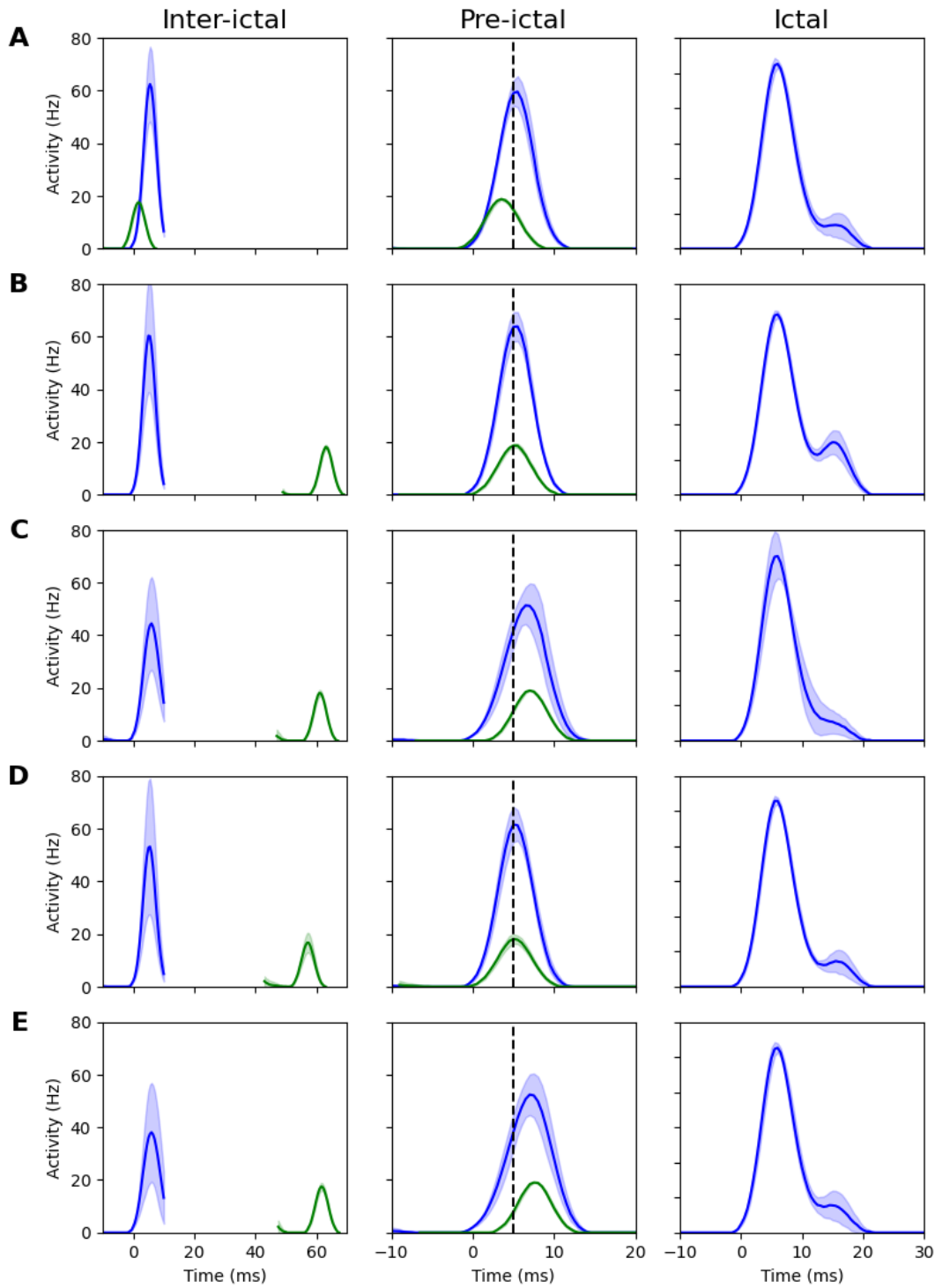


Figure 3.14: Analysis of burst detection before and after the onset of a depolarization block (DPB), showcasing the last two bursts before the DPB (Inter-ictal and Pre-ictal) and the first burst following it (Ictal). The figures (A-E) represent various sodium-potassium conductance ratios ($g_{\text{Na}}:g_{\text{K}}$). A: 1.00–1.00, B: 0.80–1.20, C: 1.20–0.80, D: 1.20–1.20, E: 0.80–0.80. Bursts are aligned by the onset of pyramidal population activity, highlighted by the standard deviation in spike activity (shaded area). A dashed line in the Pre-ictal plot marks a comparative reference for timing shifts in the basket cell population. All plots share normalized y-axes to facilitate cross-comparison. Pyramidal neurons are depicted in blue and basket cells in green.

3.6 Results of the Recurrent Connections variants

In this experiment, it was investigated if the network's susceptibility for depolarization block (DPB) events (ictal state) could be reduced by modifying the recurrent connection strength of basket cells. The effects of stronger recurrent connections of basket cells was tested in conditions of sodium:potassium conductance combinations of pyramidal cells (+- 25 % g_{Na} or g_{K}). Steps of 5 % increased recurrent connection strength were tested, ranging from 1.00 to 1.15 times the baseline connection strength (Figure 3.15).

At baseline, all conditions showed the maximum amount of DPB events in the network (Figure 3.15: a, 15 out of 15 trials or 100 %). Increasing the recurrent connection strength of basket cells by 5 % led to slight decrease in the amount of DPB events in the network in 4 out of the 9 tested conditions (Figure 3.15: b). At 10 % increased recurrent connection strength, the amount of DPB events decreased much strongly and some of the severe conditions only have DPB events in less than half of the trials (Figure 3.15: c). Lastly, at 15 % increased recurrent connection strength, the amount of DPB events decreased even further, with some conditions showing no DPB events at all (Figure 3.15: d).

More noise conditions are available for review in appendix C.

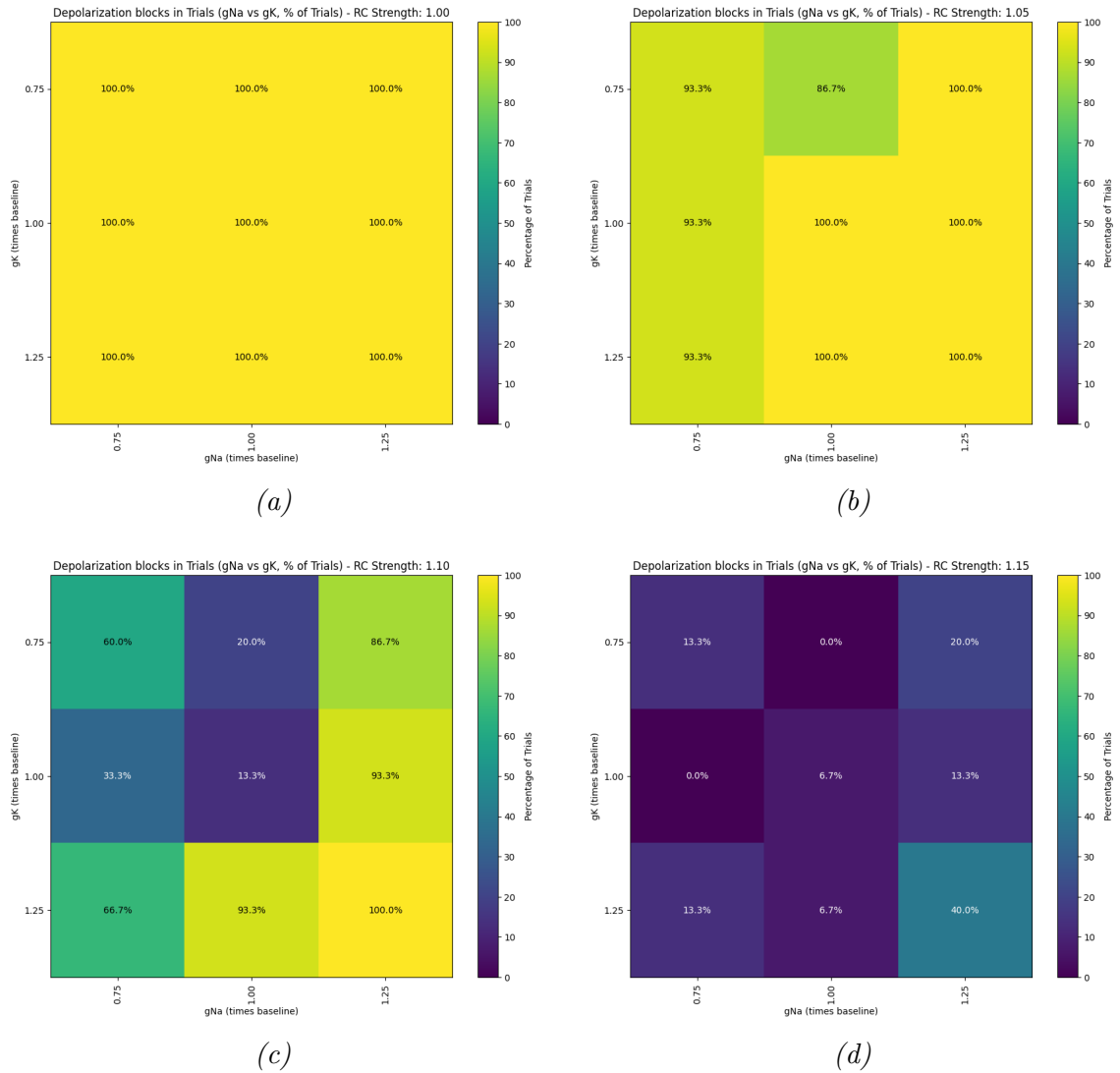


Figure 3.15: Percentage of trials where depolarization block events occurred for all tested noise conditions. The x-axis shows all the sodium conductance changes in pyramidal cells, whereas the y-axis shows the potassium conductance changes in pyramidal cells. Modifications to pyramidal cells were applied to all compartments. The color intensity shows the average delay, where high-intensity yellow equals higher percentage of DPB events in a condition. The images are labeled from low noise to higher noise (a through d), respectively.

4 Discussion

This study used a computer model of the CA3 subfield of the hippocampus originally developed by Neymotin et al. (2011). This model was used to study the effects of several different parameters that could initiate an epileptic state.

Initially, the implementation of the baseline model was verified to ensure that the model was functioning as expected. Similar metrics, to the ones tested in the adaptation by Sanjay et al. (2015) were used to verify the model. These metrics included population firing rates and theta-gamma oscillations (power and frequency). The experiments by Sanjay et al. (2015) explored the effects of impaired dendritic inhibition in the CA3 network as the main cause of epilepsy in the highly vulnerable brain region that is the CA3 subfield.

The results of our baseline model were consistent with the results of the Sanjay et al. (2015) study, which made it possible to proceed with variations and additional experiments using the same CA3 model in NEURON simulator.

First, the network dynamics due to dysfunctional voltage-gated ion channels for sodium and potassium were investigated in pyramidal, basket and O-LM cells populations within a CA3 hippocampal network. These variations of channel dynamics (conductance) were simulated to resemble epileptic genetic profiles which could be related TLE patients.

In addition to that, the networks susceptibility to external noise was tested by varying the noise level in the network with similar channel dynamics. Per trial of a condition, the amount of occurrences of depolarization blocks in the basket cell populations were counted and the average delay in the loss in basket cell activity was calculated.

Lastly, it was explored if the network could be rescued from an epileptic state by gradually increasing the strength of soma inhibition by basket cells by increasing the weight of recurrent connection within the basket cell population. Again, counting the amount of occurrences of depolarization blocks in the basket cell populations.

4.1 Model assumptions and Observations

In the original experiments Sanjay et al. (2015) the authors studied if impaired dendritic inhibition could lead to epileptic activity in the network. In their three experiment scenario's, they impaired the dendritic inhibition by O-LM cells on pyramidal cells (1), increased external noise to distal dendrites of pyramidal cells (2), and modified the connection strength of all cell types in the network (3). Their findings had no previous experimental validation and a linear relationship was assumed.

In this study, the experiments build upon the observations made by Sanjay et al. (2015) and further explored the network dynamics. Simulations were done separately, with step-wise modifications to parameters such as conductance or connection weight. This was necessary in order to be able to determine the extent in which these parameters could potentially lead to epileptic activity.

4.1.1 Sodium and Potassium variants

In the first experiment, sodium and potassium conductance parameters were modified in each cell type separately to identify which population had the most influence on firing activity of the other cell types and on the theta-gamma oscillations.

Pyramidal cells

In the case of pyramidal cells, modifications to sodium in O-LM cells had the most significant effect on their firing rate (figure 3.7, left). Similarly to directly reducing dendritic inhibition via modification of connection weight as in scenario 1 of the Sanjay et al. (2015), the pyramidal cells showed increased activity in their activity as (g_{Na}) for O-LM cells was reduced. This also increased the firing rates of the other two cell types, as they receive inputs from the pyramidal cells (figure 2.1). The large increase in basket cell firing rate directly influenced the gamma component of the LFP (figure 3.9), while O-LM reduced the theta component. These findings are consistent with the results of the Sanjay et al. (2015) study.

Out of all the cell types, pyramidal cells show the most linear relationship between the conductance of sodium and potassium channels and their firing rate. Potassium had an oppositely proportional effect on the firing rate of pyramidal cells compared to sodium. This result is somewhat unsurprising considering the role of potassium. In normal action potential dynamics, voltage-dependent sodium current rapidly depolarizes the membrane via voltage-gated ion channels. As a response, voltage-activated potassium channels are activated that hyperpolarize the membrane potential. This effect inactivates sodium channels as the membrane potential goes back to its polarized resting state, which in turn tunes down the firing frequency as observed.

Basket cells

In the basket cells a similar trend is visible, although the firing rate shift is much more pronounced for both modified ions. Again, this is a sensible result, considering the fast acting GABAergic inhibitory role as an interneuron (Wang & Buzsáki, 1996). In addition, basket cells contain extensive axonal arborization that allow them to form many connections with pyramidal cells and to other interneurons (Tukker et

al., 2013). Especially, their many connections to cells of their own type, might result in highly synchronized firing patterns that were observed in the population activity (figure 3.2). This effect is also expressed in the model, through the many-to-one connection design of the basket cells (Table B.11).

O-LM cells

O-LM cells had again somewhat linear, but relative small impact on the firing rates. Potentially, these effects are dependent on the morphology of the O-LM cells. O-LM cells primarily target the distal dendrites of pyramidal cells in the stratum lacunosum moleculare. This targeting influences their firing properties, as the distal dendritic locations typically receive inputs that are less intense or less frequent compared to the somatic or proximal dendritic inputs received by basket cells. Additionally, O-LM cells have less extensive local axonal arborizations compared to basket cells, which limits their range of influence and the synaptic inputs they receive (Saraga et al., 2003).

The primary role of O-LM cells is to modulate the input to the hippocampus from the entorhinal cortex, affecting the integration of cortical information (Leão et al., 2012). This modulation often requires precise, but less frequent, inhibition compared to the broad, fast inhibition exerted by basket cells on the pyramidal cell bodies. Therefore, their activity is more phasic or conditional, dependent on specific synaptic events that do not necessitate high-frequency firing.

Theta-gamma oscillations

Interestingly, theta remains relatively stable across all cell types, while gamma oscillations are more affected by the conductance modifications. Like in the original studies using the same model by Neymotin et al. (2011) and Sanjay et al. (2015), theta is resilient to changes in the network. This resilience is mostly due to the strong pacing which is provided to the interneurons by the MS. For sodium, while the theta component of the LFP appears to change a lot per condition, they are a factor 10 times smaller than does observed in the gamma component. With potassium modifications however, only the pyramidal cells seem to resemble a linear relationship with the theta power compared to the other cell types.

Potassium conductance influences the speed at which the membrane potential returns to its resting state. In the case of the the studied network, increased potassium conductance potentially causes faster repolarization of action potentials. This can shorten the duration of individual spikes and reduce the overall excitability of pyramidal cells, leading to a lower firing rate. However, this rapid repolarization can also allow neurons to return more quickly to a state where they can fire again, potentially aiding in synchronization (Mysin & Shubina, 2022). Alternatively, the quick recovery of neurons to their resting or near-threshold state can facilitate better phase-locking among neurons within the network (Leung & Law, 2020). This synchronization is crucial for enhancing the coherence and power of network oscillations like theta.

GABAergic interneurons, such as the basket and O-LM cells play a significant role in shaping the response of the network. As pyramidal cells fire less frequently or less synchronously due to increased potassium conductance, basket and O-LM

interneurons effectively increase their control over the timing of pyramidal cell output (Unal et al., 2018). This can help enforce a more regimented and synchronized firing pattern in line with the theta rhythm.

Gamma oscillations, on the other hand, are more sensitive to changes in the network. Especially in the case for O-LM modifications of at least -30 % (g_{Na}) (figure 3.9, bottom left). As the O-LM cells disinhibit the pyramidal cells, the basket cells receive more excitatory input which increases the gamma component of the LFP. The gamma power promptly returns to baseline levels when the O-LM cells are restored to their original conductance. Again showcasing, the high sensitivity of basket cells to changes in the network.

Classically it is thought that fast gamma oscillations are generated by the recurrent excitation between principle (pyramidal) neurons in generation of the theta-modulated gamma rhythm (Wang & Buzsáki, 1996). However, synchronization of basket cells and desynchronization of the other cell types in the more extreme experimental conditions suggests that the synaptic connection might be pivotal in the observed response (example of such effects in are seen in figures 3.2 and 3.3).

Early research has already shown that the type of synaptic input on AMPA type receptors can actually desynchronize, rather than synchronize a network of coupled neurons like in the model of this study (Khazipov et al., 1997; Van Vreeswijk et al., 1994). Thus, the oscillatory coherence in the network might be more dependent on rhythmic inhibition by fast-spiking interneurons like basket cells (Lytton & Sejnowski, 1991).

More modern investigations seem to support the idea that contrasting neurotransmitter release at the synapse, like glutamate/GABA or NMDA/AMPA co-transmission can regulate input-output dynamics in hippocampal circuits, rather than just membrane conductance dynamics (Ajibola et al., 2021; Micheli et al., 2021).

4.1.2 External noise variants

Throughout this experiment, O-LM-pyramidal connection strength was kept at 10 % of the baseline value. In the Sanjay et al. (2015) paper, the authors increased the noise through distal dendrites of pyramidal cells up to 15 times, where they noticed that the basket cell population entered a depolarization block. Similarly, in this study the presence of a depolarization block is the main factor that indicates the pathological state in the CA3 network. In this state the driving force is the increased pyramidal cell activity which lacks dendritic inhibition. In this situation, the LFP signal of the network showed an ictal-tonic pattern, as did the population (figure 2.3 and 3.11).

Percentage matrices

Comparing all the noise levels, it is readily apparent that in higher sodium conductance conditions, the network is much more excitable. As noise increases, elevated sodium rapidly induces an epileptic state 100 % of the time even though the jump in external noise goes from 16 to 17 times the baseline (0.80 and 0.85 noise levels, figure 3.12). Likewise, lower sodium levels are far less susceptible to hyperexcitability. At around -50 % (g_{Na}), the input from pyramidal cells is barely strong enough to induce a depolarization block even at 20 times baseline noise. In combination with

elevated potassium, the network showed the most severe susceptibility for epileptic activity. From the noise matrices it becomes apparent that the network is quite sensitive to small changes in noise level, where increments of 0.05 in noise levels induced significantly more depolarization blocks generally for each condition.

Delay matrices

The onset of the depolarization block changes with the noise level and the conductance of sodium and potassium. In the conditions with more DPBs, the average delay becomes significantly shorter and with less variance (figure 3.13). The original Sanjay et al. (2015) study states in the discussion that the shorter delay in the depolarization block that they perceived could be due to difference in synaptic plasticity that could include axonal or dendritic sprouting (scenario 3: effect of changes in connectivity at all synapses in the network). However, synapses (except the O-LM to pyr connection) were unchanged when measuring the delay of the DPB in this experiment. Yet, enhanced neural activity presented here showed similar results to that of a potentiated network that has been observed in other models with modified synaptic strength (Leite et al., 2005). Key is that the faster generation of epileptic activity, while sometimes result of long-term potentiation, usually occurs in various network circuitry throughout the brain (Cooke & Bliss, 2006).

Burst Analysis

A deeper investigation into the burst activity of the population was performed for basket and pyramidal cells. Considering that pyramidal activity is the apparent driving force behind the depolarization block, the exact reason of initiation was unclear. Therefore, a closer look at the burst timings and peak sizes reveals that beyond the baseline there are some consistent patterns (figure 3.14).

During the inter-ictal state the basket cells burst came before the pyramidal cells, whereas all other noise conditions did not show this burst pattern. In the pre-ictal state the basket cell burst seemed to shift in time, from before, to after the pyramidal cells burst. Thus, it is not always the case that the pyramidal input comes slightly before the basket cell burst, when the population might be in the refractory period and become locked in a depolarization block due to the constant excessive excitatory drive.

The ictal pyramidal activity did not show much variance from the baseline, in shape and in intensity. Throughout the trials the intensity of the population burst did not vary as is seen by the very small deviation, but the size of the generated noise also never did. This suggested that the network is quite sensitive to noise. Moreover, the amount of noise did not necessarily determine the characteristics of the bursts themselves.

Pyramidal cells are known to depend on the interaction between glutamatergic and GABAergic receptor activity, a powerful mechanism of intra-burst spike frequency modulation (Dzhala & Staley, 2003a). Although the basket cells do not fire at all after a DPB, the remaining O-LM influence (10 %) on pyramidal cells is perhaps enough to keep the pyramidal burst consistent.

The data suggests that the all-or-none bursting of pyramidal or basket cells is not necessarily dependent on precise timing. Rather, the ability for the population

to recover from strong synchronized input appeared to be an issue especially for basket cells.

This non-dependence on timing has been explored for the hippocampus by Menendez De La Prida et al. (2006), where they identified that populations actually go through three phases of firing periodically. These include: a recovery phase (from the previous burst), a plateau period of fluctuating activity, and a buildup where the firing rate accelerates just before the burst. These phases are also recognizable in the shown bursts of pyramidal and basket cells in figure 3.14.

However, it remains unclear if the timing of the proposed epileptic discharge (near the onset of a DPB) of pyramidal cells actually matters in the initiation of the depolarization block in basket cells. There are hints in the literature that sustained inter-ictal and ictal-like activity might even co-occur within the same network, provided the dysfunction of neural populations is beyond a certain excitability threshold (Dzhala & Staley, 2003b).

4.1.3 Recurrent connection strength variants

A further investigation in the depolarization block phenomenon was done in the last experiment. Here it was explored if increasing input among basket cells via increasingly stronger recurrent connection strength could overpower the massive external drive from the pyramidal cells and rescue the network from entering into the epileptic state. Similarly to the noise experiment, in enhanced excitatory conditions with high sodium and potassium conductance it was significantly less effective to reduce the amount of DPBs via enhanced recurrent inhibition.

The twenty times external input from the entorhinal cortex resembles heavy visual or auditory stimuli that possibly triggers epilepsy in a CA3 network. Nevertheless, the results show that even in the situation of disinhibition by O-LM cells (10 % connection strength), the network can be strengthened to almost completely avoid depolarization blocks in basket cells (figure 3.15). This could suggest that patients suffering from TLE could indeed be helped via anti-epileptic drugs (AEDs) such as benzodiazepines or barbiturates. Especially those that specifically stimulate GABAergic interneurons, such as basket cells that can dampen the firing of pyramidal cells of the hippocampus.

4.2 Implications of the findings

The results of this study highlight the critical role of ion channel dynamics, particularly sodium and potassium, in the generation of epileptic activity in the CA3 network. Modifications in these channels simulate conditions akin to those of specific genetic profiles that are associated with TLE. Furthermore, the network's response to small variations in elevated external noise levels in such conditions show that the CA3 subfield is indeed exceptionally excitable and susceptible to enter an epileptic state. In addition, the role of interneurons in network stability became apparent as even in a case of impaired dendritic inhibition by O-LM cells, epileptic networks can be rescued by influence of other interneurons like basket cells. Therefore, inducing such effects could be the focal point of medicinal intervention.

These results thus imply that manipulating interneuron activity, particularly through enhancing soma inhibition provides a theoretical bases for therapeutic

strategies. Simulating the various scenarios of this study and observing the outcomes, has shown that this computer model could serve as a predictive tool for understanding how certain genetic or environmental changes might precipitate epilepsy. This could be invaluable for developing personalized medicine approaches for TLE management.

The simulation's ability to reproduce and explore effects of synaptic plasticity via connection strength, offers a window into how long-term changes at synapses might contribute to epilepsy. This aligns with contemporary research suggesting that alterations in synaptic strength and plasticity play a significant role in the disease's progression.

More specifically, it has been shown that fast inhibitory transmission through GABAergic receptors seems to be mediated by receptor plasticity mechanisms such as trafficking, gene transcription, and post-translational modifications (Fritschy, 2008). In addition to neuronal ion regulation, these receptor mechanisms are crucial for maintaining the excitation and inhibition balance in TLE that can either suppress or promote seizures (Kaila et al., 2014). However, these aspects remain difficult to explore and implement in the current model and in NEURON due to the complexity of the underlying mechanisms.

4.3 Limitations of the research

As previously mentioned, there are many models available on ModelDB that explore the CA3 network in the hippocampus (<http://senselab.med.yale.edu/modeldb>).

The Neymotin et al. (2011) model adapted by Sanjay et al. (2015) in particular was chosen because of the relative high degree of complexity and the presence of homeostatic mechanisms, such as theta-modulated gamma oscillations as a baseline. The individual neuron types also contained many biophysical properties displayed in models and experiments of normal physiology. However, the model is still a simplification of the actual biological system and is lacking in terms of the full complexity of the CA3 network.

Also, the specific focus on the CA3 subfield and its particular cell types limits the generalizability of the findings to other regions of the hippocampus, even other subfields like CA1 or the dentate gyrus. Such that the unique properties and connections in the CA3 subfield do not reflect the broader dynamics involved in TLE. For instance, other cells such as astrocytes have also been implicated to possibly generate an excitation-inhibition imbalance through synaptic plasticity (Bonansco & Fuenzalida, 2016).

Moreover, the simulation's results are heavily dependent on the initial assumptions and parameters set by the original researchers. The linear-relationship that was assumed in terms of synaptic interactions may not hold under more realistic conditions. The simulations also have a limited scope in terms of the number of trials, which was a decision made based on the computational resources available. Yet, there are indications that due to random seeding (figure 3.1), more trials would possibly yield more consistent results.

Other earlier models have studied the influence of specific currents, conductances and synaptic connections in relationship with the generation of epileptic activity. Of which, CA3 has been investigated fewer times still, partially due to the heterogenous nature of this region.

Single cell conductance-based models such as the one designed by Cressman et al. (2009), have already shown that role of ion concentration dynamics even in reduced models are amenable. They are both qualitatively and quantitatively similar to full epilepsy network models such the one from this study. They also adhere to the Hodgkin-Huxley formalism which makes comparison between models easier.

Integrating aspects of single cell models with more parameters remains difficult however, as they increase the complexity of bifurcation analysis in neural networks. Meanwhile the identification ictal state transitions also becomes more difficult as the number of parameters increases.

4.4 Suggestions for future research

Like in the original model, only two main inhibitory mechanisms are integrated. Namely somatic and dendritic through basket and O-LM cells respectively. However, *in vivo*, the CA3 network contains many more interneuron types that could be included in the model.

A goal of this study was to explore if certain genetic profiles could be translated into model dynamics. Genotype-phenotype relationships are complex and often involve multiple genes and environmental factors (Steriade et al., 2020). Therefore, future endeavors could focus on incorporating data from sequenced genomes of TLE patients linked to channelopathies. This could provide a more accurate representation of the genetic basis of epilepsy and how it manifests in the CA3 network, provided there is data on how these mutations manifest in channel dynamics.

In addition, managing epilepsy is not only about preventing seizures, but also about improving the quality of life for patients. The key to that remains providing adequate medication with AEDs tailored to the individual form of epilepsy in the patient.

Therapeutic approaches aimed at reinstating the disrupted balance between excitatory and inhibitory processes hold significant potential for mitigating pathological brain activities. The integration of computational research with forthcoming experimental studies presents a robust avenue for enhancing our current understanding and formulating effective treatments for neurodegenerative diseases. This multi-disciplinary strategy is expected to yield substantial advancements in the field as technology and the capacity for realistic simulations improves.

Bibliography

- Ajibola, M. I., Wu, J.-W., Abdulmajeed, W. I., & Lien, C.-C. (2021). Hypothalamic Glutamate/GABA Cotransmission Modulates Hippocampal Circuits and Supports Long-Term Potentiation. *Journal of Neuroscience*, 41(39), 8181–8196. <https://doi.org/10.1523/JNEUROSCI.0410-21.2021>
- Aldenkamp, A. P., & Arends, J. (2004). Effects of epileptiform EEG discharges on cognitive function: Is the concept of “transient cognitive impairment” still valid? *Epilepsy & Behavior*, 5, 25–34. <https://doi.org/10.1016/j.yebeh.2003.11.005>
- Arski, O. N., Young, J. M., Smith, M.-L., & Ibrahim, G. M. (2021). The Oscillatory Basis of Working Memory Function and Dysfunction in Epilepsy. *Frontiers in Human Neuroscience*, 14. <https://doi.org/10.3389/fnhum.2020.612024>
- Bonansco, C., & Fuenzalida, M. (2016). Plasticity of Hippocampal Excitatory-Inhibitory Balance: Missing the Synaptic Control in the Epileptic Brain. *Neural Plasticity*, 2016, e8607038. <https://doi.org/10.1155/2016/8607038>
- Brunklaus, A., & Lal, D. (2020). Sodium channel epilepsies and neurodevelopmental disorders: From disease mechanisms to clinical application. *Developmental Medicine & Child Neurology*, 62(7), 784–792. <https://doi.org/10.1111/dmcn.14519>
- Cooke, S. F., & Bliss, T. V. P. (2006). Plasticity in the human central nervous system. *Brain*, 129(7), 1659–1673. <https://doi.org/10.1093/brain/awl082>
- Cressman, J. R., Ullah, G., Ziburkus, J., Schiff, S. J., & Barreto, E. (2009). The influence of sodium and potassium dynamics on excitability, seizures, and the stability of persistent states: I. Single neuron dynamics. *Journal of computational neuroscience*, 26(2), 159–170. <https://doi.org/10.1007/s10827-008-0132-4>
- Dzhala, V. I., & Staley, K. J. (2003a). Excitatory Actions of Endogenously Released GABA Contribute to Initiation of Ictal Epileptiform Activity in the Developing Hippocampus. *Journal of Neuroscience*, 23(5), 1840–1846. <https://doi.org/10.1523/JNEUROSCI.23-05-01840.2003>
- Dzhala, V. I., & Staley, K. J. (2003b). Transition from Interictal to Ictal Activity in Limbic Networks In Vitro. *Journal of Neuroscience*, 23(21), 7873–7880. <https://doi.org/10.1523/JNEUROSCI.23-21-07873.2003>
- Eunson, L. H., Rea, R., Zuberi, S. M., Youroukos, S., Panayiotopoulos, C. P., Liguori, R., Avoni, P., McWilliam, R. C., Stephenson, J. B. P., Hanna, M. G., Kullmann, D. M., & Spauschus, A. (2000). Clinical, genetic, and expression studies of mutations in the potassium channel gene KCNA1 reveal new phenotypic variability. *Annals of Neurology*, 48(4), 647–656. [https://doi.org/10.1002/1531-8249\(200010\)48:4<647::AID-ANA12>3.0.CO;2-Q](https://doi.org/10.1002/1531-8249(200010)48:4<647::AID-ANA12>3.0.CO;2-Q)

- Fisher, R. S., Acevedo, C., Arzimanoglou, A., Bogacz, A., Cross, J. H., Elger, C. E., Engel Jr, J., Forsgren, L., French, J. A., Glynn, M., Hesdorffer, D. C., Lee, B., Mathern, G. W., Moshé, S. L., Perucca, E., Scheffer, I. E., Tomson, T., Watanabe, M., & Wiebe, S. (2014). ILAE Official Report: A practical clinical definition of epilepsy. *Epilepsia*, 55(4), 475–482. <https://doi.org/10.1111/epi.12550>
- Fritschy, J.-M. (2008). Epilepsy, E/I balance and GABA_A receptor plasticity. *Frontiers in Molecular Neuroscience*, 1. <https://doi.org/10.3389/neuro.02.005.2008>
- Gao, K., Lin, Z., Wen, S., & Jiang, Y. (2022). Potassium channels and epilepsy. *Acta Neurologica Scandinavica*, 146(6), 699–707. <https://doi.org/10.1111/ane.13695>
- Hakami, T. (2021). Efficacy and tolerability of antiseizure drugs. *Therapeutic Advances in Neurological Disorders*, 14, 17562864211037430. <https://doi.org/10.1177/17562864211037430>
- Hodgkin, A. L., Huxley, A. F., & Katz, B. (1952). Measurement of current-voltage relations in the membrane of the giant axon of Loligo. *The Journal of Physiology*, 116(4), 424–448. Retrieved April 11, 2024, from <https://www.ncbi.nlm.nih.gov/pmc/articles/PMC1392219/>
- Hwang, S.-K., & Hirose, S. (2012). Genetics of temporal lobe epilepsy. *Brain and Development*, 34(8), 609–616. <https://doi.org/10.1016/j.braindev.2011.10.008>
- Isomoto, S., Kondo, C., & Kurachi, Y. (1997). Inwardly Rectifying Potassium Channels: Their Molecular Heterogeneity and Function. *The Japanese Journal of Physiology*, 47(1), 11–39. <https://doi.org/10.2170/jjphysiol.47.11>
- Kaila, K., Ruusuvuori, E., Seja, P., Voipio, J., & Puskarjov, M. (2014). GABA actions and ionic plasticity in epilepsy. *Current Opinion in Neurobiology*, 26, 34–41. <https://doi.org/10.1016/j.conb.2013.11.004>
- Kalitzin, S., Petkov, G., Suffczynski, P., Grigorovsky, V., Bardakjian, B. L., Lopes Da Silva, F., & Carlen, P. L. (2019). Epilepsy as a manifestation of a multistate network of oscillatory systems. *Neurobiology of Disease*, 130, 104488. <https://doi.org/10.1016/j.nbd.2019.104488>
- Khazipov, R., Leinekugel, X., Khalilov, I., Gaiarsa, J. L., & Ben-Ari, Y. (1997). Synchronization of GABAergic interneuronal network in CA3 subfield of neonatal rat hippocampal slices. *The Journal of Physiology*, 498(3), 763–772. <https://doi.org/10.1113/jphysiol.1997.sp021900>
- Leão, R. N., Mikulovic, S., Leão, K. E., Munguba, H., Gezelius, H., Enjin, A., Patra, K., Eriksson, A., Loew, L. M., Tort, A. B. L., & Kullander, K. (2012). OLM interneurons differentially modulate CA3 and entorhinal inputs to hippocampal CA1 neurons. *Nature Neuroscience*, 15(11), 1524–1530. <https://doi.org/10.1038/nn.3235>
- Leite, J. P., Neder, L., Arisi, G. M., Carlotti Jr., C. G., Assirati, J. A., & Moreira, J. E. (2005). Plasticity, Synaptic Strength, and Epilepsy: What Can We Learn from Ultrastructural Data? *Epilepsia*, 46(s5), 134–141. <https://doi.org/10.1111/j.1528-1167.2005.01021.x>
- Leung, L. S., & Law, C. S. H. (2020). Phasic modulation of hippocampal synaptic plasticity by theta rhythm. *Behavioral Neuroscience*, 134(6), 595–612. <https://doi.org/10.1037/bne0000354>

- Liu, Y., Duan, Y., Du, D., & Chen, F. (2020). Rescuing Kv10.2 protein changes cognitive and emotional function in kainic acid-induced status epilepticus rats. *Epilepsy & Behavior*, 106, 106894. <https://doi.org/10.1016/j.yebeh.2019.106894>
- Lüders, H. O., Najm, I., Nair, D., Widdess-Walsh, P., & Bingman, W. (2006). The epileptogenic zone: General principles. *Epileptic Disorders: International Epilepsy Journal with Videotape*, 8 Suppl 2, S1–9.
- Lytton, W. W., & Sejnowski, T. J. (1991). Simulations of cortical pyramidal neurons synchronized by inhibitory interneurons. *Journal of Neurophysiology*, 66(3), 1059–1079. <https://doi.org/10.1152/jn.1991.66.3.1059>
- Lytton, W. W., Orman, R., & Stewart, M. (2005). Computer simulation of epilepsy: Implications for seizure spread and behavioral dysfunction. *Epilepsy & Behavior*, 7(3), 336–344. <https://doi.org/10.1016/j.yebeh.2005.06.011>
- Meadows, L. S., Malhotra, J., Loukas, A., Thyagarajan, V., Kazen-Gillespie, K. A., Koopman, M. C., Kriegler, S., Isom, L. L., & Ragsdale, D. S. (2002). Functional and Biochemical Analysis of a Sodium Channel β 1 Subunit Mutation Responsible for Generalized Epilepsy with Febrile Seizures Plus Type 1. *Journal of Neuroscience*, 22(24), 10699–10709. <https://doi.org/10.1523/JNEUROSCI.22-24-10699.2002>
- Menendez De La Prida, L., Huberfeld, G., Cohen, I., & Miles, R. (2006). Threshold Behavior in the Initiation of Hippocampal Population Bursts. *Neuron*, 49(1), 131–142. <https://doi.org/10.1016/j.neuron.2005.10.034>
- Micheli, P., Ribeiro, R., & Giorgetti, A. (2021). A Mechanistic Model of NMDA and AMPA Receptor-Mediated Synaptic Transmission in Individual Hippocampal CA3-CA1 Synapses: A Computational Multiscale Approach. *International Journal of Molecular Sciences*, 22(4), 1536. <https://doi.org/10.3390/ijms22041536>
- Migliore, M., Cannia, C., Lytton, W. W., Markram, H., & Hines, M. L. (2006). Parallel network simulations with NEURON. *Journal of Computational Neuroscience*, 21(2), 119–129. <https://doi.org/10.1007/s10827-006-7949-5>
- Migliore, M., Messineo, L., & Ferrante, M. (2004). Dendritic IhSelectively Blocks Temporal Summation of Un同步ized Distal Inputs in CA1 Pyramidal Neurons. *Journal of Computational Neuroscience*, 16(1), 5–13. <https://doi.org/10.1023/B:JCNS.0000004837.81595.b0>
- Mysin, I., & Shubina, L. (2022). From mechanisms to functions: The role of theta and gamma coherence in the intrahippocampal circuits. *Hippocampus*, 32(5), 342–358. <https://doi.org/10.1002/hipo.23410>
- Neymotin, S. A., Lazarewicz, M. T., Sherif, M., Contreras, D., Finkel, L. H., & Lytton, W. W. (2011). Ketamine Disrupts Theta Modulation of Gamma in a Computer Model of Hippocampus. *Journal of Neuroscience*, 31(32), 11733–11743. <https://doi.org/10.1523/JNEUROSCI.0501-11.2011>
- Nikitin, E. S., & Vinogradova, L. V. (2021). Potassium channels as prominent targets and tools for the treatment of epilepsy. *Expert Opinion on Therapeutic Targets*, 25(3), 223–235. <https://doi.org/10.1080/14728222.2021.1908263>
- Nyhus, E., & Curran, T. (2010). Functional role of gamma and theta oscillations in episodic memory. *Neuroscience & Biobehavioral Reviews*, 34(7), 1023–1035. <https://doi.org/10.1016/j.neubiorev.2009.12.014>

- Oyrer, J., Maljevic, S., Scheffer, I. E., Berkovic, S. F., Petrou, S., & Reid, C. A. (2018). Ion Channels in Genetic Epilepsy: From Genes and Mechanisms to Disease-Targeted Therapies (P. M. Sexton, Ed.). *Pharmacological Reviews*, 70(1), 142–173. <https://doi.org/10.1124/pr.117.014456>
- Sanjay, M., Neymotin, S. A., & Krothapalli, S. B. (2015). Impaired dendritic inhibition leads to epileptic activity in a computer model of CA3. *Hippocampus*, 25(11), 1336–1350. <https://doi.org/10.1002/hipo.22440>
- Saraga, F., Wu, C. P., Zhang, L., & Skinner, F. K. (2003). Active dendrites and spike propagation in multicompartment models of oriens-lacunosum/moleculare hippocampal interneurons. *The Journal of Physiology*, 552(3), 673–689. <https://doi.org/10.1113/jphysiol.2003.046177>
- Scheffer, I. E., Harkin, L. A., Grinton, B. E., Dibbens, L. M., Turner, S. J., Zielinski, M. A., Xu, R., Jackson, G., Adams, J., Connellan, M., Petrou, S., Wellard, R. M., Briellmann, R. S., Wallace, R. H., Mulley, J. C., & Berkovic, S. F. (2006). Temporal lobe epilepsy and GEFS+ phenotypes associated with SCN1B mutations. *Brain*, 130(1), 100–109. <https://doi.org/10.1093/brain/awl272>
- Steriade, C., French, J., & Devinsky, O. (2020). Epilepsy: Key experimental therapeutics in early clinical development. *Expert Opinion on Investigational Drugs*, 29(4), 373–383. <https://doi.org/10.1080/13543784.2020.1743678>
- Stokes, J., Kyle, C., & Ekstrom, A. D. (2015). Complementary Roles of Human Hippocampal Subfields in Differentiation and Integration of Spatial Context. *Journal of Cognitive Neuroscience*, 27(3), 546–559. https://doi.org/10.1162/jocn_a_00736
- Striano, P., & Minassian, B. A. (2020). From Genetic Testing to Precision Medicine in Epilepsy. *Neurotherapeutics*, 17(2), 609–615. <https://doi.org/10.1007/s13311-020-00835-4>
- Tukker, J. J., Lasztóczki, B., Katona, L., Roberts, J. D. B., Pissadaki, E. K., Dalezios, Y., Márton, L., Zhang, L., Klausberger, T., & Somogyi, P. (2013). Distinct Dendritic Arborization and In Vivo Firing Patterns of Parvalbumin-Expressing Basket Cells in the Hippocampal Area CA3. *Journal of Neuroscience*, 33(16), 6809–6825. <https://doi.org/10.1523/JNEUROSCI.5052-12.2013>
- Unal, G., Crump, M. G., Viney, T. J., Éltes, T., Katona, L., Klausberger, T., & Somogyi, P. (2018). Spatio-temporal specialization of GABAergic septo-hippocampal neurons for rhythmic network activity. *Brain Structure and Function*, 223(5), 2409–2432. <https://doi.org/10.1007/s00429-018-1626-0>
- Van Vreeswijk, C., Abbott, L. F., & Bard Ermentrout, G. (1994). When inhibition not excitation synchronizes neural firing. *Journal of Computational Neuroscience*, 1(4), 313–321. <https://doi.org/10.1007/BF00961879>
- Wallace, R. H., Wang, D. W., Singh, R., Scheffer, I. E., George, A. L., Phillips, H. A., Saar, K., Reis, A., Johnson, E. W., Sutherland, G. R., Berkovic, S. F., & Mulley, J. C. (1998). Febrile seizures and generalized epilepsy associated with a mutation in the Na⁺-channel ss1 subunit geneSCN1B. *Nature Genetics*, 19(4), 366–370. <https://doi.org/10.1038/1252>
- Wang, X.-J., & Buzsáki, G. (1996). Gamma Oscillation by Synaptic Inhibition in a Hippocampal Interneuronal Network Model. *The Journal of Neuroscience*, 16(20), 6402–6413. <https://doi.org/10.1523/JNEUROSCI.16-20-06402.1996>

- Wengert, E. R., & Patel, M. K. (2021). The Role of the Persistent Sodium Current in Epilepsy. *Epilepsy Currents*, 21(1), 40–47. <https://doi.org/10.1177/1535759720973978>
- Witter, M. P. (2007). Intrinsic and extrinsic wiring of CA3: Indications for connectional heterogeneity. *Learning & Memory*, 14(11), 705–713. <https://doi.org/10.1101/lm.725207>
- Yayik, A., Yildirim, E., Kutlu, Y., & Yildirim, S. (2015). Epileptic State Detection: Pre-ictal, Inter-ictal, Ictal. *International Journal of Intelligent Systems and Applications in Engineering*, 3(1), 14–18. <https://doi.org/10.18201/ijisae.14531>
- Yu, F. H., Mantegazza, M., Westenbroek, R. E., Robbins, C. A., Kalume, F., Burton, K. A., Spain, W. J., McKnight, G. S., Scheuer, T., & Catterall, W. A. (2006). Reduced sodium current in GABAergic interneurons in a mouse model of severe myoclonic epilepsy in infancy. *Nature Neuroscience*, 9(9), 1142–1149. <https://doi.org/10.1038/nn1754>
- Zhang, L.-m., Chen, L., Zhao, Y.-f., Duan, W.-m., Zhong, L.-m., & Liu, M.-w. (2023). Identification of key potassium channel genes of temporal lobe epilepsy by bioinformatics analyses and experimental verification. *Frontiers in Neurology*, 14. <https://doi.org/10.3389/fneur.2023.1175007>

A Appendix

A.1 Cellular dynamics: equations and parameters

The mathematical formulations of the cell types below are based on the work of Sanjay et al. (2015) and have been implemented as published in their model release on GitHub in the relevant NEURON mod files.

Basket cells: The transient sodium current was described by

$$I_{Na,I} = g_{Na,I} m_\infty^3 h (V_I - E_{Na,I}),$$

where

$$m_\infty = \frac{\alpha_m}{\alpha_m + \beta_m},$$

and

$$\alpha_m(V_I) = -0.1 \frac{(V_I + 35)}{e^{-0.1(V_I+35)} - 1}, \quad \beta_m(V_I) = 4e^{-\frac{(V_I+60)}{18}}.$$

The inactivation variable h obeyed the first-order kinetics:

$$\frac{dh}{dt} = \phi(\alpha_h(1 - h) - \beta_h h),$$

where

$$\alpha_h(V_I) = 0.07e^{-\frac{(V_I+58)}{20}}, \quad \beta_h(V_I) = \frac{1}{e^{-0.1(V_I+28)} + 1}.$$

The delayed rectifier potassium current was described by

$$I_{K,I} = g_{K,I} n^4 (V_I - E_{K,I}),$$

where the activation variable n obeyed the following equation:

$$\frac{dn}{dt} = \phi(\alpha_n(1 - n) - \beta_n n),$$

with

$$\alpha_n(V_I) = -0.01 \frac{(V_I + 34)}{e^{-0.1(V_I+34)} - 1}, \quad \beta_n(V_I) = 0.125e^{-\frac{(V_I+44)}{80}}.$$

For the experiments, the following parameters were used: $g_{Na,I} = 35 \text{ mS/cm}^2$, $g_{K,I} = 9 \text{ mS/cm}^2$, $E_{Na,I} = 55 \text{ mV}$, $E_{K,I} = -90 \text{ mV}$, $\phi = 5$.

O-LM cells: The channel currents were described by

$$I_{Na,o} = g_{Na,o} m^3 h (V_O - E_{Na,O}),$$

where m obeyed

$$\frac{dm}{dt} = \alpha_m(1-m) - \beta_m m,$$

with

$$\alpha_m = \frac{-0.1(V_O + 38)}{e^{\frac{-(V_O + 38)}{10}} - 1}, \quad \beta_m = 4e^{-\frac{(V_O + 65)}{18}},$$

and h obeyed

$$\frac{dh}{dt} = \alpha_h(1-h) - \beta_h h,$$

with

$$\alpha_n(V_O) = 0.07e^{\frac{-(V_O + 63)}{20}}, \quad \beta_n(V_O) = \frac{1}{1 + e^{\frac{-0.1(V_O + 33)}{10}}},$$

Similarly,

$$I_{K,O} = g_{K,O} n^4 (V_O - E_{K,O}),$$

$$\frac{dn}{dt} = \alpha_n(1-n) - \beta_n n,$$

$$\alpha_n(V_O) = \frac{0.018(V_O - 25)}{1 - e^{-\frac{V_O - 25}{25}}}, \quad \beta_n(V_O) = \frac{0.0036(V_O - 35)}{e^{\frac{V_O - 35}{12}} - 1}$$

$$I_{h,O} = g_{h,O} r (V_O - E_{h,O}),$$

$$\frac{dr}{dt} = \frac{r_\infty - r}{\tau_r},$$

$$r_\infty(V_O) = \frac{1}{1 + e^{-\frac{V_O + 84}{10.2}}}, \quad \tau_r(V_O) = \frac{1}{e^{-14.59 - 0.086V_O} + e^{-1.87 + 0.0701V_O}};$$

$$I_{A,O} = g_{A,O} ab (V_O - E_{A,O}),$$

$$\frac{da}{dt} = \frac{\alpha_\infty - a}{\tau_a},$$

$$\alpha_\infty(V_O) = \frac{1}{1 + e^{\frac{-(V_O + 14)}{16.6}}}, \quad \tau_a(V_O) = 5,$$

$$\frac{db}{dt} = \frac{b_\infty - b}{\tau_b},$$

$$b_\infty(V_O) = \frac{1}{1 + e^{\frac{V_O + 71}{7.3}}}, \quad \tau_b(V_O) = \frac{1}{\frac{0.000009}{e^{\frac{V_O - 26}{18.5}}} + \frac{0.014}{0.2 + e^{\frac{-(V_O + 70)}{11}}}}.$$

For the experiments, the following parameters were used: $g_{Na,o} = 30 \text{ mS/cm}^2$, $g_{K,O} = 23 \text{ mS/cm}^2$, $g_{h,O} = 12 \text{ mS/cm}^2$, $g_{A,O} = 16 \text{ mS/cm}^2$, $E_{Na,O} = 90 \text{ mV}$, $E_{K,O} = -100 \text{ mV}$, $E_{h,O} = -32.9 \text{ mV}$, $E_{A,O} = -90 \text{ mV}$.

Pyramidal cells: I_{conn,E_k} was the current due to electrical coupling between compartments, which was given by

$$I_{\text{conn},E,k} = g_{k,j+1}(V_{E,j+1} - V_{E,j}) + g_{k,j}(V_{E,j-1} - V_{E,j})$$

with the coupling conductance given by

$$g_{k,j} = \frac{r_k r_j^2}{R_a L_k (L_k r_j^2 + L_j r_k^2)}$$

where L_k and r_k was the length and radius of the compartment k respectively (note the need of units conversion in order to get $g_{k,j}$ in mS/cm²). The ionic currents were given by:

$$\begin{aligned} I_{Na,E_k} &= g_{Na,E_k} m^3 h i (V_{E_k} - E_{Na,E}), \\ I_{K,E_k} &= g_{K,E_k} n^4 (V_0 - E_{K,E}), \\ I_{h,E_k} &= g_{h,E_k} r (V_{E_k} - E_{h,E}), \\ I_{A,E_k} &= g_{A,E_k} ab (V_{E_k} - E_{A,E}), \end{aligned}$$

and the gating variables obeyed equations of the form

$$\frac{dx}{dt} = \frac{x_\infty - x}{\tau_x},$$

where $x = m, h, i, n, r, a, b$ and

$$m_\infty = \frac{\alpha_m}{\alpha_m + \beta_m}, \quad \tau_m = \max \left(0.2, \frac{0.5}{\alpha_m + \beta_m} \right),$$

$$\begin{aligned} \alpha_m(V_{E_k}) &= \frac{0.4(V_{E_k} + 30)}{1 - e^{-\frac{V_{E_k} + 30}{7.2}}}, & \beta_m(V_{E_k}) &= \frac{0.124(V_{E_k} + 30)}{e^{\frac{V_{E_k} + 30}{7.2}} - 1}, \\ h_\infty(V_{E_k}) &= \frac{1}{1 + e^{\frac{V_{E_k} + 50}{4}}}, & \tau_h &= \max \left(0.5, \frac{0.5}{\alpha_h + \beta_h} \right), \\ \alpha_h(V_{E_k}) &= \frac{0.03(V_{E_k} + 45)}{1 - e^{-\frac{V_{E_k} + 45}{1.5}}}, & \beta_h(V_{E_k}) &= \frac{0.01(V_{E_k} + 45)}{e^{\frac{V_{E_k} + 45}{1.5}} - 1}, \\ i_\infty(V_{E_k}) &= \frac{1 + b_k e^{\frac{V_{E_k} + 60}{2}}}{1 + e^{\frac{V_{E_k} + 60}{2}}}, & \tau_i &= \max \left(10, \frac{30000 \beta_i}{1 + \alpha_i} \right), \\ \alpha_i(V_{E_k}) &= e^{0.45(V_{E_k} + 66)}, & \beta_i(V_{E_k}) &= e^{0.09(V_{E_k} + 66)}, \\ n_\infty &= \frac{1}{1 + \alpha_n}, & \tau_n &= \max \left(2, \frac{50 \beta_n}{1 + \alpha_n} \right), \\ \alpha_n(V_{E_k}) &= e^{-0.11(V_{E_k} - 13)}, & \beta_n(V_{E_k}) &= e^{-0.08(V_{E_k} - 13)}, \end{aligned}$$

$$\begin{aligned}
r_{\infty,\text{HCN}2}(V_{E_k}) &= \frac{1}{1 + e^{\frac{V_{E_k} - V_{50k}}{10.5}}}, & \tau_{r,\text{HCN}2}(V_{E_k}) &= \frac{1}{e^{-14.59 - 0.086V_{E_k}} + e^{-1.87 + 0.0701V_{E_k}}}, \\
r_{\infty,\text{HCN}1}(V_{E_k}) &= \frac{1}{1 + e^{0.151(V_{E_k} - V_{50k})}}, & \tau_{r,\text{HCN}1}(V_{E_k}) &= \frac{e^{0.033(V_{E_k} + 75)}}{0.011(1 + e^{0.0833(V_{E_k} + 75)})}, \\
a_{\infty} &= \frac{1}{1 + \alpha_a}, & \tau_a &= \max\left(0.1, \frac{c_k \beta_a}{1 + \alpha_a}\right), \\
\alpha_a(V_{E_k}) &= e^{-0.038\left(d_k + \frac{1}{1 + \frac{e^{V_{E_k}} + 40}{e^{E_k} + 5}}\right)(V_{E_k} - e_k)}, & \beta_a(V_{E_k}) &= e^{-0.038\left(f_k + \frac{1}{1 + \frac{e^{V_{E_k}} + 40}{e^{E_k} + 5}}\right)(V_{E_k} - e_k)}, \\
b_{\infty}(V_{E_k}) &= \frac{1}{1 + e^{0.11(V_{E_k} + 56)}}, & \tau_b(V_{E_k}) &= \max(2, 0.26(V_{E_k} + 50)).
\end{aligned}$$

For the experiments, the following parameters were used: $E_{Na,E_k} = 55$ mV, $E_{K,E_k} = -90$ mV, $E_{h,E_k} = -30$ mV, $E_{A,E_k} = -90$ mV. The ionic conductances values (in mS/cm²) and values of other parameters dependent on the compartment are shown in the additional table section below.

B Appendix

B.1 Additional tables

B.1.1 Sodium-Potassium variants numerical results.

Table B.1: Overview of results for the network with modified sodium conductance in pyramidal cells.

Pyr (Hz) + Std	BWB (Hz) + Std	OLM (Hz) + Std	Theta Freq (Hz)	Theta power (mV ² Hz ⁻¹)	Gamma Freq (Hz)	Gamma power (mV ² Hz ⁻¹)	Modified Celltype	Condition
1.33 ± 0.59	8.33 ± 1.98	0.69 ± 0.32	6.2	1.35	31.5	1.03	Pyr	0.5
1.47 ± 0.60	9.16 ± 1.97	0.79 ± 0.35	6.2	1.58	31.3	1.40	Pyr	0.6
1.59 ± 0.61	9.88 ± 2.08	0.87 ± 0.35	6.2	1.68	31.8	1.54	Pyr	0.7
1.69 ± 0.62	9.99 ± 2.19	0.94 ± 0.35	6.2	1.70	32.4	1.56	Pyr	0.8
1.77 ± 0.63	9.74 ± 2.16	1.00 ± 0.36	6.2	1.71	34.1	1.33	Pyr	0.9
1.87 ± 0.60	9.13 ± 2.26	1.06 ± 0.36	6.2	1.63	35.7	0.89	Pyr	1.0
2.00 ± 0.59	8.98 ± 2.32	1.14 ± 0.36	6.2	1.45	41.2	0.47	Pyr	1.1
2.11 ± 0.62	9.08 ± 2.56	1.23 ± 0.37	6.2	1.37	44.8	0.33	Pyr	1.2
2.17 ± 0.65	9.29 ± 2.67	1.29 ± 0.38	6.4	1.26	47.0	0.28	Pyr	1.3
2.21 ± 0.65	9.42 ± 2.67	1.37 ± 0.38	6.2	1.25	49.1	0.27	Pyr	1.4
2.25 ± 0.67	9.60 ± 2.69	1.41 ± 0.39	6.3	1.16	47.7	0.25	Pyr	1.5

Table B.2: Overview of results for the network with modified sodium conductance in basket cells.

Pyr (Hz) + Std	BWB (Hz) + Std	OLM (Hz) + Std	Theta Freq (Hz)	Theta power (mV ² Hz ⁻¹)	Gamma Freq (Hz)	Gamma power (mV ² Hz ⁻¹)	Modified Celltype	Condition
2.80 ± 0.65	0.00 ± 0.00	3.07 ± 0.43	7.8	0.40	34.2	0.04	Bwb	0.5
2.78 ± 0.65	0.02 ± 0.06	3.03 ± 0.44	7.8	0.41	33.9	0.04	Bwb	0.6
2.27 ± 0.69	3.54 ± 0.87	1.46 ± 0.40	6.4	1.08	46.9	0.16	Bwb	0.7
1.96 ± 0.62	7.37 ± 2.19	1.13 ± 0.36	6.2	1.19	45.0	0.24	Bwb	0.8
1.89 ± 0.60	8.39 ± 2.38	1.09 ± 0.36	6.2	1.49	38.8	0.54	Bwb	0.9
1.87 ± 0.60	9.07 ± 2.32	1.06 ± 0.36	6.2	1.51	37.0	0.80	Bwb	1.0
1.85 ± 0.60	9.57 ± 2.24	1.05 ± 0.36	6.2	1.62	35.8	0.97	Bwb	1.1
1.84 ± 0.59	9.61 ± 2.20	1.06 ± 0.36	6.2	1.63	36.5	1.00	Bwb	1.2
1.83 ± 0.60	9.79 ± 2.22	1.04 ± 0.36	6.2	1.67	37.0	1.07	Bwb	1.3
1.83 ± 0.60	10.08 ± 2.26	1.03 ± 0.36	6.2	1.67	35.1	1.14	Bwb	1.4
1.82 ± 0.59	10.30 ± 2.17	1.04 ± 0.35	6.2	1.80	36.2	1.22	Bwb	1.5

Table B.3: Overview of results for the network with modified sodium conductance in OLM cells.

Pyr (Hz) + Std	BWB (Hz) + Std	OLM (Hz) + Std	Theta Freq (Hz)	Theta power (mV ² Hz ⁻¹)	Gamma Freq (Hz)	Gamma power (mV ² Hz ⁻¹)	Modified Celltype	Condition
3.79 ± 1.00	18.76 ± 3.77	0.01 ± 0.03	4.0	0.02	37.8	1.82	OLM	0.5
3.22 ± 0.89	21.74 ± 2.41	0.23 ± 0.21	6.2	0.59	32.3	4.29	OLM	0.6
2.79 ± 0.80	18.51 ± 2.38	0.42 ± 0.26	6.2	1.17	32.8	3.61	OLM	0.7
2.45 ± 0.72	14.57 ± 2.40	0.62 ± 0.31	6.2	1.46	33.9	2.40	OLM	0.8
2.14 ± 0.67	11.20 ± 2.41	0.84 ± 0.34	6.2	1.63	34.9	1.31	OLM	0.9
1.87 ± 0.61	9.15 ± 2.26	1.06 ± 0.36	6.2	1.59	35.5	0.89	OLM	1.0
1.61 ± 0.55	7.49 ± 2.03	1.31 ± 0.38	6.2	1.48	37.7	0.59	OLM	1.1
1.36 ± 0.50	6.29 ± 1.84	1.60 ± 0.39	6.2	1.31	36.3	0.41	OLM	1.2
1.11 ± 0.45	4.98 ± 1.61	1.98 ± 0.39	6.2	1.11	35.6	0.27	OLM	1.3
0.90 ± 0.40	4.01 ± 1.38	2.49 ± 0.37	6.2	0.99	34.3	0.21	OLM	1.4
0.75 ± 0.36	3.31 ± 1.20	3.02 ± 0.35	6.2	0.88	36.7	0.17	OLM	1.5

Table B.4: Overview of results for the network with modified potassium conductance in pyramidal cells.

Pyr (Hz) + Std	BWB (Hz) + Std	OLM (Hz) + Std	Theta Freq (Hz)	Theta power (mV ² Hz ⁻¹)	Gamma Freq (Hz)	Gamma power (mV ² Hz ⁻¹)	Modified Celltype	Condition
2.15 ± 0.64	10.75 ± 2.43	1.32 ± 0.37	6.3	1.19	35.9	1.32	Pyr	0.5
2.05 ± 0.63	10.04 ± 2.34	1.25 ± 0.37	6.2	1.28	36.6	1.17	Pyr	0.6
1.97 ± 0.63	9.74 ± 2.33	1.14 ± 0.37	6.2	1.34	35.1	1.13	Pyr	0.7
1.93 ± 0.62	9.32 ± 2.48	1.11 ± 0.37	6.2	1.42	37.0	0.87	Pyr	0.8
1.90 ± 0.62	9.31 ± 2.29	1.08 ± 0.37	6.2	1.50	37.0	0.90	Pyr	0.9
1.86 ± 0.59	9.03 ± 2.24	1.07 ± 0.36	6.2	1.59	36.6	0.85	Pyr	1.0
1.83 ± 0.59	8.83 ± 2.26	1.05 ± 0.36	6.2	1.57	36.3	0.74	Pyr	1.1
1.79 ± 0.58	8.63 ± 2.17	1.03 ± 0.35	6.2	1.66	35.9	0.68	Pyr	1.2
1.75 ± 0.56	8.36 ± 2.16	1.02 ± 0.35	6.2	1.72	35.5	0.65	Pyr	1.3
1.72 ± 0.56	8.18 ± 2.04	1.00 ± 0.35	6.2	1.77	36.9	0.59	Pyr	1.4
1.68 ± 0.54	7.99 ± 2.08	0.99 ± 0.35	6.2	1.85	36.4	0.56	Pyr	1.5

Table B.5: Overview of results for the network with modified potassium conductance in basket cells.

Pyr (Hz) + Std	BWB (Hz) + Std	OLM (Hz) + Std	Theta Freq (Hz)	Theta power (mV ² Hz ⁻¹)	Gamma Freq (Hz)	Gamma power (mV ² Hz ⁻¹)	Modified Celltype	Condition
1.85 ± 0.58	9.19 ± 2.77	1.06 ± 0.36	6.2	1.45	36.6	0.54	Bwb	0.5
1.86 ± 0.59	9.11 ± 2.77	1.06 ± 0.36	6.2	1.53	37.0	0.63	Bwb	0.6
1.86 ± 0.60	9.12 ± 2.45	1.06 ± 0.36	6.2	1.58	36.8	0.73	Bwb	0.7
1.86 ± 0.60	9.06 ± 2.33	1.07 ± 0.36	6.2	1.49	36.6	0.78	Bwb	0.8
1.86 ± 0.60	8.94 ± 2.28	1.06 ± 0.36	6.2	1.51	36.7	0.79	Bwb	0.9
1.86 ± 0.60	9.07 ± 2.30	1.07 ± 0.36	6.2	1.57	36.0	0.88	Bwb	1.0
1.87 ± 0.60	9.07 ± 2.22	1.07 ± 0.36	6.2	1.59	36.2	0.87	Bwb	1.1
1.87 ± 0.61	9.03 ± 2.30	1.07 ± 0.38	6.2	1.62	35.7	0.87	Bwb	1.2
1.88 ± 0.61	8.93 ± 2.27	1.06 ± 0.36	6.2	1.52	36.9	0.80	Bwb	1.3
1.88 ± 0.61	8.86 ± 2.18	1.07 ± 0.36	6.2	1.51	37.0	0.82	Bwb	1.4
1.87 ± 0.61	8.71 ± 2.17	1.09 ± 0.36	6.2	1.53	37.7	0.74	Bwb	1.5

Table B.6: Overview of results for the network with modified potassium conductance in OLM cells.

Pyr (Hz) + Std	BWB (Hz) + Std	OLM (Hz) + Std	Theta Freq (Hz)	Theta power (mV ² Hz ⁻¹)	Gamma Freq (Hz)	Gamma power (mV ² Hz ⁻¹)	Modified Celltype	Condition
1.70 ± 0.57	8.01 ± 2.16	1.23 ± 0.36	6.2	1.54	38.8	0.64	OLM	0.5
1.73 ± 0.58	8.21 ± 2.13	1.19 ± 0.36	6.2	1.51	36.6	0.66	OLM	0.6
1.76 ± 0.58	8.34 ± 2.32	1.17 ± 0.37	6.2	1.52	37.4	0.70	OLM	0.7
1.79 ± 0.58	8.58 ± 2.17	1.14 ± 0.36	6.2	1.58	37.2	0.77	OLM	0.8
1.83 ± 0.59	8.81 ± 2.26	1.10 ± 0.36	6.2	1.53	35.9	0.79	OLM	0.9
1.87 ± 0.60	9.20 ± 2.26	1.07 ± 0.36	6.2	1.60	36.3	0.84	OLM	1.0
1.90 ± 0.61	9.40 ± 2.28	1.03 ± 0.36	6.2	1.56	36.1	0.90	OLM	1.1
1.94 ± 0.61	9.58 ± 2.30	1.00 ± 0.35	6.2	1.55	35.9	0.95	OLM	1.2
1.98 ± 0.63	9.99 ± 2.44	0.96 ± 0.36	6.2	1.54	36.1	1.06	OLM	1.3
2.02 ± 0.63	10.27 ± 2.30	0.93 ± 0.35	6.2	1.59	35.1	1.18	OLM	1.4
2.06 ± 0.65	10.66 ± 2.39	0.89 ± 0.35	6.2	1.52	35.4	1.22	OLM	1.5

B.1.2 Compartment dependent parameters

Table B.7: Compartment dependent parameters used in the formulations of the three neuronal cell types. See A for the full equations. The ionic conductances are in mS/cm².

	g_h	g_A	g_{Na}	g_K	V_{50}	b	c	d	e	f
Bdend	0.1	48	32	10	-82	1	4	1.5	11	0.825
Soma	0.1	48	32	10	-82	0.8	4	1.5	11	0.825
Adend1	0.2	72	32	10	-82	0.5	4	1.5	11	0.825
Adend2	0.4	120	32	10	-90	0.5	2	1.8	-1	0.7
Adend3	0.7	200	32	10	-90	0.5	2	1.8	-1	0.7

Table B.8: Synaptic Parameters for the Connectivity Between Neurons in the Model: Pre- and postsynaptic receptor types are given for each cell type. The time constants τ_1 and τ_2 are in milliseconds. τ_1 is the rise time constant, the time it takes for synaptic conductance to increase from baseline to peak. τ_2 is the decay time constant, the time it takes for the conductance to decrease from peak to baseline. The conductance indicates the strength of the synaptic connection and its ability to conduct ionic current across the postsynaptic membrane. This influences the extent to which the synaptic input can depolarize the postsynaptic neuron and is in nanoSiemens (nS).

Presynaptic	Postsynaptic	Receptor	τ_1 (ms)	τ_2 (ms)	Conductance (nS)
Pyramidal	Pyramidal	AMPA	0.05	5.3	0.02
Pyramidal	Pyramidal	NMDA	15	150	0.004
Pyramidal	Basket	AMPA	0.05	5.3	0.36
Pyramidal	Basket	NMDA	15	150	1.38
Pyramidal	OLM	AMPA	0.05	5.3	0.36
Pyramidal	OLM	NMDA	15	150	0.72
Basket	Pyramidal	GABA-A	0.07	9.1	0.72
Basket	Basket	GABA-A	0.07	9.1	4.5
Basket	OLM	GABA-A	0.07	9.1	0.0288
OLM	Pyramidal	GABA-A	0.2	20	72
MS	Basket	GABA-A	20	40	1.6
MS	OLM	GABA-A	20	40	1.6

B.1.3 Connections

Note: For all tables the weight values are given in microsiemens (μS). The weight is converted by taking into account that $1\text{e-}3$ is equivalent to $1 \mu\text{S}$.

Table B.9: Pyramidal to Basket Weave Basket and OLM NMDA Synaptic Connections. This table summarizes the count and scaled synaptic weights for NMDA receptor-mediated connections originating from pyramidal neurons. The “Scale” variable allows modulation of the connection strength in various experimental conditions. Each connection specifies the number of synapses (‘Count’) and the effective synaptic weight (‘Weight’) after scaling, targeting NMDA receptors at specific postsynaptic sites.

Connection	Count	Weight (μS)	Synapse
Pyr to Bwb NMDA	100	scale $\times 1.38$	somaNMDA
Pyr to OLM NMDA	10	scale $\times 0.7$	somaNMDA
Pyr to Pyr NMDA	25	scale $\times 0.004$	BdendNMDA

Table B.10: Pyramidal to Basket Weave Basket and OLM AMPA Synaptic Connections. Detailed here are the AMPA receptor-mediated synaptic connections from pyramidal neurons. The “Scale” factor is applied to the base synaptic weight to explore its effect on network dynamics. The “Count” column reflects the number of synaptic contacts, while the “Weight” column indicates the scaled weight, directed towards AMPA receptors at the soma or dendritic compartments.

Connection	Count	Weight (μS)	Synapse
Pyr to Bwb AMPA	100	scale \times 0.36	somaAMPAf
Pyr to OLM AMPA	10	scale \times 0.36	somaAMPAf
Pyr to Pyr AMPA	25	scale \times 0.02	BdendAMPA

Table B.11: Basket Cell GABAergic Synaptic Connections. This table provides information on the GABA receptor-mediated synaptic connections between basket weave basket cells and other neuronal types. The “Scale” factor adjusts the base synaptic weight for experimental analysis. The “Count” indicates how many synaptic connections are made, and the “Weight” reflects the scaled synaptic efficacy, impacting inhibitory GABAergic transmission.

Connection	Count	Weight (μS)	Synapse
Bwb to Bwb GABA	60	scale \times 4.5	somaGABAf
Bwb to Pyr GABA	50	scale \times 0.72	somaGABAf
Bwb to OLM GABA	17	scale \times 0.036	somaGABAf

Table B.12: OLM to Pyramidal GABAergic Synaptic Connections. Presented here are the details of GABA receptor-mediated inhibitory connections from OLM cells to pyramidal neurons. The `olm_to_pyr_weight` variable represents a specific scaling factor for these connections, potentially derived from experimental data. The “Count” column denotes the number of connections, and the “Weight” column shows the scaled synaptic strength affecting GABAergic signaling at distal dendritic sites.

Connection	Count	Weight (μS)	Synapse
OLM to Pyr GABA	20	<code>olm_to_pyr_weight</code> \times 72	Adend2GABAs
OLM to Pyr GABA 2	10	<code>olm_to_pyr_weight</code> \times 1.44	Adend2GABAs

B.1.4 NetStim parameters

Note: For all tables the weight values are given in microsiemens (μS). The weight is converted by taking into account that $1e-3$ is equivalent to $1 \mu\text{S}$.

Table B.13: NetStim Parameters Summary for Pyramidal Cells. The “Number” of spikes for each stimulus is calculated using the formula $(1e3/\text{Interval}) \cdot h.tstop$ where $h.tstop$ is 5000 ms, adjusting based on the specified interval for each stimulus. The `pyr_noise_scale` is used in the *external noise variants* experiment. This results in a target number of spikes over the simulation period.

Stimulus	Interval (ms)	Noise	Weight (μS)	Target
Pyr 1	1	1	0.05	somaAMPAf
Pyr 2	1	1	$0.05 \cdot \text{pyr_noise_scale}$	Adend3AMPAf
Pyr 3	1	1	0.012	somaGABAf
Pyr 4	1	1	0.012	Adend3GABAf
Pyr 5	100	1	$6.5 \cdot \text{pyr_noise_scale}$	Adend3NMDA

Table B.14: Noise to OLM NetStim Parameters Summary. The “Number” of spikes for each stimulus is calculated using the formula $(1e3/\text{Interval}) \cdot h.tstop$, with $h.tstop$ representing the simulation stop time in ms, adjusted based on the specified interval for each stimulus. Different seeds are used for each stimulus instance.

Stimulus	Interval (ms)	Noise	Weight (μS)	Target
OLM 1	1	1	0.0625	somaAMPAf
OLM 2	1	1	0.2	somaGABAf

Table B.15: Noise to BWB NetStim Parameters Summary. The “Number” of spikes for each stimulus is calculated using the formula $(1e3/\text{Interval}) \cdot h.tstop$, where $h.tstop$ is the simulation stop time in ms. Each stimulus is adjusted based on the specified interval. Different seeds are used for each stimulus instance to introduce variability.

Stimulus	Interval (ms)	Noise	Weight (μS)	Target
Bwb 1	1	1	0.02	somaAMPAf
Bwb 2	1	1	0.2	somaGABAf

Table B.16: Noise from MS to BWB & OLM NetStim Parameters Summary. The “Number” of spikes for each stimulus is calculated using the formula $(1e3/\text{Interval}) \cdot h.tstop$, with $h.tstop$ representing the simulation stop time in ms. The specified interval for each stimulus defines the rate at which the NetStim will deliver spikes, with a non-random (noise=0) spike generation.

Stimulus	Interval (ms)	Noise	Weight (μS)	Target
OLM MS	150	0	1.6	somaGABA _{ss}
Bwb MS	150	0	1.6	somaGABA _{ss}

C Appendix

C.1 Additional data

Additional data, including the raw data and the code used to generate the figures in this thesis, can be obtained on request from Synaptica B.V. See copyright statement for contact details.

C.2 Additional figures

Additional figures for the results of the noise and recurrent connection variants are shown in the following pages. Representative figures are shown in the results section.

C.2.1 External Noise variants: DPB percentage matrices

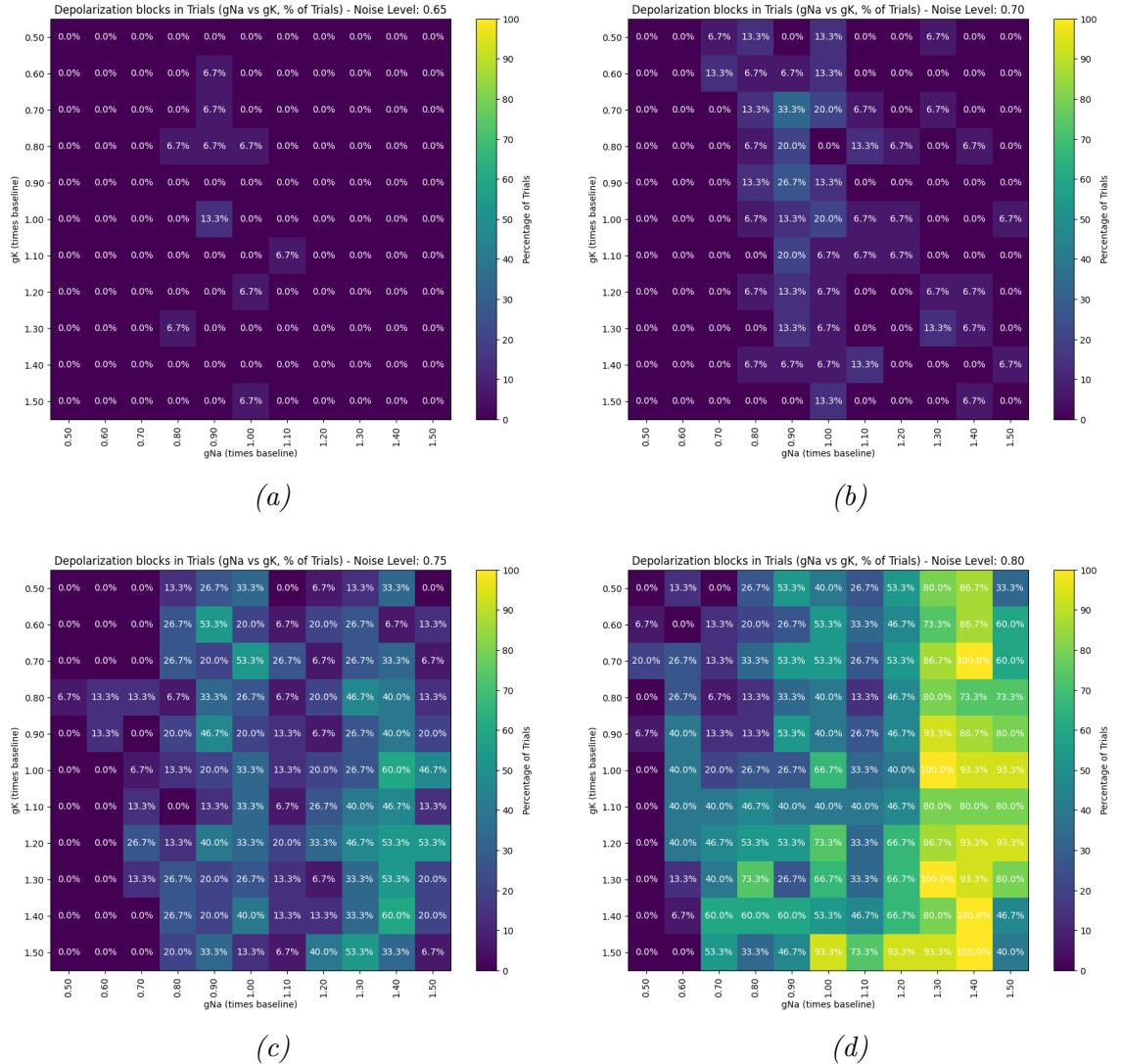
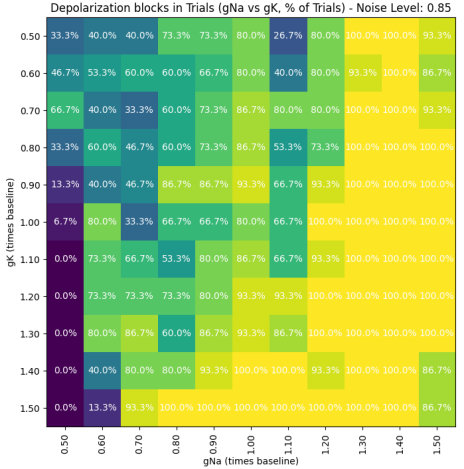
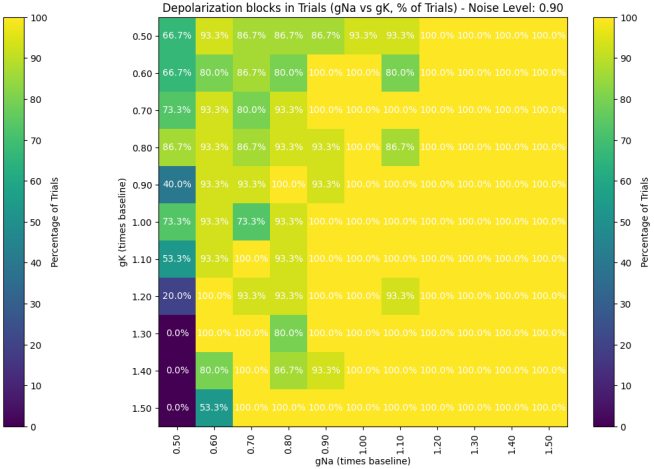


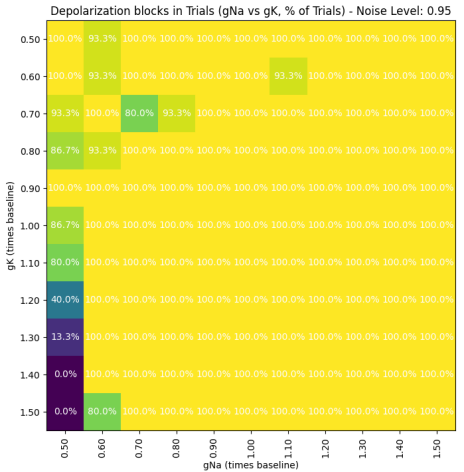
Figure C.1: Percentage of trials where depolarization block events occurred for all tested noise conditions. The x-axis shows all the sodium conductance changes in pyramidal cells, whereas the y-axis shows the potassium conductance changes in pyramidal cells. Modifications to pyramidal cells were applied to all compartments. The color intensity scales from 0 to 100 %, where high-intensity yellow equals a higher amount of DPB events in a condition. The images are labeled from low noise to higher noise (a through k), respectively.



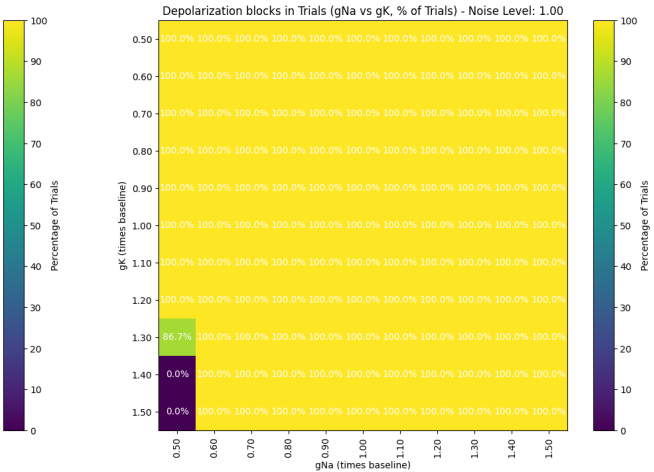
(e)



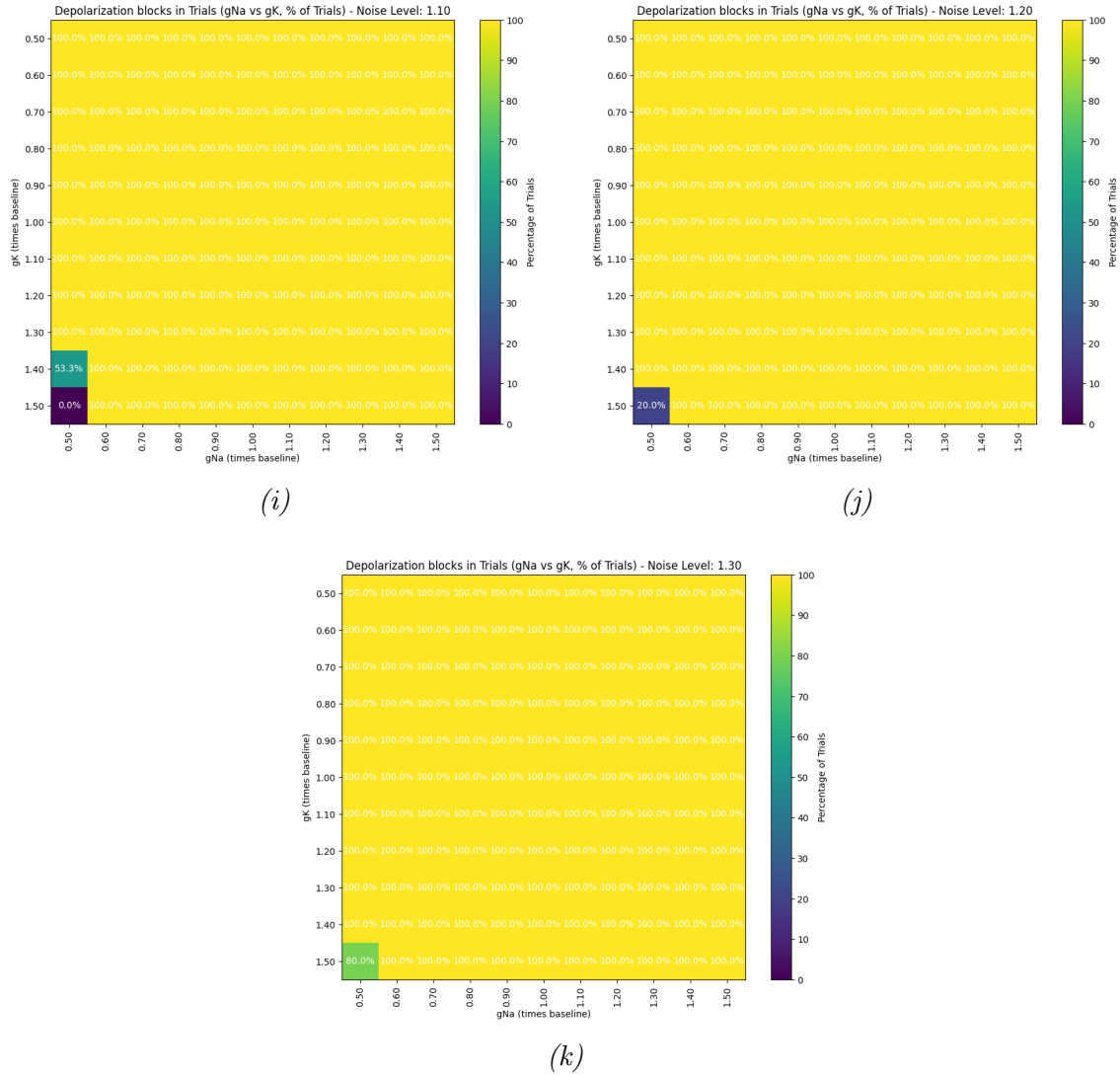
(f)



(g)



(h)



C.2.2 External Noise variants: DPB delay matrices

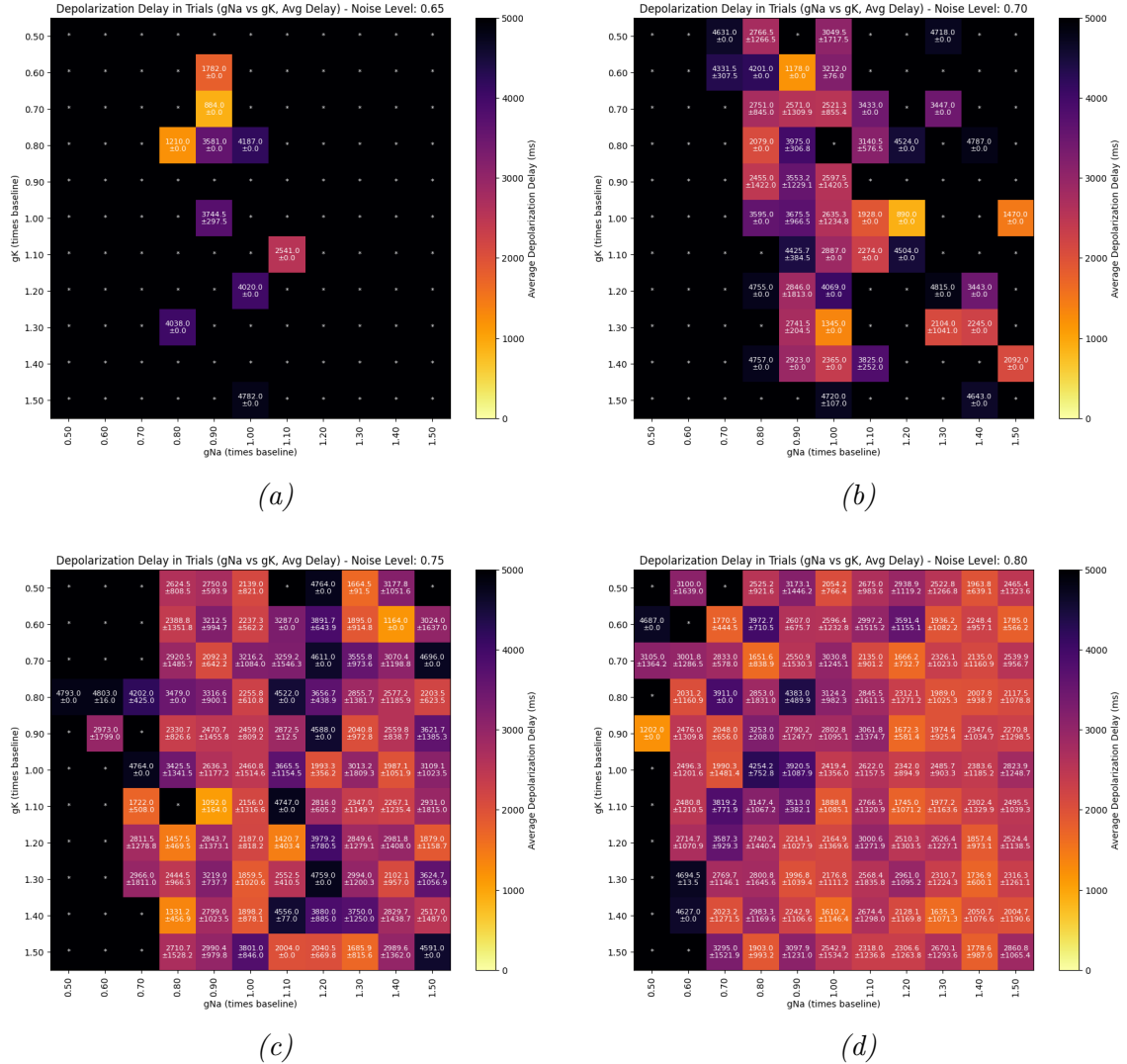
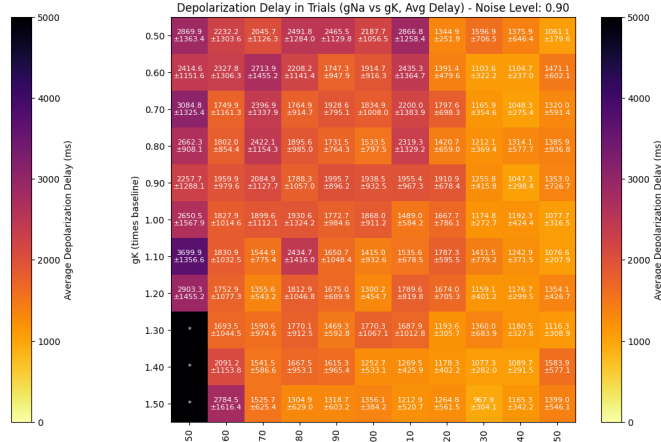


Figure C.2: Average delay + Standard deviation of DPB in trials where depolarization block events occurred for all tested noise conditions. The x-axis shows all the sodium conductance changes in pyramidal cells, whereas the y-axis shows the potassium conductance changes in pyramidal cells. Modifications to pyramidal cells were applied to all compartments. The color intensity shows the average delay, where high-intensity red equals a shorter delay in DPB events in a condition. An asterisk (*) is an indication that no DPB events occurred in the condition and is colorless. The images are labeled from low noise to higher noise (a through k), respectively.

Depolarization Delay in Trials (gNa vs gK, Avg Delay) - Noise Level: 0.85



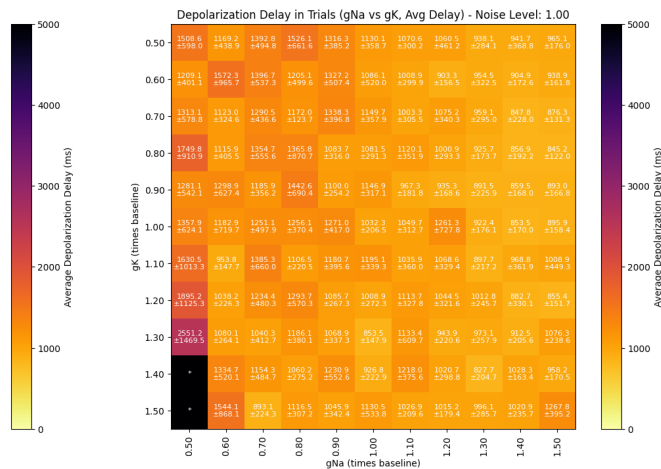
(e)

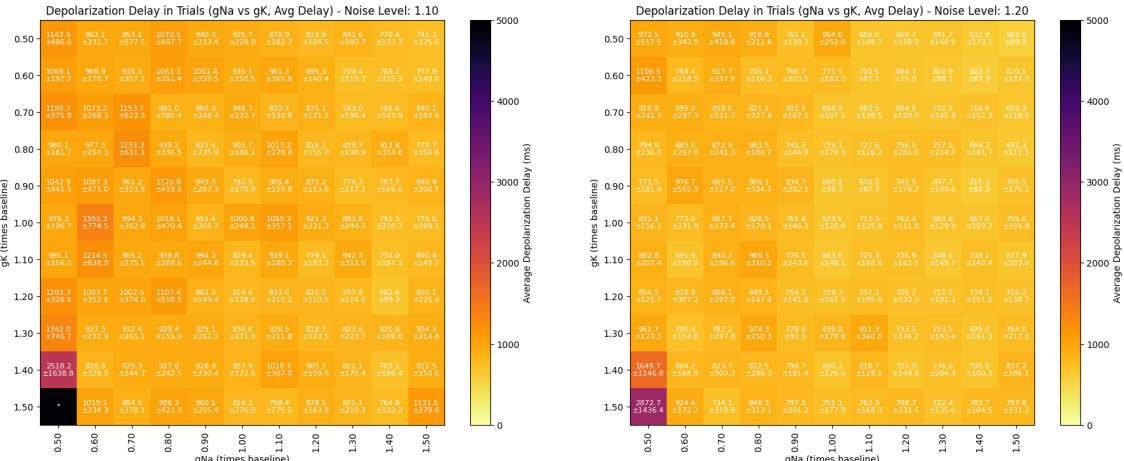


(f)



(g)

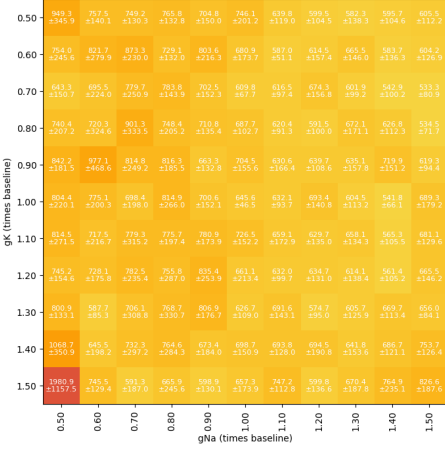




(i)

(j)

Depolarization Delay in Trials (gNa vs gK, Avg Delay) - Noise Level: 1.20



(k)

C.2.3 Recurrent connection matrices

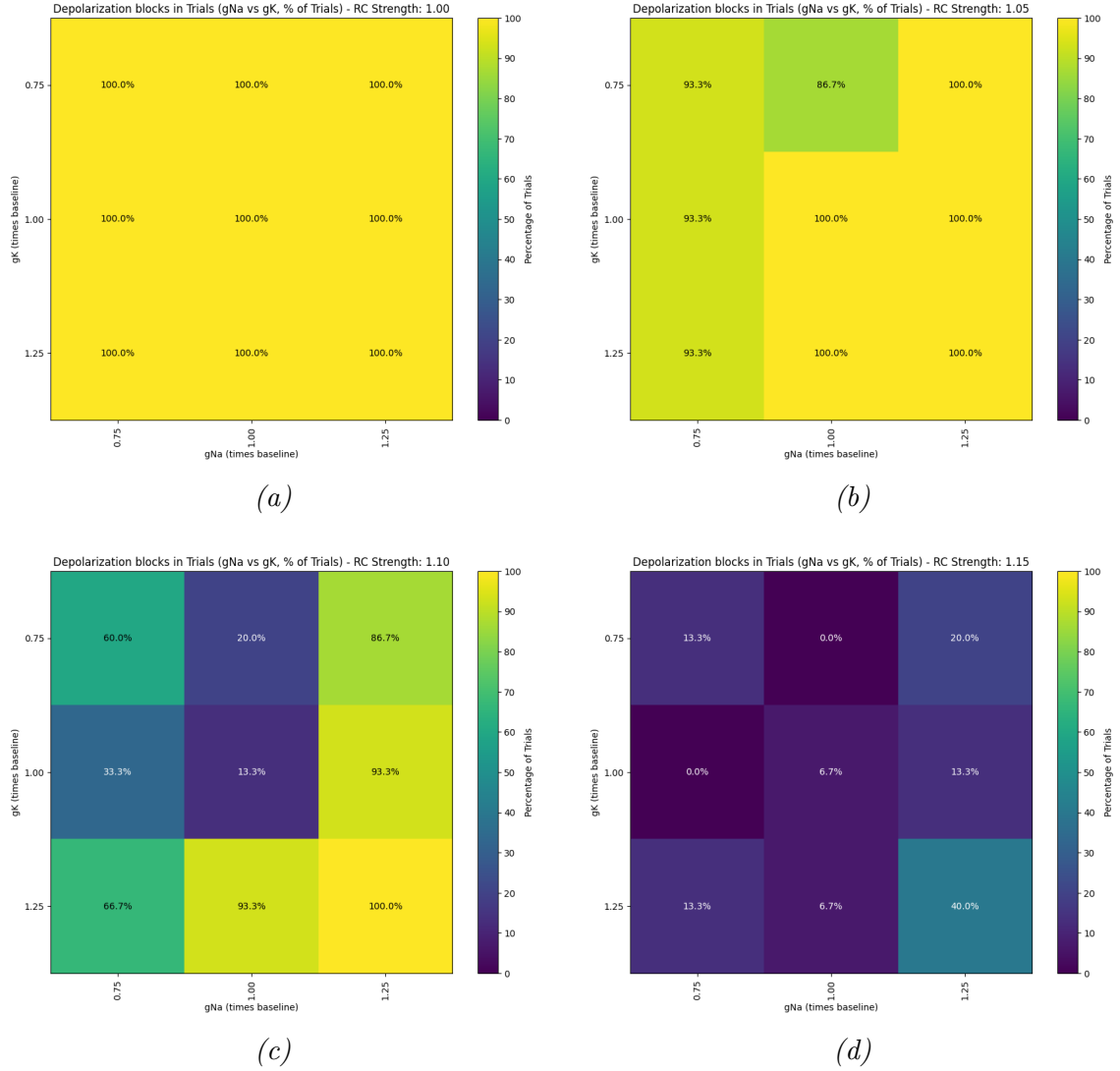
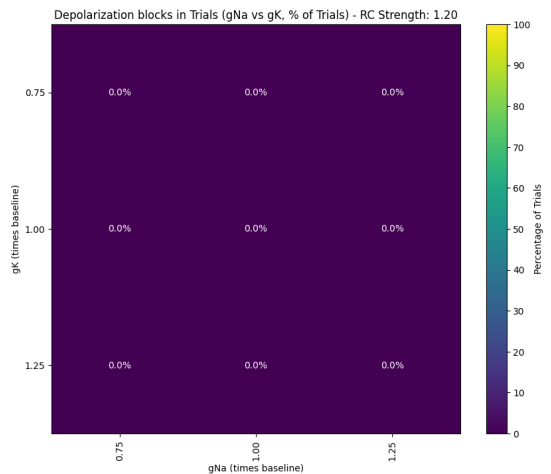


Figure C.3: Percentage of trials where depolarization block events occurred for all tested noise conditions. The x-axis shows all the sodium conductance changes in pyramidal cells, whereas the y-axis shows the potassium conductance changes in pyramidal cells. Modifications to pyramidal cells were applied to all compartments. The color intensity shows the average delay, where high-intensity yellow equals higher percentage of DPB events in a condition. The images are labeled from low noise to higher noise (a through e), respectively.



(e)

About Synaptica B.V.

Company Overview

Founded by Dr. Marijn Martens, Synaptica B.V. is a pioneering medical-scientific research and development company specializing in epilepsy. Synaptica employs biologically realistic spiking brain circuit models to perform advanced epilepsy calculations. Dr. Martens, a graduate cum laude from Donders Graduate School for Cognitive Neuroscience in 2010, has leveraged his extensive academic and startup experience to offer innovative diagnostic and therapeutic tools based on digital biomarkers.

Mission Statement

Synaptica continues to be at the forefront of neuroscientific research, pushing the boundaries of technology and science to better understand and treat neurological disorders. Synaptica as a company also strives to combine multidisciplinary research with computational modeling to develop personalized medicine approaches.

Recent Achievements

- **2024:** Through the EuroCC Open Call Application, Synaptica was awarded access to Snellius, the largest supercomputer in the Netherlands. This resource is enabling the company to perform crucial protein folding simulations of mutated ion channels, aiding in the prediction of functional consequences associated with channelopathies, such as epilepsy.
- **2023:** Synaptica secured a two-year R&D MIT AI research grant in collaboration with SME Artinis Medical Systems. This partnership focuses on developing a computer model that simulates neuron activity in humans and an fNIRS-based epilepsy headset for real-time brain activity monitoring. These tools aim to enhance the accuracy of epilepsy diagnosis and treatment.

List of Publications

- **2023** Human cortical spheroids with a high diversity of innately developing brain cell types, Kim de Klein, (...), M.B. Martens et al., *Stem Cell Research & Therapy*
- **2021** Two-Minute Walking Test With a Smartphone App for Persons With Multiple Sclerosis: Validation Study, Pim van Oirschot, (...), M.B. Martens et al., *JMIR Formative Research*
- **2020** Key role for lipids in cognitive symptoms of Schizophrenia, Dorien Maas, (...), M.B. Martens et al, *Translational Psychiatry*
- Numerous additional publications from 2020 to 2010, including significant contributions to the fields of cognitive neuroscience and digital health technology, emphasizing the genetic and molecular landscapes of various neurological conditions.

As implied by this study, identifying the origin of epileptic activity in the brain is a complex task that requires a comprehensive understanding of the underlying mechanisms. Computational modeling can only provide a theoretical framework for understanding the dynamics of the brain, and further experimental validation is necessary to confirm the findings. Such investigation can involve proteomics, genomics, and electrophysiological studies to elucidate the molecular and cellular mechanisms underlying epilepsy. Combining all of these subfields of neuroscience is essential to provide a comprehensive diagnostics tool for personalized medicine, a goal that Synaptica is committed to achieving.

Synaptica

Thank you for reading this report!
Return to the table of contents? [Click here!](#)